CHEMICAL REVIEWS

Review

pubs.acs.org/CR

Well-Ordered Transition Metal Oxide Layers in Model Catalysis – A Series of Case Studies

Helmut Kuhlenbeck, Shamil Shaikhutdinov, and Hans-Joachim Freund*

Fritz Haber Institute der Max Planck Gesellschaft, Faradayweg 4-6, 14195 Berlin, Germany

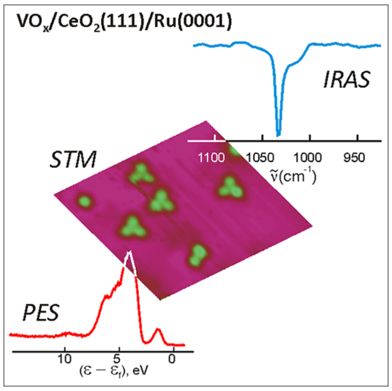

CONTENTS

1. INTRODUCTION

The development of surface science of solid metal surfaces during the last 50 years has been intimately connected with heterogeneous catalysis and culminated in the Nobel prize for Gerhard Ertl in 2007. While this is true, it is also a fact that in catalysis oxide surfaces play an important role as they are often used as supports or active materials themselves. However, this was not reflected in the worldwide efforts in the early decades of surface science. There are several arguments, which could be put forward to rationalize this observation. One group of reasons in this respect is connected with the experimental difficulties in the application of electron spectroscopies[2] to the study of poor electric and heat conductors. It has therefore been a goal to circumvent these problems by preparing thin, well-ordered oxide films on metal substrates, which do not charge upon electron impact or electron emission, and which may easily be cooled to liquid nitrogen or liquid helium temperatures.[3] Another group of reasons is connected with the structure of oxides. Defects play an even more important role for the reactivity of oxides as compared to metal surfaces.[4] The structural problems are intimately related to the stability and ill-defined stoichiometry of some oxide surfaces.

A practical advantage of thin film work over work with single-crystal surfaces is that in most cases sample preparation is simpler, and the research cost is often lower. However, there are issues that have to be considered in thin film work: The structure and epitaxial relations of the substrate may influence the stoichiometry of the thin films, and thus may be used to control the defect density of the oxide film. This in turn is important to understand chemical reactivity. Figure 1 illustrates the type of issues to be considered. The TPD spectra of NO desorbing from a cleaved single-crystal NiO(100) and a NiO(100) thin film grown on Ni(100) are very similar, but there are also differences that one should realize because they may be relevant: the larger width of the main desorption peak of NO desorbing from a thin film NiO(100) may or may not be related to the higher heating rate, but above 250 K there are desorption states that are related to a non-negligible density of nonregular adsorption sites. This is due to the mosaic structure of NiO(100) layers forming when the oxide grows on Ni(100)[5] but is not an intrinsic property of bulk NiO(100). The type of morphological differences depends on the type of the oxide, and there are also cases such as $V_2O_5(001)$ on Au(111)[6] where

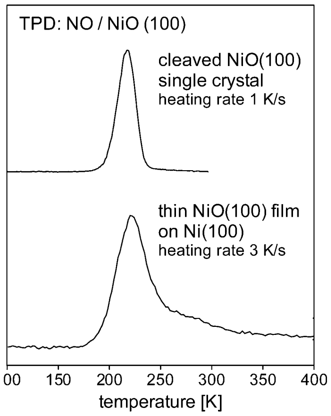

Figure 1. Thermal desorption spectra of NO on a cleaved single-crystal NiO(100) surface and on NiO(100)/Ni(100). Adapted with permission from ref 1. Copyright 1999 Wiley.

Special Issue: 2013 Surface Chemistry of Oxides

Received: August 2, 2012
Published: February 7, 2013

dx.doi.org/10.1021/cr300312n | *Chem. Rev.* 2013, 113, 3986–4034

the quality of the thin film surface is superior to that of the available single crystals. To understand chemistry on oxide surfaces, it is of paramount importance to have a clear picture of the molecule surface bond. We have chosen NiO(100) as a prototype system to discuss this aspect in more detail in the first part of this Review.

Films with varying thickness may be grown on a metal substrate and its properties studied as a function of the films thickness.[7] This is particularly important in connection with the growth of other active components such as metal or metal oxide nanoparticles on top of the oxide film to model dispersed metal or metal oxide catalysts on oxide supports.[8]

This Review covers structure/morphology−reactivity relations of a variety of thin film systems, including mainly binary oxides and the effect of defects, as well as oxide supported oxide nanoparticles. Because of the width of the field, this Review is restricted to oxide films with a structure that is similar to that of the respective bulk crystal; that is, thin films with special structures stabilized by the substrate−film interface energy are not covered.

2. NICKEL OXIDE: NiO(100)

First observations of nickel oxide formation on Ni(100) were reported already in the late 1950s/early 1960s.[9] NiO(100) has been systematically investigated since the 1980s and is therefore one of the first systematically investigated single-crystal transition metal oxide surfaces. NiO exhibits a rock salt structure with a lattice constant of 4.1684 Å.[10] The most stable and most often investigated surface is the (100) surface, but a number of investigations have also been performed for NiO(111).[11] A model of these surfaces and the unit cell are shown in Figure 2. The structure of the NiO(100) surface has been studied with IV-LEED.[12] It was shown that the surface structure is very similar to that of the bulk, with negligible rumpling and a contraction of the distance between surface layer and second layer of not more than a few percent.

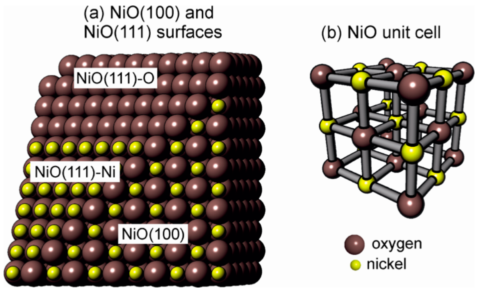

Figure 2. (a) Structure of NiO(100), oxygen-terminated NiO(111), and nickel-terminated NiO(111). (b) Unit cell of NiO.

NiO single crystals are readily available, and the (100) surface can be obtained by cleavage in situ.[12b] Many studies have been reported for thin NiO(100) layers produced by oxidation of Ni(100). In this case, LEED diffraction patterns with rather broad spots are observed due to a tilting of the oxide crystallites at the surface,[5,13] which is attributed to interface stress resulting from the difference of the NiO and Ni lattice constants. As was shown by Muñoz-Márquez, there is no sharp cutoff of the oxygen concentration at a certain depth below the surface: oxygen is found even in a depth of 100 Å below the surface after dosing 6000 L at elevated temperature.[13] Another common way to prepare a NiO(100) layer is evaporation of Ni onto Ag(100) in an oxygen atmosphere. In this case, the lattice fit between overlayer and substrate is much better because the lattice constant of silver (4.085 Å) is closer to the lattice constant of NiO than the lattice constant of nickel (3.524 Å). In recent publications, the complex structure of the silver−NiO interface has been discussed.[14] NiO(100) films have also been prepared by reactive deposition onto Pd(100).[15] The Pd(100) lattice parameter of 3.891 Å results in an overlayer−substrate lattice fit that is better than for Ni(100) but worse than for Ag(100).

There are a number of reasons why NiO(100) was studied. The interest from solid-state physics into NiO stems from the strong electron correlation in this oxide. There is a long-standing discussion about to what extent NiO is a Mott−Hubbard insulator or a charge-transfer insulator.[16] Also, technical aspects such as the use of NiO spin valves for hard disks,[17] and the use of NiO in catalysts for hydrogenation reactions,[18] and in electrodes for fuel cells[19] triggered a number of investigations.

The following discussion will, as alluded to in the Introduction, focus on two adsorbate systems, that is, NO/NiO(100) and CO/NiO(100), as prototype systems to understand the interaction of simple molecules with oxide surfaces. Together with CO/MgO(100) and NO/MgO(100), these systems served as benchmarks for the theoretical description of adsorbate−oxide bonding.[1,20]

A first detailed study of NO bonding to NiO(100) was performed in the 1990s with photoelectron spectroscopy, HREELS, and ab initio wave function-based cluster calculations.[7a] Figure 3 displays N1s and O1s XPS spectra of NO on different substrates as well as reference spectra for clean Ni(100). The N1s peak of NO on Ni(100) is slightly asymmetric, similar to data reported earlier by Shen et al.[21] HREELS[22] data reveal the presence of several adsorbed NO species in bent and upright geometry, which is probably the reason for the splitting of the O1s peak. A similar explanation may hold for the spectra of NO on oxygen precovered Ni(100)

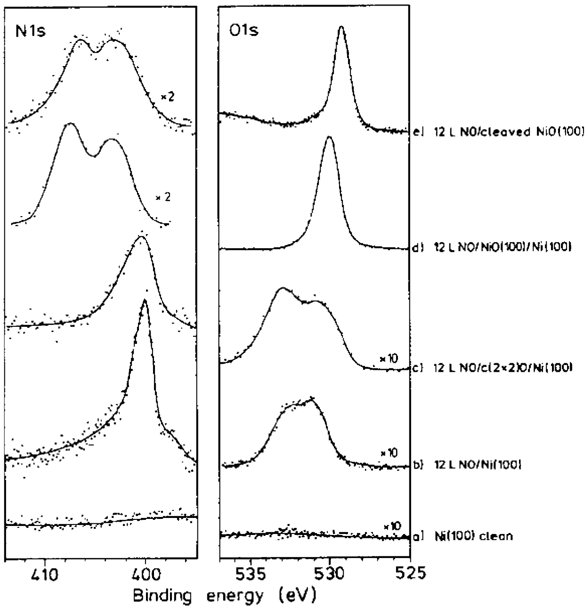

Figure 3. Set of N1s and O1s XP spectra for NO adsorbed on different substrates. Reprinted with permission from ref 7a. Copyright 1991 American Physical Society.

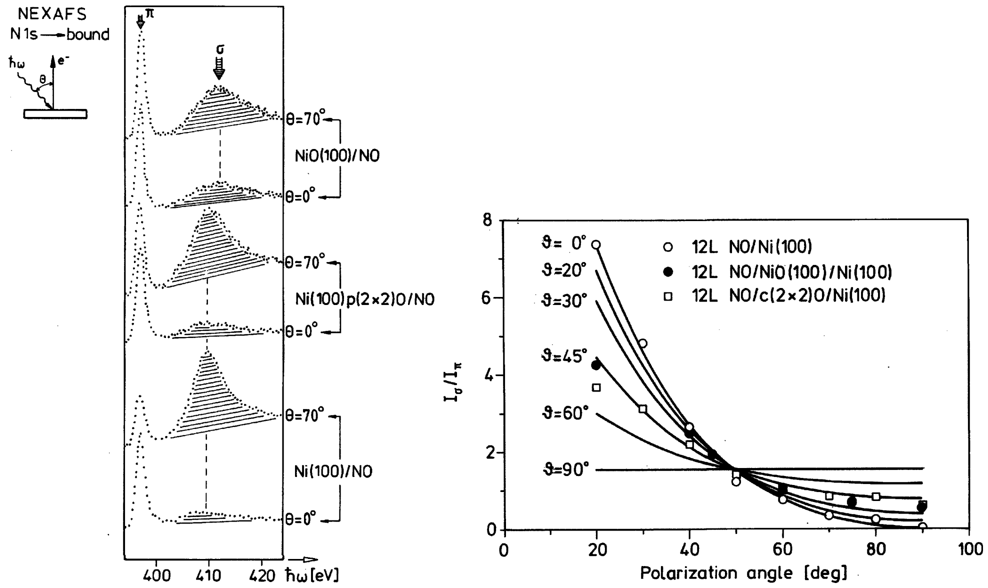

Figure 4. N1s NEXAFS results for NO adsorbed on NiO(100)/Ni(100) in comparison with results for NO adsorbed on Ni(100) and c(2 × 2)O/Ni(100). Left panel: N1s NEXAFS spectra for perpendicular and grazing light incidence. Right panel: Experimentally determined σ/π intensity ratios as a function of the light incidence angle together with calculated curves for different molecular orientations of the adsorbed NO molecules. Adapted with permission from ref 7a. Copyright 1991 American Physical Society.

[spectra (c)]. The intensity of the O1s signal of the c(2 × 2) oxygen overlayer was used to calibrate the NO coverage via the NO O1s intensity, assuming that the c(2 × 2) structure corresponds to an oxygen coverage of $\theta = 0.5$. From this, a NO coverage of $\theta \approx 0.2$ on NiO(100) was estimated.

The N1s spectrum of NO on NiO(100) [spectra (d)] exhibits two well-resolved peaks, while the O1s level cannot be separated from the substrate level. Because the N1s states of NO on NiO(100) and epitaxially grown NiO(100)/Ni(100) [spectra (e)] are rather similar and the coverages do not differ very much, it may be concluded that the adsorption on the epitaxial layer is not dominated by adsorption on defects.

Double peak structures like the ones in the N1s spectra of NO on NiO(100) are in many cases related to the presence of different bonding states on the surface. However, one would probably expect changes of the intensity ratio when the coverage changes, which was not observed with laser-induced desorption experiments.[23] Additionally, HREELS measurements revealed only a single NO stretching frequency,[7a] which means that the observed N1s doublet is not due to the presence of more than one adsorbate state, but to an intense satellite structure. Such intense satellites are not rare for weak chemisorption systems and have been observed for a number of adsorbates on metals such as CO/Cu, CO/Ag, CO/Au, N_2/Ni, and N_2/Ru.[24] Also, such satellite structure is well-known for molecular compounds with rather extended π electron systems and push–pull substituents, such as *para*-nitroaniline and related compounds with high electron polarizability.[25] It is the strength of coupling between adsorbate and substrate that determines the intensity of the two N1s peaks. The two levels are attributed to two different XPS final states, that is, a state where the core hole is screened by substrate electrons at lower binding energy, and another one with less screening at higher binding energies. For the case of a strong substrate–adsorbate coupling, the screened state is expected to be dominant, while the unscreened state is expected to be more intense for the case of a weak coupling.[24c,26] For the case of an intermediate coupling strength, that is, weak chemisorption, similar peak intensities may be expected.[24c,26]

Figure 4 (left) compares N–K edge NEXAFS spectra of a saturated NO layer on epitaxial NiO(100) recorded at normal and grazing light incidence. The narrow peaks below 400 eV are due to the N1s→2π resonance, while the broad features centered at ~410 eV are due to the σ shape resonance. The former is excited with light polarized perpendicular to the molecular axis, while the latter is excited with light polarized along the molecular axis, which means that the molecular orientation can be revealed by experiments where the resonance intensities are measured as a function of the light polarization. According to Somers et al.,[27] the ratio of the resonance intensities can be described by eq 1 for NO-type molecules with a random azimuthal orientation of the molecular axes:

$$\frac{I_\sigma}{I_\pi} = K \frac{P(\sin^2\delta\sin^2\theta + 2\cos^2\delta\cos^2\theta) + (1-P)\sin^2\delta}{1 - P\cos^2\theta} \tag{1}$$

K is a proportionality constant, δ is the tilt angle with respect to the surface normal, θ is the angle of incidence, and P is the degree of polarization of the incident light. Figure 4 (right) shows the experimental results for NO on clean Ni(100) (○), on oxygen precovered Ni(100) (□), and on epitaxial NiO(100) (●) together with curves calculated for different tilting angles δ according to eq 1. The best agreement between the experimental data for NO on NiO(100) and the calculated curves is obtained for a tilting angle of $\delta \approx 45°$. The accuracy of this result is somewhat limited since the optical constants of the substrate could not be taken into account because they are not known. Nevertheless, the result clearly indicates that the NO molecules are not bound in an upright geometry on NiO(100).

Ab initio cluster calculations for a NiO_5 cluster with one NO molecule bound with its nitrogen end to the Ni atom were employed to explain this result. The lower left part of Figure 5 shows the relevant part of the MO scheme for a perpendicularly oriented NO molecule, while the lower right part shows the corresponding scheme for tilted NO molecules in C_S symmetry. The table at the top of the figure contains the symmetry representations of some relevant orbitals for three different symmetry groups (C_1, C_S, and C_{4V}). The major difference between the tilted and the linear geometries is that the π_x and π_y levels are degenerate in linear geometry, while this degeneracy is lifted in the tilted geometry. The same applies to the d_{xz} and d_{yz} levels.

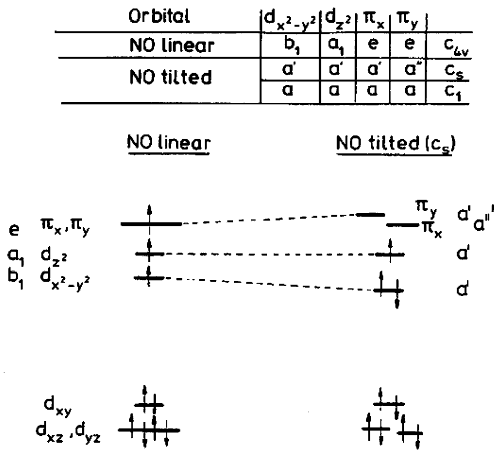

Figure 5. One-electron scheme of the Ni3d and NO 2π levels for NO adsorbed on NiO(100) in a linear and a bent configuration. Reprinted with permission from ref 7a. Copyright 1991 American Physical Society.

For the linear configuration, the ground state is a quartet state. The bonding interaction between the NO 2π level and the energetically nearby d states is negligible because they transform according to different irreducible representations. On the other hand, in the tilted configuration with C_S symmetry, the $2\pi_x$ level transforms according to the same symmetry representation as the nearby d levels, and consequently these levels will mix such that bonding and antibonding hybrid states are formed. The level at lowest energy will be energetically stabilized with respect to the noninteracting system, and the system may gain energy by doubly occupying this level. Therefore, a bent configuration is energetically more stable in a simple one-electron picture. Similar arguments apply to a tilted system with C_1 symmetry where all levels transform according to the same irreducible representation.

SCF calculations corrected for the BSSE and augmented by a CI calculation, including Ni3d and NO 2π orbitals for a NO–NiO_5 cluster with linearly coordinated NO, yielded a small positive energy, that is, no bonding, while BSSE-corrected SCF calculations using TZP-quality basis functions gave a weak binding energy of 0.04 eV for the ground state. Similar to results obtained by Janssen and Nieuwpoort[28] for a NiO_6^{10-} cluster, the $3d^8 4s^0$ configuration represents more than 98% of the state in the first calculation.

The methodology of the first calculation was also applied to a NO–NiO_5 cluster with the NO molecule tilted along the Ni–O direction. In this case, charge-transfer configurations of the Ni3d and NO 2π orbitals had to be considered additionally due to the reduced symmetry. A potential minimum of −0.17 eV relative to the ground-state energy of the first calculation was found for a NO tilting angle of about 45°. The following charge-transfer configurations are the major contributions to this state:

$$[(\text{“}t_{2g}\text{”})^6 (d_{z^2})^1 (d_{x^2-y^2})^2 (\pi_x)^0]$$

$$[(\text{“}t_{2g}\text{”})^6 (d_{z^2})^2 (d_{x^2-y^2})^1 (\pi_x)^0]$$

$$[(\text{“}t_{2g}\text{”})^6 (d_{z^2})^0 (d_{x^2-y^2})^1 (\pi_x)^2]$$

$$[(\text{“}t_{2g}\text{”})^6 (d_{z^2})^1 (d_{x^2-y^2})^0 (\pi_x)^2]$$

The CI coefficients are between 0.45 and 0.53, which shows that this state is heavily mixed; even states with doubly occupied 2π orbitals are relevant. Figure 6 shows the binding of some states of the NO–NiO_5 cluster as a function of the NO tilting angle, calculated for a Ni–N distance of 2.1 Å.

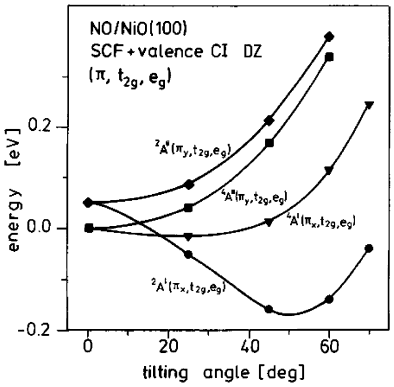

Figure 6. Calculated energies of a NO–NiO_5 cluster for some electronic states as a function of the tilting angle of the NO molecule. Energies are referenced to the ground state of NO adsorbed in a linear configuration. Adapted with permission from ref 7a. Copyright 1991 American Physical Society.

In later studies, the geometry of NO/NiO(100) was determined with photoelectron diffraction.[29] The tilt of the N–O bond relative to the surface normal was determined to be 59° (+31°/−17°), the distance of the N atom and the Ni atom below was determined to be 1.88 ± 0.02 Å, and the N1s-splitting in XPS spectra was experimentally verified.

A careful TPD study was performed for NO and CO on NiO(100). This study was triggered by the need for reliable adsorption energy values because at that time the theoretical values exhibited a significant spread, which was also the case for the experimental numbers (see Table 1).

Figures 7 and 8 display sets of TPD spectra for NO and CO on NiO(100) cleaved in vacuo and NiO(100) grown as a thin film on Ni(100). In the case of the thin film preparations, only cooling with liquid nitrogen was possible so that temperatures below $T \approx 85$ K could not be reached. Thus, multilayer desorption does not show up in these data.

Obviously, the desorption spectra for the thin film NiO(100) substrates and the single-crystal samples are very similar, again demonstrating that the interaction of NO and CO with NiO(100) films is not dominated by defect adsorption.

The TPD data have been quantitatively evaluated via the leading edge method and complete analysis. Details of these methods may be found in ref 40. Both methods determine the heat of adsorption of desorbing molecules as a function of the coverage of molecules on the surface. Results are displayed in

Table 1. Table of Literature Data for Adsorption of CO and NO on NiO(100) and Mg(100)[a]

author	system	method	adsorption energy [eV]
Pacchioni and Bagus[31]	CO/NiO(100)	ab initio cluster calculation	0.24
Pöhlchen and Staemmler[32]	CO/NiO(100)	ab initio cluster calculation, BSSE correction	0.03–0.1
Cappus et al.[33]	CO/NiO(100)/ Ni(100)	TPD, Redhead	0.32
Vesecky et al.[34]	CO/NiO(100)/ Ni(100)	IRS, Clausius–Clapeyron	0.45
Staemmler[35]	NO/NiO(100)	ab initio cluster calculation, BSSE correction	0.1
Kuhlenbeck et al.[7a]	NO/NiO(100)/ Ni(100) and NO/ NiO(100)	TPD, Redhead	0.52
Nygren and Pettersson[20f]	CO/MgO(100)	ab initio cluster calculation, BSSE correction	0.08
Chen et al.[36]	CO/MgO(100)	DFT	0.28
Neyman et al.[37]	CO/MgO(100)	DFT, BSSE correction	0.11
He et al.[38]	CO/MgO(100)/ Mo(100)	IRS, Clausius–Clapeyron	0.43
		TPD, Redhead	0.46
Furuyama et al.[39]	CO/MgO powder	IRS, Clausius–Clapeyron	0.15–0.17

[a] Clausius–Clapeyron: Evaluation of pressure and temperature-dependent IR intensities with the Clausius–Clapeyron equation. Redhead: Evaluation of TPD data with the Redhead equation.[30] Adapted with permission from ref 1. Copyright 1999 Wiley.

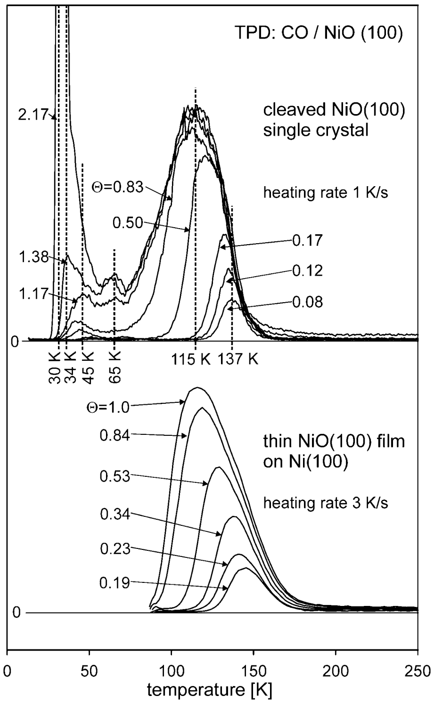

Figure 7. Thermal desorption spectra of CO on NiO(100) cleaved in vacuo (top) and CO on a thin NiO(100) film grown by oxidation of Ni(100) (bottom). The mass spectrometer was set to mass 28 (CO). The coverages θ are given relative to the coverage of a full monolayer. Reprinted with permission from ref 1. Copyright 1999 Wiley.

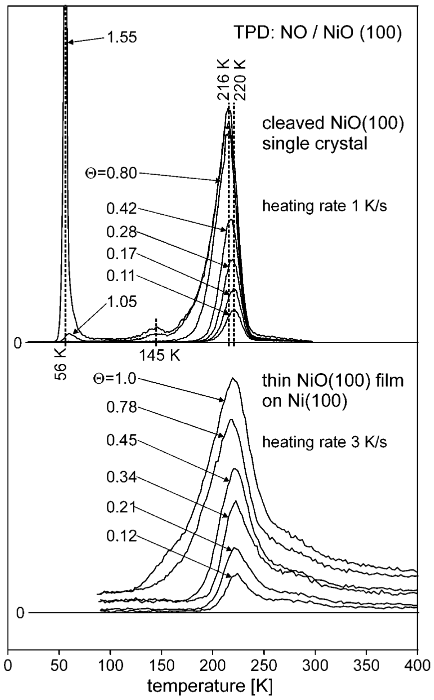

Figure 8. Thermal desorption spectra of NO on NiO(100) cleaved in vacuo (top) and NO on a thin NiO(100) film grown by oxidation of Ni(100) (bottom). The mass spectrometer was set to mass 30 (NO). The coverages θ are given relative to the coverage of a full monolayer. Reprinted with permission from ref 1. Copyright 1999 Wiley.

Figures 9 and 10 for CO and NO, respectively. For both types of adsorbates, the adsorption energies decrease with increasing coverage due to lateral interactions until they reach values near those of the respective multilayers (0.0885 and 0.177 eV for CO and NO, respectively[41]) at coverages of about 1. The low coverage values have been determined by averaging over the

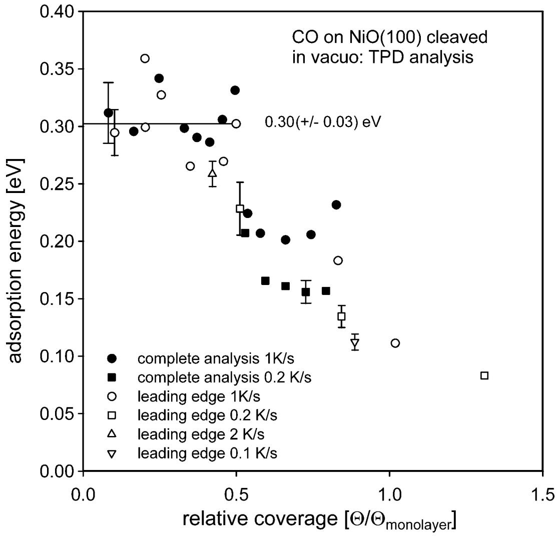

Figure 9. Adsorption enthalpy of CO on NiO(100) cleaved in vacuo as a function of coverage. The data have been determined from TPD spectra. (Top) Using the leading edge method[40a] and complete analysis.[40b] TPD data taken with heating rates of 0.1, 0.2, 1, and 2 K/s have been used. The indicated errors have been obtained from the numerical uncertainty of the fits employed in the evaluation procedure. Reprinted with permission from ref 20g. Copyright 1999 Elsevier.

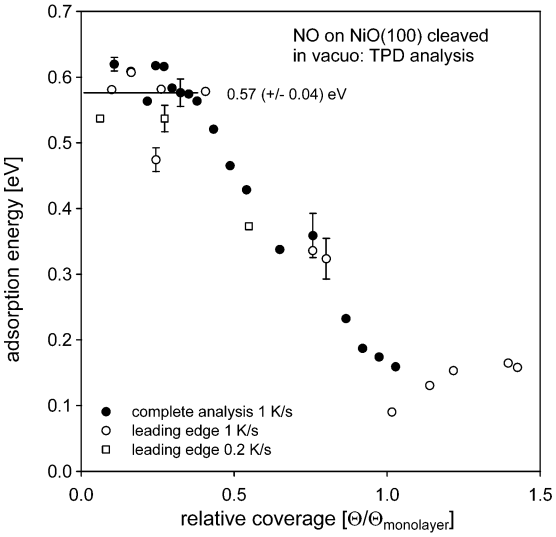

Figure 10. Adsorption enthalpy of NO on NiO(100) cleaved in vacuo as a function of coverage. The data have been determined from TPD spectra. (Top) Using the leading edge method[40a] and complete analysis.[40b] TPD data taken with heating rates of 0.2 and 1 K/s have been used. The indicated errors have been obtained from the numerical uncertainty of the fits employed in the evaluation procedure. Reprinted with permission from ref 20g. Copyright 1999 Elsevier.

coverage regions indicated in Figures 9 and 10, yielding values of 0.30 ± 0.03 and 0.57 ± 0.04 eV for CO and NO, respectively. These values are suitable for comparison with theoretical results because in the low coverage regime lateral interactions, which have been neglected in the theoretical studies, are weak.

The experimental results discussed above for NO and CO on NiO(100), together with results for CO on MgO(100),[1,20g] triggered a number of theoretical studies.[20a−c,42] Most of these studies aimed at improving the theoretical description of the adsorbate−oxide bond. This was and is a complex and ongoing development.

3. NICKEL OXIDE: NiO(111)

If a NiO single crystal were cut perpendicular to the [111] direction, then an oxygen-terminated or a nickel-terminated (111) surface would result. These surfaces are both shown in Figure 2a. A (111)-terminated NiO crystal consists of layers containing only Ni^{2+} or O^{2-} ions. These layers are stacked consecutively along the [111] direction. If the bottom and the top of such a crystal are terminated by ideal (111) planes, charge neutrality requires that one side is oxygen terminated and the other one is metal terminated. Such an arrangement is called polar. It is energetically unstable because the electrostatic energy per atom increases linearly with the thickness of the sample.[43] Tasker has categorized crystalline surfaces into three polarity types (see Figure 11): type 1 contains electrically neutral layers with equal density of positive and negative charges (Figure 11A). NiO(100) is a representative of this class of nonpolar and energetically stable surfaces. Type 2 is built up of electrically charged layers but has a repeat unit without dipole moment perpendicular to them. Ideal corundum (0001) surfaces are an example of this arrangement. Such surfaces may be polar or nonpolar, depending on the terminating layer; examples are shown in Figure 11D−F. Finally, type 3 also has charged planes, but it is not possible to find a repeat unit

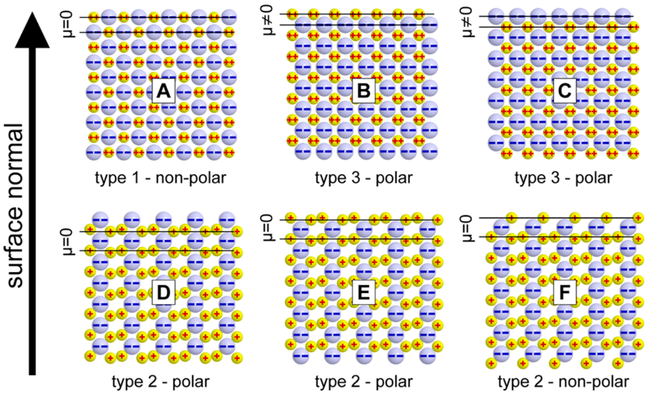

Figure 11. Schematic examples of the three surface polarity types defined by Tasker.[43]

without dipole moment perpendicular to them (see Figure 11B,C). Such surfaces will always be polar, and NiO(111) belongs to this class.

Polar surfaces like the one shown in Figure 11B−E are not expected to exist for real crystals, because they are energetically very unfavorable. However, there are ways to stabilize them. Because the energetic instability is the consequence of a noncompensated dipole field between the top and the bottom surface, a reduction of the charge density in the top and the bottom layer by 50% stabilizes such an atomic arrangement.[43] The charge density reduction is not necessarily confined to the top and bottom layers; it may also be distributed over a number of layers in the surface region.

Ways to reduce the charge are illustrated in Figure 12:

- Reduction of the charge of each of the atoms in the top and in the bottom layer by 50% as shown in Figure 12A. It is clear that this may have a significant impact on the electronic structure in the surface region; special electronic surface states, metallization, etc., may result.
- Reconstruction of the surface. In Figure 12B, the simple case of omission of every second atom in the top and bottom layers is illustrated, but also more complex reconstruction schemes are conceivable. In 1992, Wolf introduced a scheme for the rock salt structure where the Madelung summation is performed with complete cubic unit cell contents as base "molecules". These units consist of an electrically neutral arrangement of 8 atoms without a dipole moment. Use of such base units leads to the so-called octopolar surface reconstruction, which comes in an oxygen-terminated and a metal-terminated flavor as shown in Figure 13. In this case, the charge density reduction is distributed over two layers: in the top layer 75% of the atoms are missing, and in the second layer 25% are missing. This structure comprises pyramids consisting of 3 atoms of one sort and 1 atom of the other arranged in a p(2 × 2) repeat unit on the polar surface.

  The p(2 × 2) reconstruction may be viewed as a small-size limit for surface faceting, where the nonpolar surfaces of the facets actually define the crystal surface. This type of surface stabilization has been observed for MgO(111) (see Gajdardziska-Josifovska et al[44] and references therein).
- Adsorption of charged adsorbates as sketched in Figure 12C for the case of a hydroxyl-type adsorbate.

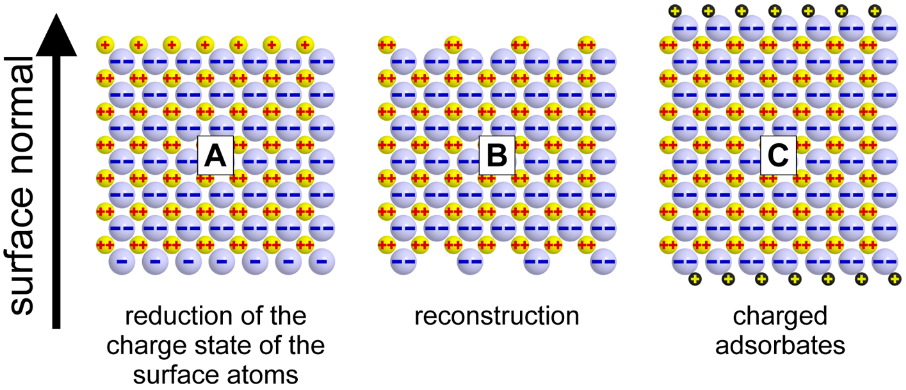

Figure 12. Stabilization of polar surfaces by reduction of the charge of the surface atoms (A), reconstruction (B), and charged adsorbates (C).

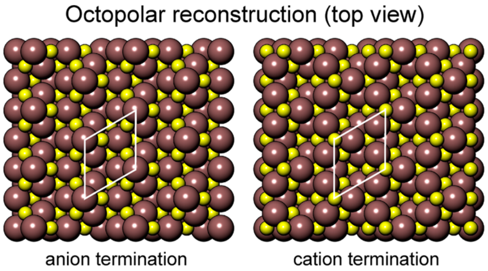

Figure 13. Top views of the oxygen- and metal-terminated octopolar reconstructions of rock salt (111) surfaces as introduced by Wolf.[47] The (2 × 2) unit cell of the reconstruction is indicated.

Reviews of the theoretical aspects of surface polarity have been published by Noguera[45] and Goniakowski et al.[46]

For an existing polar surface, one of these mechanisms must be operative. Of course, the stabilization mechanism may change as a function temperature, pressure, and composition of the ambient atmosphere, where especially the stabilization by adsorbates is an interesting topic from the chemical point of view. The complex of related questions triggered many of the studies dealing with NiO(111).

LEED images of NiO(111) on Ni(111) were published already in 1963 by MacRae.[48] Since then, NiO(111) single-crystal surfaces have been studied,[11a,49] as well as thin layers on Ni(100),[49a,50] Ni(111),[11c,d,48,51] Au(111),[11e,52] Mo(110),[53] and α-Al_2O_3(0001).[54] Unlike NiO(100), NiO(111) single-crystal surfaces cannot be prepared by cleavage but must be prepared by cutting, polishing, and thermal treatment in oxygen.[49e] According to Langell and Nassir,[50c] NiO(111) on Ni(100) is stabilized by hydroxyl groups and transforms into NiO(100) when the hydroxyls desorb at 600 K. Reachable thicknesses are in the range of a few layers. Figure 14 shows that the quality of such oxide layers may be reasonable. The appearance of a 12-spot ring instead of the expected ring with 6 LEED spots is due to the presence of different oxide domains. LEED intensity analysis led Warren and Thiel[50b] to the conclusion that the layer is terminated by oxygen, which might be compatible with hydroxyl termination because the scattering cross section of hydrogen is weak.

A LEED pattern of NiO(111) on Ni(111) is shown in Figure 15. The background and the limited sharpness of the spots indicate the presence of a notable density of defects. If the sample is annealed at 600 K, then intensity at p(2 × 2) positions shows up in the LEED pattern, which triggered a SPA-LEED investigation. Figure 16[52b] shows SPA-LEED images, and Figure 17[52b] displays line scans that visualize the evolution of intensity at p(2 × 2) positions. HREELS[52b] shows that the NiO(111) layer is covered by hydroxyl groups before the flash and that the flash removes them (hydroxyl groups were also observed by a number of other groups with HREELS[50c,51b,h] and XPS[11a,50c,51b,h,l,55]). Removal of these groups requires that a different stabilization mechanism becomes active, which was assumed to be the octopolar reconstruction introduced by Wolf.[47] This reconstruction leads

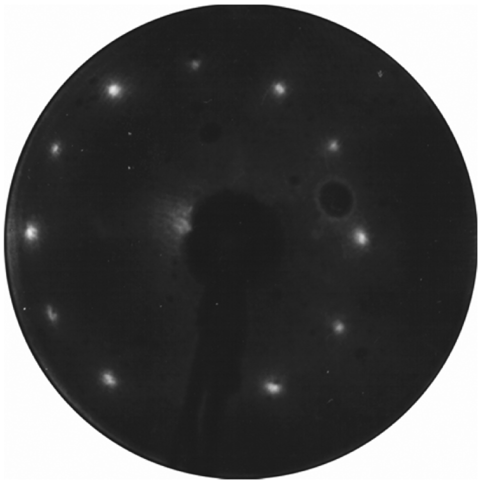

Figure 14. LEED pattern of NiO(111) on Ni(100).

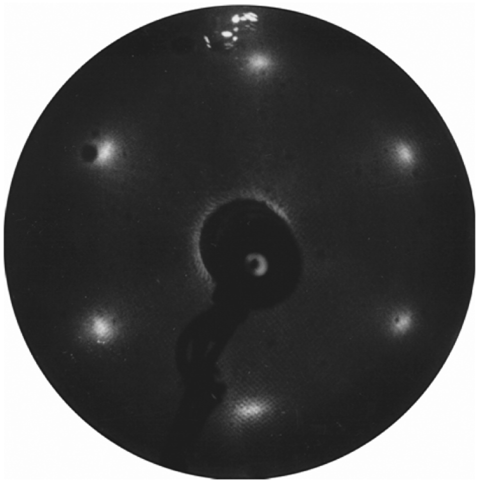

Figure 15. LEED pattern of NiO(111) on Ni(111). Adapted with permission from ref 52b. Copyright 1994 Elsevier.

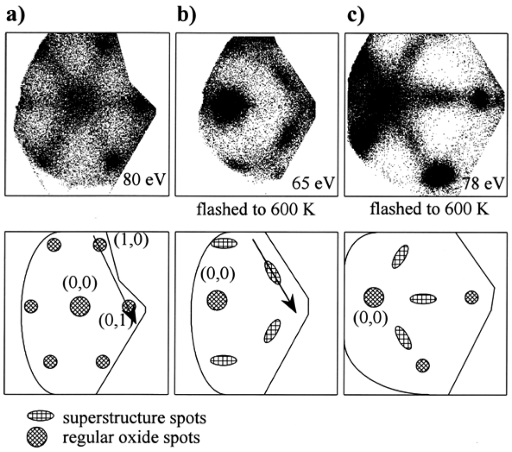

Figure 16. SPA-LEED patterns of (a) the p(1 × 1), and (b,c) the p(2 × 2) reconstructed surfaces at two different electron energies. The arrows refer to Figure 17. Reprinted with permission from ref 52b. Copyright 1994 Elsevier.

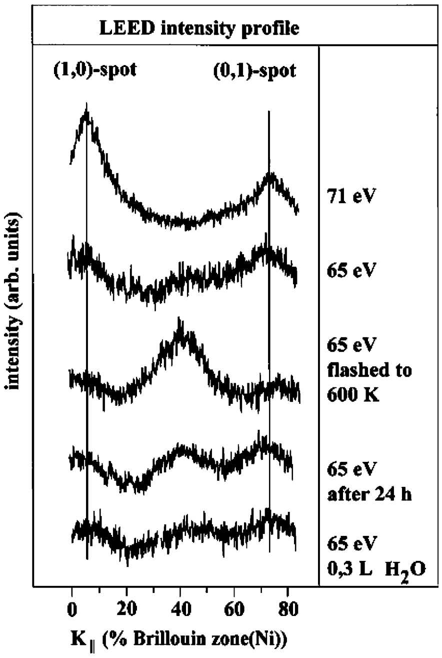

Figure 17. SPA-LEED scans along a direction as indicated in Figure 16 for the p(1 × 1) surface (two topmost traces) and the reconstructed surface at 65 eV electron energy. The two lowest traces indicate the changes occurring when the sample is exposed to the background pressure for 24 h or to a dose of 0.3 L of H_2O directly after reconstruction has taken place. Reprinted with permission from ref 52b. Copyright 1994 Elsevier.

to a p(2 × 2) LEED superstructure (see Figure 13). A p(2 × 2) structure was also observed with STM for thin layers of NiO(111) on Au(111).[52c]

Kitakatsu et al.[51l] studied a three to four layers thick NiO(111) layer on Ni(111) and found that a hydroxyl coverage of 0.85 ± 0.1 monolayers stabilized the unreconstructed surface. Dosing of 150 L of water increased the coverage to 1.5−2.0 monolayers, which was assigned to the formation of a OH−Ni−OH surface triple layer as found in β-Ni$(OH)_2$.

A number of structural studies were performed for NiO(111) single-crystal surfaces using GIXS by Barbier, Renaud, and coworkers. The single-crystal surfaces were prepared by first annealing a NiO(111) boule in air at 1850 K for 24 h in air, followed by cutting, polishing, and reannealing in air at 1300 K for 3 h.[52d] Barbier and Renaud[49b] found that stoichiometric (oxidized) NiO(111) is stabilized by a p(2 × 2) reconstruction, while heating at 860 K in vacuum produces metallic Ni at the surface. It was reported that annealing in air leads to an unreconstructed surface, which was attributed to stabilization by adsorbates. For the latter case, a forthcoming paper[49c] confirmed that the surface is not reconstructed. It was suggested that adsorbate molecules stabilize it, but details could not be given.

In a later publication, Barbier et al.[49d] revoked the statement that NiO(111) surfaces annealed in air are nonreconstructed and reported that such surfaces exhibit a p(2 × 2) reconstruction. The detection of this reconstruction was attributed to a better crystalline quality of the sample used in this study. Annealing a p(2 × 2)-terminated sample in vacuum produced a surface that was partly terminated by the regular octopolar reconstruction and partly by a p(2 × 2) structure where some atoms are displaced with respect to the regular octopolar reconstruction. With increasing temperature, the proportion of the modified p(2 × 2) structure was shown to increase. It was not possible to differentiate between metal- and oxygen-terminated reconstructions, and it was noted that besides coexistence of both structures also a single surface termination with variable displacements of the second layer atoms might be conceivable.

A later publication by Barbier et al.[49e] addressed the p(2 × 2) structure issue again. The authors report that the octopolar reconstruction of an air-annealed NiO(111) single-crystal surface is terminated by nickel. Annealing in 10^{-4} mbar of O_2 at 700 K reduces the surface and induces the formation of a p(2 × 2) oxygen-terminated superstructure related to the (111) surface of a spinel-type (Me_3O_4) oxide. It was reported that dosing of 10^6 L of H_2O with a pressure of 10^{-6} mbar did not change the surface structure (i.e., did not produce a hydroxylated unreconstructed surface), which was attributed to the low defect density of the prepared surfaces.

Barbier et al.[52d] also studied the structure of a thin NiO(111) film on Au(111), finding that the film on Au(111) is terminated by a mixture of oxygen- and nickel-terminated octopolarly reconstructed areas. This was somewhat at variance with the STM results of Ventrice et al.[52c] who observed that domains on the surface are separated by double steps, which would mean that the investigated surface was terminated by only one type of octopolar reconstruction. Similar to what was found for NiO(111) single-crystal surfaces,[49e] thin films on Au(111) also turned out to be insensitive to exposure to 10^6 L of H_2O (this time dosed with a H_2O pressure of 3×10^{-5} mbar).

Erdman et al.[56] reinterpreted the X-ray diffraction data of Barbier et al.[52d] for NiO(111) on Au(111) using direct methods[57] and reported that they could not reproduce the results of Barbier et al. Instead, they proposed a defect structure where 25% of the atoms of the Ni layer below the surface oxygen layer are transferred to above the oxygen layer, thus giving rise to a p(2 × 2) superstructure with subsurface vacancies. However, it was noted that this configuration is not charge-neutral: in a simple ionic picture, it exhibits an excess charge of 4 electrons per (2 × 2) surface unit cell. Calculations reported in the same manuscript suggest that charge neutrality may be provided by a reduction of the charge of some surface oxygen atoms.

In a later publication, Ciston et al.[11a] published results obtained with off-zone-axis THEED, XPS, and DFT. The NiO(111) single-crystal sample was mechanically dimpled and thinned by ion beam milling until it was sufficiently transparent for the electron beam. After this procedure, the sample was annealed under flowing O_2 to recover the surface. This procedure produced surfaces with a distribution of misorientations by different angles in different azimuthal directions along the surface. The THEED data were again evaluated with direct methods. Annealing the sample to 1150 °C in a tube furnace under flowing O_2 led to the appearance of a p(2 × 2) superstructure. This structure (called 2 × 2-α-OH) was identified as a structure already found before for MgO(111).[58] It is a hydroxylated structure, which is different from the octopolar reconstruction and from the structure with subsurface vacancies identified by Erdman et al.[56] It was indicated that the spinel-type surface structure observed by Barbier[49e] was actually a 2 × 2-α-O phase.[11a]

Annealing to only 950 °C was shown to lead to a $(\sqrt{3} \times \sqrt{3})$R30° reconstruction, which was assigned to a hydroxylated structure also already reported for MgO(111).[58] The existence of hydroxyls was verified with O1s XPS. Such a superstructure was also observed by Floquet and Dufour[60] who related its occurrence to the presence of silicon. Gajdardziska-Josifovska et al.[44] also studied NiO(111) with THEED using direct methods. They observed the $(\sqrt{3} \times \sqrt{3})$R30° superstructure after annealing in air at 1000 °C with the lower limit for the formation of this structure being 650 °C. A model based on cyclic ozone units was proposed, which is different from the model put forward by Ciston et al.[11a]

Ebensperger and Meyer,[59] Zhang and Tang,[61] and Ciston et al.[11a] published DFT-based calculations of the surface free energy as a function of the oxygen and/or water chemical potential. These publications essentially agree in that within a water-free environment the oxygen-terminated octopolar reconstruction should be the most stable one for a wide range of oxygen chemical potentials. The Ni-terminated octopolar reconstruction is only slightly higher in energy (35 meV per (1 × 1) unit cell area according to Ebensperger and Meyer[59]). Regarding the influence of the water chemical potential on the equilibrium surface structure, Ebensperger and Meyer[59] found that for a chemical potential of water of less than −1.7 eV the surface should be terminated by the oxygen-terminated octopolar reconstruction, while at higher chemical potentials a completely hydroxylated unreconstructed surface should be the equilibrium structure. The results of Ciston et al.[11a] are not much different, but they position the crossover between the two structures at −1.88 or −2.08 eV depending on the functional used in the DFT computations. A phase diagram as published by Ebensperger and Meyer[59] is shown in Figure 18. It clearly shows that, according to the DFT results, surfaces other than the fully hydroxylated unreconstructed surface and the oxygen-terminated octopolarly reconstructed surface should only be found under conditions, which are not easily reachable under equilibrium conditions. Therefore, the observations of such structures may be related to nonequilibrium conditions or preparation issues.

The need for stabilization forces the polar NiO(111) surface to either react with adsorbates or reconstruct. Both effects enhance the chemical activity. The octopolar reconstruction increases the number of different types of surface sites, which may be relevant for surface reactions. Knudsen et al.[62] and Peng et al.[51u] have studied CO oxidation on Ni(111). It was found that CO_2 desorption after O_2 adsorption followed by CO adsorption already occurs at 120 K. O_2 needs to be adsorbed prior to CO; if CO is adsorbed prior to O_2, then no CO_2 is produced.[62] Molecularly adsorbed oxygen could be detected with TPD and XPS,[62] which led to the speculation that CO_2 production might be related to the presence of this species. Figure 19 shows that NiO is already formed after a dosage of 20 L of O_2 at 100 K, and therefore the question arose whether CO oxidation proceeds on NiO(111) or on Ni(111) with chemisorbed oxygen.

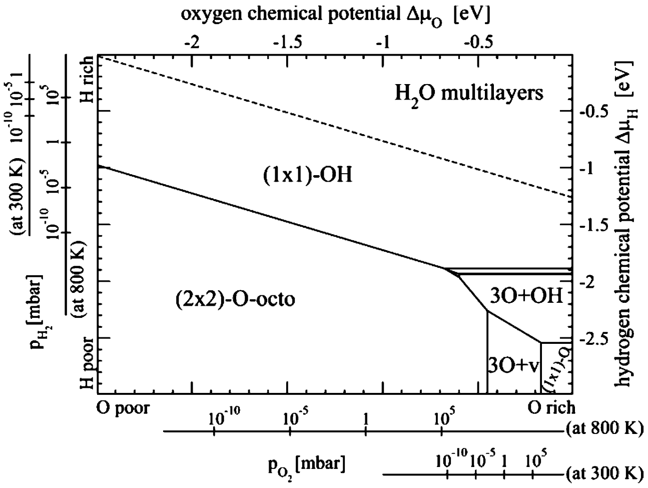

Figure 18. Phase diagram of the NiO(111) surface in thermodynamic equilibrium with H_2 and O_2 reservoirs controlling the chemical potentials $\Delta\mu_O$ and $\Delta\mu_H$. The upper right area indicates conditions under which water multilayers would form. $\Delta\mu_O(T, p)$ and $\Delta\mu_H(T, p)$ have been translated to pressure scales for fixed temperatures of T = 300 and 800 K. (1 × 1)-OH and (2 × 2)-O-octo are the fully hydroxylated nonreconstructed surface and the oxygen-terminated octopolarly reconstructed surface. For details, see Ebensperger and Meyer.[59] Reprinted with permission from ref 59. Copyright 2011 Wiley.

Peng et al.[51u] applied density functional theory to solve this problem. The activation barriers for CO oxidation on Ni(111) with chemisorbed oxygen were found to be at least 0.5 eV,[51u] which is too high for CO_2 formation at 120 K. A viable reaction path was found for octopolarly reconstructed NiO(111). CO was proposed to adsorb on nickel sites of oxygen-terminated octopolarly reconstructed NiO(111) as sketched in Figure 20a. Figure 20b visualizes the geometry of O_2, which adsorbs molecularly, bridging toward three nickel sites.

The proposed reaction schema is schematically illustrated in Figure 21. It is assumed that the surface is oxygen covered as indicated in Figure 20a. An incoming CO molecule reacts with the apical oxygen atom of an octopolar pyramid, and the reaction product CO_2 desorbs (Figure 21b). CO_2 desorption is facilitated if an O_2 molecule adsorbs on the apex site while the CO_2 molecule desorbs (Figure 21c), enabling CO_2 to desorb at low temperature. Another CO molecule can easily react with the oxygen atom surrounded by a circle in Figure 21d. The reaction product CO_2 desorbs, and the surface reaches the state it had before the reaction started. For completeness, it is mentioned that also the effect of deposited gold was investigated,[62] and it was found that gold suppresses surface carbonate formation (which occurs without the presence of gold) and increases the CO_2 yield. Details on the mechanism were not given.

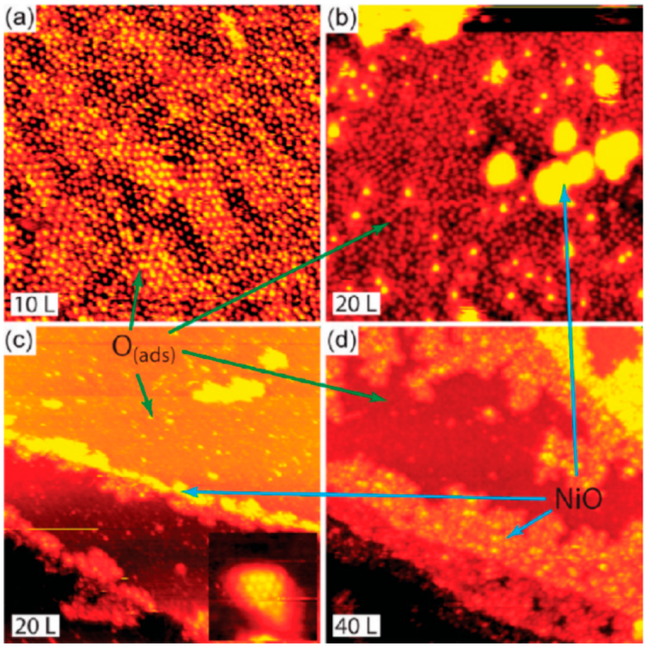

Figure 19. (a−d) STM images of Ni(111) following exposure to the indicated quantities of O_2 at 100 K. The inset in (c) shows a NiO(111) island formed upon oxidation at room temperature. (a) 200 × 200 Å^2, (b) 200 × 200 Å^2, (c) 1000 × 1000 Å^2, inset 25 × 25 Å^2, (d) 1000 × 1000 Å^2. Reprinted with permission from ref 51u. Copyright 2010 American Chemical Society.

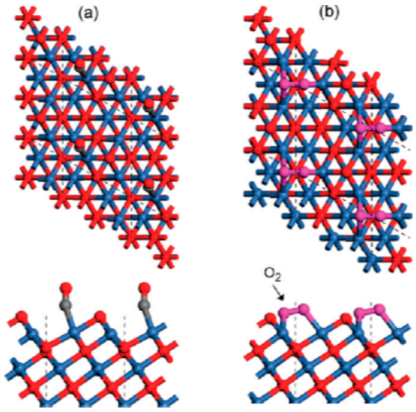

Figure 20. Top and side views for (a) CO and (b) O_2 adsorbed on octopolarly reconstructed NiO(111). The parallelogram drawn with dashed lines indicates the (2 × 2) supercell. Blue, gray, and red (pink) spheres represent Ni, C, and O atoms, respectively. Reprinted with permission from ref 51u. Copyright 2010 American Chemical Society.

The increased reactivity had also been addressed earlier.[61,63] Papp and co-workers had shown that through topotactical decomposition of $Ni(OH)_2$, NiO powder may be produced whose crystallites show predominantly (111) orientation. Its activity with respect to $DeNO_x$, that is, the formation of nitrogen and water from NO and ammonia, was investigated. Only after heating above 400 K, when the lost thrust of water loss has taken place, and the stabilizing OH groups bound to the NiO(111) crystallites begin to separate off as water does the powder become active. Those observations are very much in line with the expectations discussed in this section: while the OH-terminated surface is stable and does not exhibit a pronounced reactivity, the water-free but reconstructed surface has sufficient energy to drive the $DeNO_x$ reaction. Because the reaction produces water, the reactivity could decrease again and be reactivated by thermal treatment to stimulate water loss.

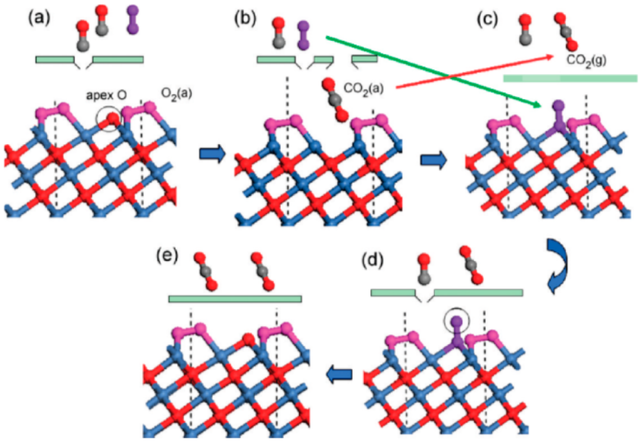

Figure 21. (a−e) Schematic of the CO oxidation catalytic cycle O_2 + 2CO → $2CO_2$ on NiO(111). Blue and gray spheres represent Ni and C atoms, respectively. Purple and pink spheres are used for gas-phase and adsorbed O species, respectively, while lattice O in NiO is red. Reprinted with permission from ref 51u. Copyright 2010 American Chemical Society.

4. CHROMIUM OXIDE: Cr_2O_3(0001)

Chromium oxide has various applications including corrosion inhibition[64] and catalysis. It is a relevant component of the Phillips catalyst for ethylene polymerization, and it is employed in catalysts for olefin polymerization,[65] hydrogenation of alkenes,[66] reduction of NO,[67] and others. Because of this, Cr_2O_3 surfaces have been the topic of a number of experimental and theoretical studies.

A common way to prepare Cr_2O_3(0001) layers is the direct oxidation of Cr(110).[68] Also, preparation as a thin layer on Al_2O_3(0001), optionally with a Fe_2O_3 interlayer,[69] on Ag(111),[70] on Pd(111),[71] and on Cu(111)[72] has been reported. (0001) surfaces of Cr_2O_3 single crystals were also studied.[73] Cr_2O_3 has a corundum type structure and therefore three different ideal (0001) surface terminations, which may formally be obtained by cutting a Cr_2O_3 single crystal along the (0001) plane.[73,74] The corundum structure may be described as a (0001)-stacked sequence of quasi-hexagonal oxygen layers with three atoms in the two-dimensional unit cell (O_3) followed by two chromium layers with each of them having one Cr atom in the 2d unit cell. This arrangement is polar and belongs to type 2 in Taskers's classification scheme[43] (see Figure 11D−F); Cr−Cr−O_3 (Figure 22A), Cr−O_3−Cr (Figure 22(C), and O_3−Cr−Cr (Figure 22(B) are the possible (0001) surface terminations. The first and the last of these terminations are polar[43] and thus energetically unfavorable so that a surface terminated with a single chromium layer is expected.

The present understanding is that the surface is terminated by chromium ions in the topmost layer under oxygen-deficient conditions. However, different groups have proposed different arrangements of the chromium ions at the surface, partially with significantly modified surface interlayer distances. Some of the studies assume a partial, possibly statistical occupation of different chromium sites at the surface, and in many cases the agreement between model calculations and experiment was only moderate.

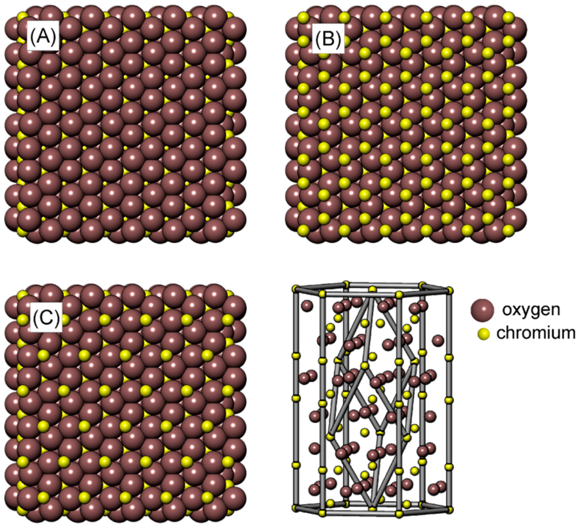

Figure 22. (A–C) Ideal surface terminations of $Cr_2O_3(0001)$. The bottom right panel displays the nonprimitive hexagonal and the primitive rhombohedral three-dimensional bulk unit cells.

A LEED I/V analysis study of $Cr_2O_3(0001)/Cr(110)$[74a,b] and a XPD study of $Cr_2O_3(0001)$ on Ag(111) found that the surface should exhibit ideal single-layer chromium termination,[70] while a XPD study for $Cr_2O_3(0001)$ on Pd(111) indicated that the surface is terminated with a chromium double layer.[71] On the other hand, a LEED I/V study of a $Cr_2O_3(0001)$ single-crystal surface proposed a surface with partial occupation of the two surface chromium layers.[73a] Partial occupation of the surface chromium layers with somewhat different concentrations and atomic coordinates was also proposed in a SXRD study of a $Cr_2O_3(0001)$ single-crystal surface.[73b]

A structural study of $Cr_2O_3(0001)/Cr(110)$ employing temperature-dependent LEED and EELS as well as cluster calculations proposed that the location of the chromium ions should be temperature dependent.[76] At low temperature, only sites of the bulk-truncated single-layer Cr-terminated surface were occupied. Raising the temperature led to the occupation of 3-fold hollow surface sites, which are not occupied in the bulk structure. At low temperature, an order–order phase transition was observed, which led to a $(\sqrt{3} \times \sqrt{3})R30°$ superstructure with maximum LEED spot intensity at 150 K that was followed by an order–disorder phase transition above 150 K.

A XPS/LEED/STM study of $Cr_2O_3(0001)$ on Cr(110) concluded that the surface should be chromium terminated with the density of chromium ions approximately corresponding to the density of single chromium layer of the bulk.[77] A statistical occupation of different chromium surface sites was proposed, while a SXRD study of a $Cr_2O_3(0001)$ single-crystal surface came to the conclusion that one-third of the surface chromium ions should be located in interstitial sites below the surface O_3 layer, which are unoccupied in the bulk structure.[74c]

All of these studies agree in that the surface is metal-terminated under the chosen preparation conditions, but the spread of the results may be an indication that preparation issues play a critical role. Also, contaminations may influence the results because the metal-terminated $Cr_2O_3(0001)$ surface is reactive as will be discussed below.

A number of theoretical papers have been published on the issue of the $Cr_2O_3(0001)$ surface termination.[75,78] Surface phase diagrams computed with GGA and GGA+*U* were published by Rohrbach et al.[75] (see Figure 23). These calculations indicate that at low oxygen chemical potentials, the nonpolar surface termination shown in Figure 22C is the equilibrium termination. At higher oxygen chemical potentials, a chromyl-terminated surface is formed (see Figure 24; such a surface is produced by coordinating oxygen atoms via double bonds to the surface chromium ions in Figure 22C). The formal oxidation state of the chromium ions at the surface changes from 3+ for the chromium-terminated surface to 5+ for the chromyl-terminated one. GGA+*U* finds oxygen-terminated surfaces at much higher oxygen chemical potentials than GGA, but yields rather similar results otherwise. According to the GGA calculations, also a termination with additional chromium ions between the surface O_3 and the first bulk O_3 layer (reminiscent of the structure proposed by Gloege et al.[74c]) may

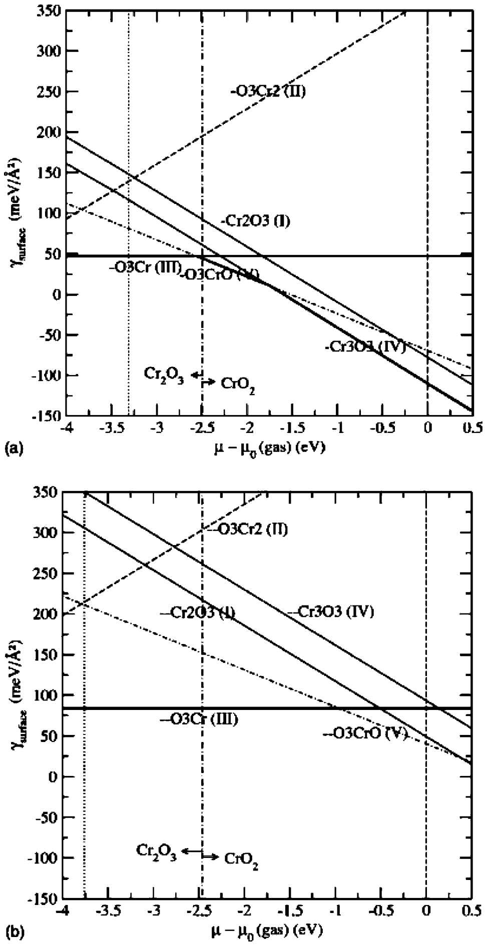

Figure 23. (a) GGA derived surface energies of the different $Cr_2O_3(0001)$ terminations plotted against oxygen chemical potentials. (b) GGA+*U* derived surface energies plotted against oxygen chemical potentials. The dotted and dashed vertical lines mark the upper and lower limits of the chemical potential as given by the condensation of molecular oxygen at the surface and the reduction of chromia to metallic Cr. The dot–dashed vertical lines mark the value of the chemical potential where the oxidation of Cr_2O_3 to CrO_2 becomes energetically favored. GGA+*U* calculations for CrO_2 have been performed with $U = 5$ eV, equal to Cr_2O_3. Reprinted with permission from ref 75. Copyright 2004 American Physical Society.

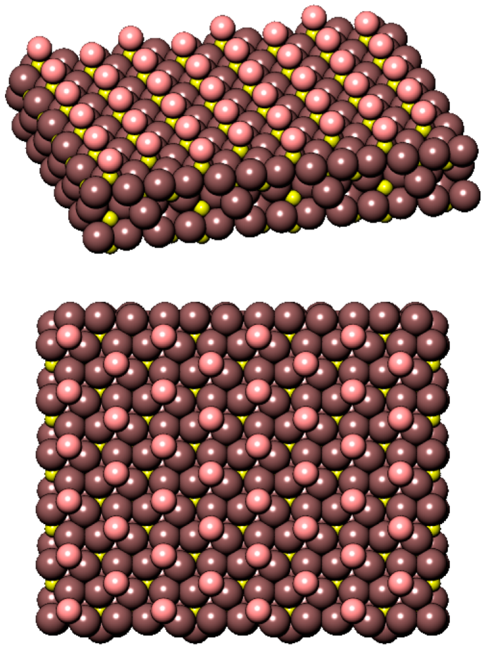

Figure 24. Top and perspective views of chromyl-terminated $Cr_2O_3(0001)$.

be relevant under conditions applied in experiments performed in typical UHV chambers. Preceding computations by Wang and Smith[78a] proposed the surface to be O_3-terminated (see Figure 22A) under common UHV conditions and not too high temperature. Annealing leads to a temperature-dependent chromyl concentration, while only at temperatures significantly above 1000 K is a chromium-terminated surface expected.[78a]

The formation of chromyl groups upon exposure of $Cr_2O_3(0001)$ to oxygen has been addressed in a number of experimental studies.[69,73b,79]

Using EELS, IRAS, and TPD, Dillman et al.[79a] found that oxygen is molecularly adsorbed below room temperature via formation of a "moderately strong chemisorptive bond", probably with a moderate charge transfer from the surface to the molecule. Above room temperature, the molecular oxygen species was found to dissociate leading to surface covered with chromyl groups. Similar to Dillmann et al.,[79a] Henderson et al.[79b] proposed the existence of a molecular oxygen species at low temperature, while exposure at 400 K should lead to chromyl groups. For oxygen dosing at 800 K, a complete capping of all surface chromium atoms with oxygen atoms was reported. A similar result was found after treatment with an O_2 plasma.[80] Bikondoa et al.[73b] proposed that a $O_3{-}Cr_{0.38}{=}O_{0.38}$ termination is formed at 10^{-2} mbar of O_2. In this surface termination, 38% of the single layer chromium surface sites are occupied by chromyl groups.

The adsorption of water on $Cr_2O_3(0001)$ was studied experimentally using LEED, STM, HREELS, TPD, and XPS.[69,81] Henderson and Chambers[69] found that water dissociates on metal-terminated $Cr_2O_3(0001)$. According to their results, a surface chromium ion binds an OH group, and the remaining hydrogen atom binds to a surface oxygen atom, forming a strong hydrogen bond to the oxygen atom of the former hydroxyl group. The latter bond is thought to be responsible for the unusually low observed O−H vibrational frequency of 2885 cm^{-1}. Figure 25 shows a sketch of the surface complex as proposed by Henderson and Chambers.[69]

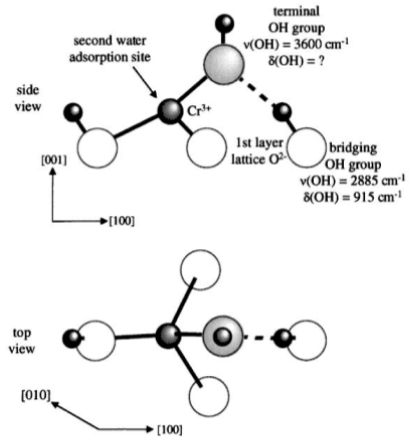

Figure 25. Schematic model for the structure of OH groups on Cr-terminated α-$Cr_2O_3(0001)$. Reprinted with permission from ref 69. Copyright 2000 Elsevier.

This complex is assumed to be able to also bind molecular water as indicated in the figure. Recombination and desorption of the hydroxyls occurs at 345 K. Chromyl groups were reported to block water dissociation.

Maurice et al.[81] investigated the hydroxylation of thin (5−6 layers thick) $Cr_2O_3(0001)$ films on Cr(110) with STM, LEED, and XPS. They report that surface hydroxylation occurs on regular sites as well as on step edges and grain boundaries. XPS studies for different waters doses at room temperature reveal three different steps in the hydroxylation process (see Figure 26). In the first step, water hydroxylates the surface chromium ions with the OH coverage reaching about 40% of that of the surface oxygen ion layer. In the second step, a further increase of the surface hydroxyl concentration up to a concentration of roughly one monolayer takes place, which is attributed to an oxidation of substrate chromium. The third step is a plateau where the concentration of the hydroxyl ions does not change very much.

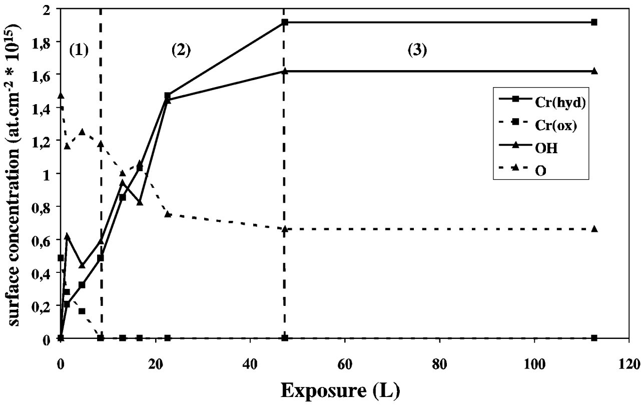

Figure 26. Variation of the atomic concentration of hydroxylation chromium, oxidized chromium, hydroxyl oxygen, and oxidic O^{2-} ions in the first plane of $Cr_2O_3(0001)$ thin films for increasing exposure to water vapor. Reprinted with permission from ref 81. Copyright 2001 Elsevier.

Chromium oxide is an essential component of the Phillips catalyst for the production of polyethylene from ethylene. Even nowadays the reaction mechanism of this single-site catalyst is under active discussion.[83] The interaction of ethylene with

$Cr_2O_3(0001)$ was studied by Hemmerich et al.[82] using XPS, IRAS, EELS, and TPD. They found reversible adsorption without reaction under UHV conditions, that is, for doses of some langmuirs at UHV-compatible pressures for chromium-terminated $Cr_2O_3(0001)$ as well as for $Cr_2O_3(0001)$ treated with oxygen to produce chromyl groups. Ethylene desorption occurs below 350 K. From XPS and IRAS data, it was concluded that at coverages below a monolayer the ethylene molecules are lying flat on the surface and that there is some charge transfer between the ethylene and the substrate. If the $Cr_2O_3(0001)$ surface is exposed to ethylene at atmospheric pressure at slightly above room temperature, then a more stable layer is formed. Annealing at 520 K does not lead to a complete attenuation of the C1s signal, which is found at a binding energy typical for polyethylene (see Figure 27). Infrared spectra also point toward polyethylene formation. It was suggested that polyethylene is formed at the surface chromium ions, which represents a still accepted view.[83]

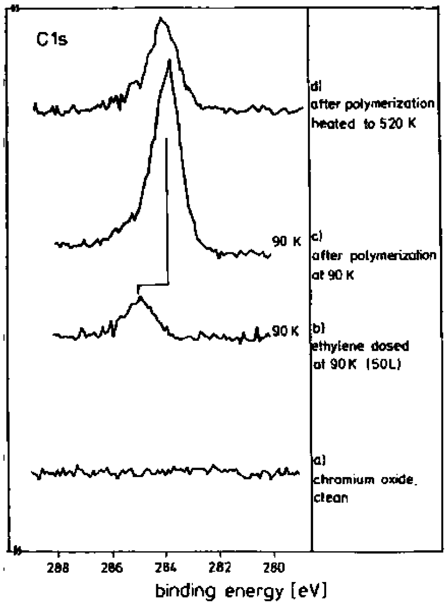

Figure 27. C1s XPS spectra of clean $Cr_2O_3(0001)$ and $Cr_2O_3(0001)$ after exposure to ethylene under low pressure conditions and 1 bar. Adapted with permission from ref 82. Copyright 1997 Oldenbourg.

CO_2 may adsorb molecularly unperturbed on surfaces, but also the formation of surface species like carbonates and carboxylates has been observed.[84] In the former case, the molecule coordinates to a surface oxygen ion, forming a $(CO_3)^{2-}$ unit, while in the latter case a surface metal atom transfers charge to the CO_2 molecule, and a negatively charged bent $CO_2^{\delta-}$ unit results. The interaction of CO_2 with $Cr_2O_3(0001)/Cr(110)$ was studied with TPD and IRAS.[85] Similar to what will be discussed at a later point for $V_2O_3(0001)$ and $V_2O_5(001)$, it was found that oxygen-terminated $Cr_2O_3(0001)$ does not react with CO_2; only molecular adsorption of CO_2 is observed. The presence of uncovered chromium sites was found to be a prerequisite for a strong interaction of CO_2 with the oxide. This situation will be discussed in the following.

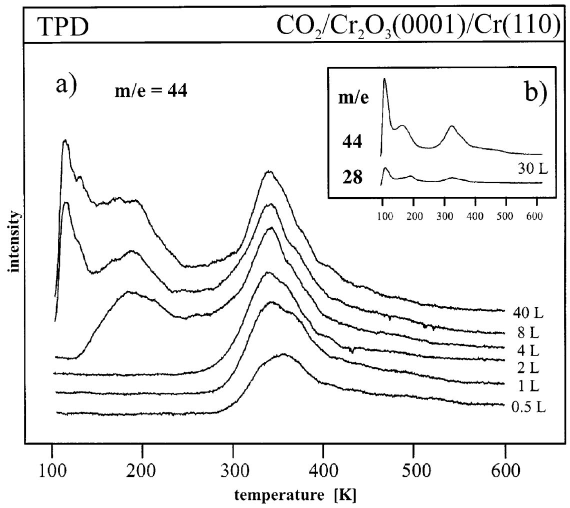

Figure 28. Thermal desorption spectra of CO_2 on $Cr_2O_3(0001)$. The inset compares TPD spectra of CO and CO_2 for a saturation coverage of CO_2. Adapted with permission from ref 85. Copyright 1999 Elsevier.

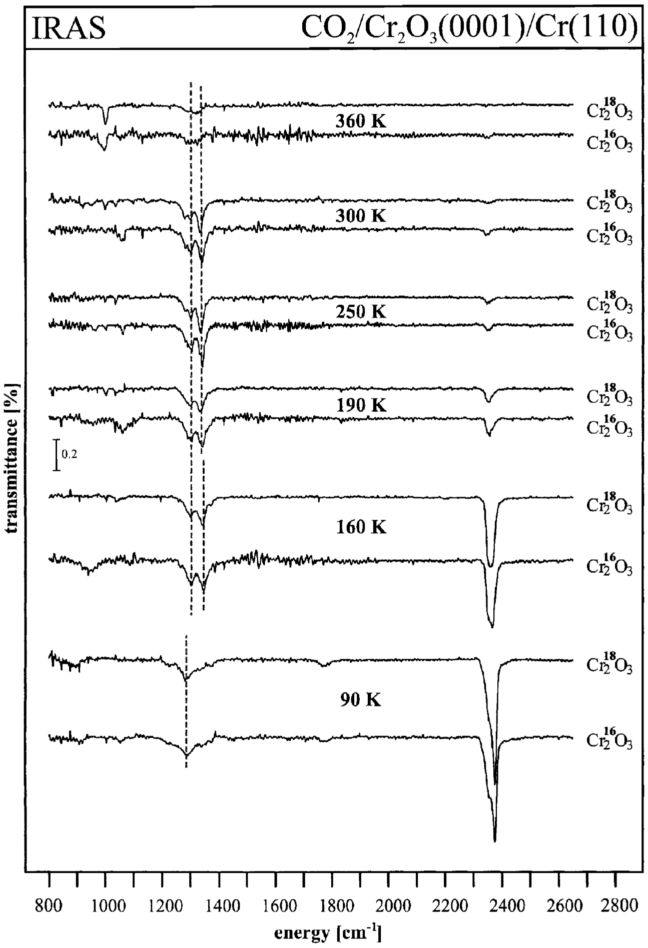

Figure 29. Infrared absorption spectra of CO_2 on $Cr_2O_3(0001)/Cr(110)$. The graph compares spectra for CO_2 on an oxide layer grown by oxidation of Cr(110) with ^{16}O and ^{18}O at dosing temperature (90 K) and after annealing at different temperatures. Adapted with permission from ref 85. Copyright 1999 Elsevier.

Figure 28 displays a set of TPD spectra obtained for CO_2 on $Cr_2O_3(0001)$, and Figure 29 shows IRAS spectra of CO_2 on $Cr_2{}^{18}O_3(0001)$ and $Cr_2{}^{16}O_3(0001)$ obtained after annealing at different temperatures and adsorption at 90 K. The desorption signals below ~250 K in Figure 28 correlate with the IR bands between 2300 and 2400 cm^{-1}, which are assigned to molecularly adsorbed linear CO_2. The desorption signals above ~300 K, on the other hand, are typical for a more strongly bound species such as carbonate or bent $CO_2^{\delta-}$. In the IR spectra in Figure 29, those species give rise to the bands in the range of ~1300 cm^{-1}. The IR data permit one to differentiate between these two possibilities: in the case of carbonate formation, one would expect differences in the vibrational spectra of CO_2 on $Cr_2{}^{18}O_3(0001)$ and $Cr_2{}^{16}O_3(0001)$ due to the bond of CO_2 to surface oxygen, while for $CO_2^{\delta-}$, no effect is expected because this species would be coordinated to metal ions. Thus, it is clear from Figure 29 that $CO_2^{\delta-}$ forms. From the missing antisymmetric $CO_2^{\delta-}$ stretching vibration at about 1500−1600 cm^{-1}, it was concluded that the molecule binds with the C_2 axis more or less perpendicular to the surface. In this case, the vibrational surface selection rule requires that this band is weak or invisible.

A modification of the $CO_2^{\delta-}$ vibrational structure after desorption of part of the linear CO_2 molecules upon warming to 160 K was observed, and attributed to a loss of solvation of $CO_2^{\delta-}$ by linear CO_2. Figure 30 graphically summarizes the results for CO_2 adsorption on $Cr_2O_3(0001)$. At low temperature, linear CO_2 is found on the surface, which gives rise to the two low-temperature CO_2 desorption peaks ~120 and ~180 K in Figure 28. IR data for CO_2 on oxygen-predosed $Cr_2O_3(0001)$ led to the conclusion that the more strongly bound species was linear CO_2 on oxygen sites, while the other one was assumed to be linear CO_2 coordinated to metal sites (C and D in Figure 30). The species A and B in Figure 30 are $CO_2^{\delta-}$ units in different geometries, while the complex S is a $CO_2^{\delta-}$ unit solvated by a CO_2 molecule. Carbonate species with structures similar to species F could not be identified.

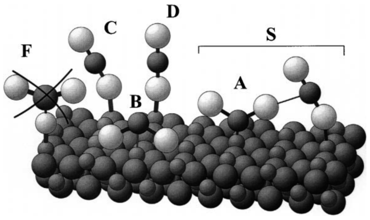

Figure 30. Overview of species identified after adsorption of CO_2 on $Cr_2O_3(0001)/Cr(110)$. Reprinted with permission from ref 85. Copyright 1999 Elsevier.

Adsorption of CO on $Cr_2O_3(0001)$ was studied in a number of theoretical and experimental publications.[68,86] The special geometry and bonding of CO to $Cr_2O_3(0001)$ was first addressed in detail in a photoelectron study in the 1990s.[68,86j]

Upon adsorption of CO onto $Cr_2O_3(0001)$, a $(\sqrt{3} \times \sqrt{3})R30°$ superstructure is observed in LEED. This superstructure is very sensitive to electron and photon irradiation; the LEED pattern faints after several seconds of observation. Because of this sensitivity, it was not possible to obtain a good photograph of this pattern.

CO desorbs from $Cr_2O_3(0001)$ at $T = 160$ K as revealed by TPD.[68] The adsorption enthalpy as calculated by the Redhead formula[30] is about 43 kJ/mol, which classifies the CO molecules as being weakly chemisorbed. Preadsorption of oxygen significantly lowers the CO peak area,[68] which indicates that surface chromium atoms are important for the adsorption of CO.

The ARUPS spectra in Figure 31 have been recorded with a fixed angle, that is, 90°, between the incident light beam and the direction of electron detection. The σ valence states of CO, that is, 4σ and 5σ, emit strongest along the molecular axis if the electric field vector of the exciting light points along this axis.[87] Thus, from the intensity of the σ ionizations as a function of the experimental geometry, the orientation of the molecules may be deduced. Two CO-induced features are visible, which are most intense at near perpendicular light incidence and accordingly near grazing electron exit angles. These peaks are located at binding energies of 11.8 and 14.3 eV with respect to the Fermi level, which are rather high binding energies for CO valence states. The σ valence states of the CO molecules emit strongly at the photon energy the spectra have been taken with, that is, 36 eV, due to the presence of the σ shape resonance, whereas the π states are rather weak at this photon energy.[87,88] For this reason, the ionizations at 14.3 and 11.8 eV were identified as being due to the CO σ valence states. Because these states emit strongest at near perpendicular light incidence and near grazing electron exit, it follows that the CO molecules must by lying more or less flat on the surface. In agreement with this finding, the σ shape resonance of the σ ion states was observed at grazing electron exit angles, whereas no intensity resonance is observed at normal electron emission as shown in Figure 32. The 1π intensity plotted in this figure has been obtained by a fitting procedure assuming the 1π ionization to be situated near the 4σ ionization as explained below. The conclusion that the CO molecules are essentially lying flat on the surface is supported by NEXAFS data and ARUPS data recorded in the so-called allowed and forbidden geometries.[68]

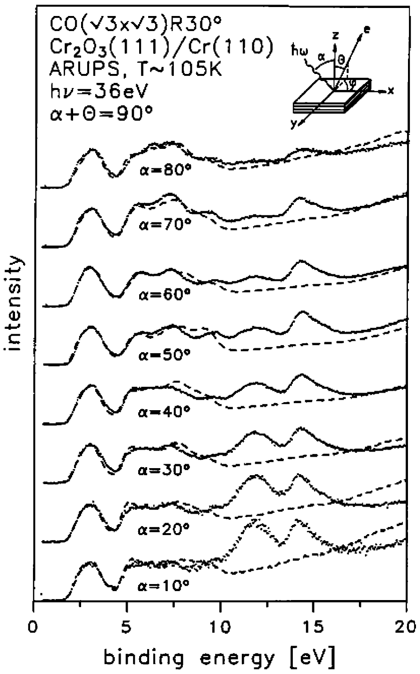

Figure 31. Series of ARUP spectra for CO adsorbed on $Cr_2O_3(111)$. The spectra have been taken such that the electron exit angle was always equivalent to the direction of the electric field vector of the incident light. For comparison, also in each case a spectrum of a flashed $Cr_2O_3(111)$ surface is shown. Reprinted with permission from ref 68. Copyright 1992 German Bunsen Society for Physical Chemistry.

For CO molecules lying flat on the surface, the 1π orbitals are expected to be split into two components for symmetry reasons. One component should be oriented parallel to the surface ($1\pi_{xy}$), whereas the other one should stick out of the

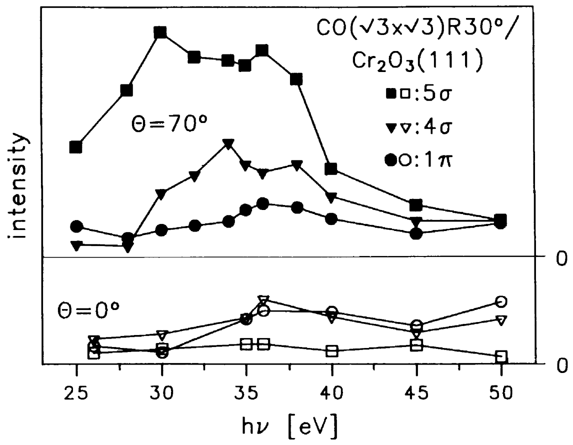

Figure 32. Intensities of the CO valence ionizations as a function of the photon energy plotted for two different experimental geometries. Upper panel: Near perpendicular light incidence and grazing electron detection ($\theta = 70°$). Lower panel: Grazing light incidence and normal electron detection ($\theta = 0°$). Reprinted with permission from ref 68. Copyright 1992 German Bunsen Society for Physical Chemistry.

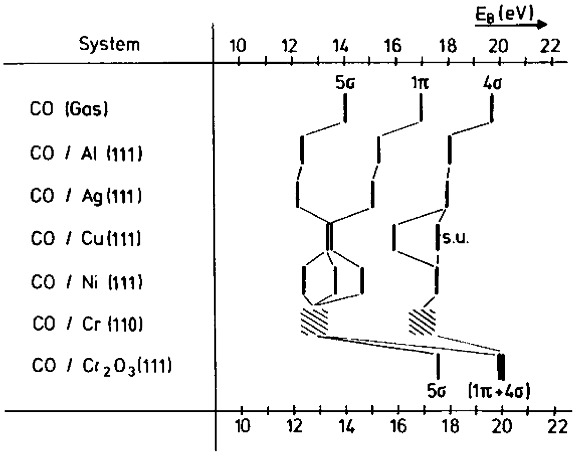

Figure 33. Comparison of electronic valence binding energies for CO adsorbed on different substrates. The binding energies are referenced to the vacuum level of the respective adsorption system. Because the work function for CO/Cr(110) is not known, the regions in which the ionizations are expected to occur have been hatched. Data have been taken from refs 45−50. Reprinted with permission from ref 68. Copyright 1992 German Bunsen Society for Physical Chemistry.

surface plane ($1\pi_z$). The $1\pi_{xy}$ level should be intense at angles where the σ levels are also intense because the latter levels are also oriented parallel to the surface plane. Therefore, the $1\pi_{xy}$ emission might be hidden below the strong σ emissions. On the other hand, the $1\pi_z$ emission should be intense when the σ emission is weak, that is, at normal electron emission. The $1\pi_z$ level will interact strongly with the substrate, which shifts this level to higher binding energy because the substrate levels are located at lower binding energy than the 1π orbitals. Thus, the $1\pi_z$ level is most likely not energetically situated in the region of the substrate levels but somewhere below. As can be seen from the spectra shown in Figure 31, the 5σ emission at 11.8 eV binding energy is totally suppressed at near normal electron emission. If the $1\pi_z$ level were located near the 5σ level, there should be some remaining intensity because the $1\pi_z$ level would show up in this geometry. Because this is not the case, it is concluded that for CO adsorbed on $Cr_2O_3(0001)$, the $1\pi_z$ valence ionization is not energetically close to the 5σ ionization as is the case for CO on most metals.

Inspection of Figure 31 shows that a broad feature remains in the region of the 4σ emission between 13 and 16 eV. Because the 4σ and 5σ intensities should behave similar to some extent, it is tempting to attribute this intensity to the CO $1\pi_z$ level. If it is true that the $1\pi_z$ is near the 4σ, then the interaction of the $1\pi_z$ with the substrate must be unusually strong and different from what is known for typical CO adsorbates. Figure 33 compares CO binding energies for different substrates.[89] The binding energies are referred to the vacuum level of the respective adsorbate system. For CO adsorbed on $Cr_2O_3(0001)$, the binding energies of all valence levels are larger than the binding energies observed so far for metallic substrates.

This result may be rationalized with the following model: the CO σ lone pairs interact with surface chromium atoms, building up σ bonds toward these ions and shifting the σ levels to higher binding energies. The 1π levels, on the other hand, additionally interact with the oxygen atoms below the molecule. Because the O^{2-} ions are in a closed-shell configuration, this interaction will be basically repulsive. The O^{2-} levels of the oxide are situated at lower binding energies than the CO 1π levels so that O^{2-} levels will be shifted to lower binding energies, whereas the 1π levels are energetically stabilized. For the $1\pi_z$ level, this effect is obvious from Figure 33. Because the interaction of the 1π levels with the oxygen atoms will be repulsive, the interaction of the σ orbitals with the chromium atoms must be bonding because otherwise the CO molecules would not adsorb on the surface.

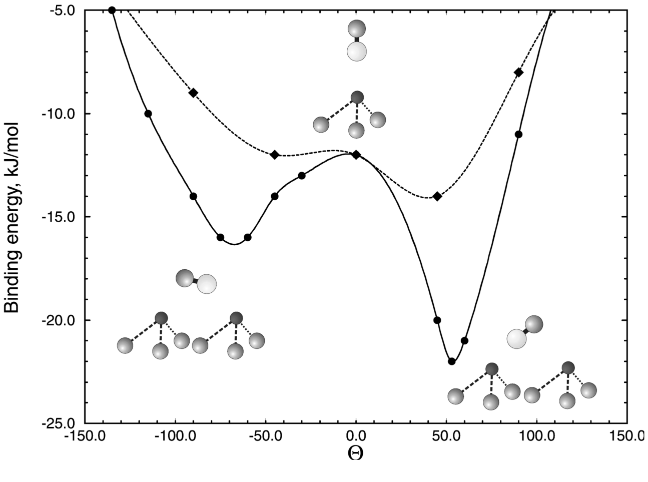

Figure 34. Potential energy curves for the interaction of CO with the $Cr_2O_3(0001)$ surface. SCF approximation: Embedded $Cr_3O_6^{6-}$ cluster. (●) 40% and (◆) 60% relaxation of the topmost Cr−O interlayer distance. Reprinted with permission from ref 86e. Copyright 2001 Elsevier.

Somewhat later, a mixed theoretical/experimental study of the system CO on chromium-terminated $Cr_2O_3(0001)$ was published.[86e] Using quantum-chemical cluster calculations, a potential energy curve was computed, which showed pronounced energetic minima for strongly tilted CO molecules (see Figure 34). The calculation was performed for different relaxations of the topmost Cr−O interlayer distance because a LEED study had shown that this distance is considerably smaller than the bulk value.[74a,b] The results depend strongly on the relaxation, but this graph essentially supports the conclusions that the CO molecules might be lying flat on the surface. It was noted that lateral interactions, which probably play a role in the experiments, were not considered in the calculations.

It is evident from this discussion that the bonding of CO to $Cr_2O_3(0001)$ is significantly different from the standard type of bonding of CO to metallic surfaces as described by the Blyholder model[90] where the 1π levels do not contribute significantly to the CO−substrate interaction. However, there are cases like CO on Cr(110)[89f,91] that are different. In this case, the CO molecules are strongly tilted and near dissociation. Because of the strong tilt, there is also a strong interaction between the 1π levels and the Cr(110) substrate.

5. VANADIUM OXIDE: $V_2O_3(0001)$

There are a number of reasons vanadium oxides have been studied: the magnetic properties of V_2O_3[92] and its phase transitions[93] triggered studies in solid-state physics. Technical applications such as smart windows and vanadium oxide-based lithium battery cathodes inspired also a number of investigations.[94] The probably most common reason to study vanadium oxides is the relevance of the vanadium−oxygen system for catalysis. The vanadium−oxygen system is characterized by many different oxide compounds: beyond the simple binary compounds VO (V^{2+}), V_2O_3 (V^{3+}), VO_2 (V^{4+}), and V_2O_5 (V^{5+}), there are also a number of mixed-valence compounds such as Magnéli phases V_nO_{2n-1} and Wadsley phases $V_{2n}O_{5n-1}$. The variability of the vanadium oxidation state has the consequence that vanadium oxides can catalyze reactions involving oxidation or oxygen transfer.[95] In most cases, supported V_2O_5 is employed together with other oxides to improve stability, reactivity, and selectivity.[96]

The oxy-dehydrogenation of methanol toward formaldehyde ($CH_3OH + O \rightarrow CH_2O + H_2O$) is a reaction that consumes oxygen. It is well-known that supported vanadia catalyzes this reaction.[97] This reaction has been studied for $V_2O_3(0001)$ and $V_2O_5(001)$ substrates with a special focus on the role of hydroxyl groups. The partial methanol oxidation reaction consumes oxygen, and therefore the interaction of oxygen with the surface and its state on the surface are important parameters that have been studied independently. Surface hydroxyl groups are formed in the course of the reaction. They lead to the production of water, which is the reason also the interaction of the surface with water was investigated. A rather general result of the studies on $V_2O_3(0001)$ and $V_2O_5(001)$ is that the surfaces obtained directly after preparation are not very active. To activate them, it is required to produce surface oxygen vacancies, which may be achieved via electron irradiation.[98]

Well-ordered $V_2O_3(0001)$ layers were grown on several substrates including Au(111),[98d,e] W(110),[98c] Rh(111),[100] Pd(111),[101] and $Cu_3Au(100)$.[102] A typical preparation procedure is deposition of vanadium at elevated temperature in an oxygen ambient atmosphere of $\sim 10^{-6}$ mbar, followed by an annealing post-treatment.[98c,e] V_2O_3 is an oxide with a corundum-type structure where the (0001) surface is quasi-hexagonal. A STM image obtained directly after preparation of a ~70 Å thick layer is shown in Figure 35. The image exhibits the expected 3-fold symmetry, but the details of the surface termination are not fully understood at present. Vibrational spectroscopy, STM,[101c] and XPS[98c,d] indicate that the surface is terminated by a layer of vanadyl groups, whereas medium-energy/low-energy ion scattering studies[103] and ion beam triangulation[104] favor the modified O_3 termination as introduced by Kresse,[99] where the surface is terminated by a quasi-hexagonal oxygen layer. One vanadium atom from a deeper layer pops up into the area below the surface oxygen layer, and a VO_2 type surface structure results (see Figure 36b).

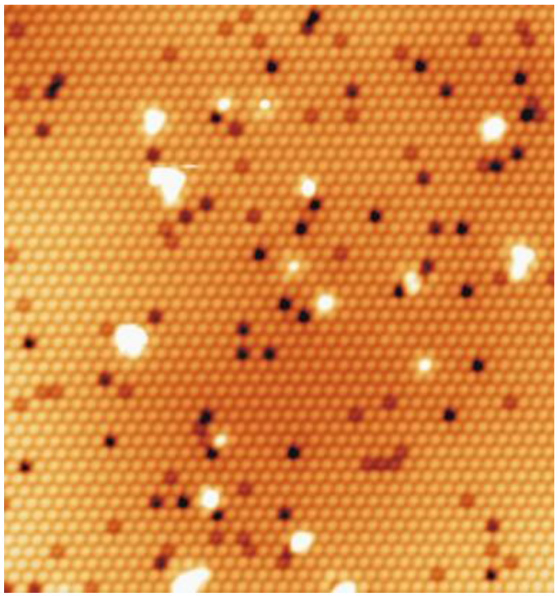

Figure 35. STM image of oxygen-terminated $V_2O_3(0001)$. Area: 200 × 200 Å^2. Tunneling conditions: $V = -1.5$ V, $I = 0.2$ nA. Reprinted with permission from ref 98a. Copyright 2011 Springer.

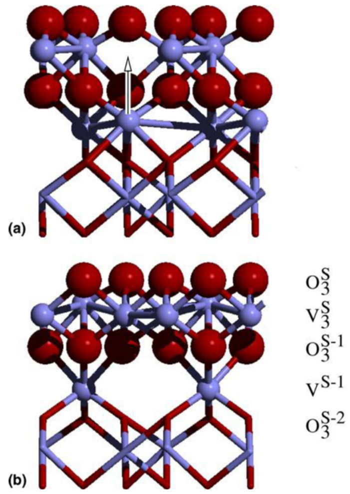

Figure 36. (a) Ideal O_3 termination of corundum, and (b) energetically most stable termination. Reprinted with permission from ref 99. Copyright 2004 Elsevier.

This contradiction is not settled at present. A surface phase diagram has been computed by Kresse et al.[99] (for thin layers on $Al_2O_3(0001)$, see also Todorova et al.[105]). The stability range for the O_3 termination according to this diagram (see Figure 37) may be reached during the preparation of $V_2O_3(0001)$ layers, which typically involves temperatures of up to 900 K and oxygen pressures in the 10^{-6} mbar range. However, annealing in UHV or surface reduction might stabilize a different termination. Because the surface termination must be considered as being unknown at present, the term "surface oxygen layer" is used for the topmost oxygen layer, which would be a vanadyl layer or an O_3 layer, and the term "oxygen termination" is used for the surface termination.

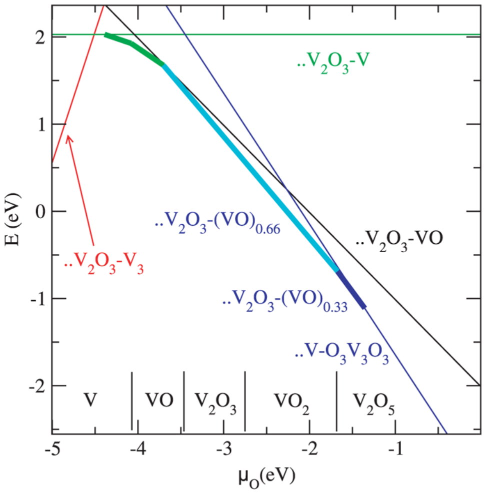

Figure 37. Surface energy per primitive surface cell versus chemical potential of oxygen μ_O for the (0001) surface of rhombohedral V_2O_3. Thin lines correspond to calculations for the primitive surface cell, whereas thick shorter lines correspond to "reconstructed" cells with a periodicity of $(\sqrt{3} \times \sqrt{3})$R30°. The thick lines between V_2O_3−V and V_2O_3−VO correspond to mixed V_2O_3−$V_x(VO)_{1-x}$ phases. The stability regime of the bulk oxides is indicated at the bottom of the graph. Reprinted with permission from ref 99. Copyright 2004 Elsevier.

Irradiation with electrons reduces the surface.[98c] Low doses lead to an increase of the number of point defects,[98a] which have an appearance similar to the dark features in Figure 35, whereas large electron doses lead to a metal-terminated surface, which is characterized by missing vanadyl vibrations in the vibrational spectra.[98d] Such surfaces are much more reactive than the oxygen-terminated ones as will be shown in the following. A STM image published by Guimond et al.[106] for a surface without vanadyl vibrations shows an ordered structure with a number of defects. Yet unpublished IV-LEED calculations indicate that this surface is terminated by a single vanadium layer, which would be in agreement with STM. The freely accessible surface vanadium atoms are probably the reason for the high reactivity of the surface. A schematic model for vanadium-terminated $V_2O_3(0001)$ is shown in Figure 38.

The surface reduction is a reversible process. Annealing the surface in oxygen re-establishes the original vanadyl- or O_3-terminated surface. The interaction of the surface with oxygen has been studied in detail with infrared spectroscopy, photoelectron spectroscopy, HREELS, and density functional theory.[98d]

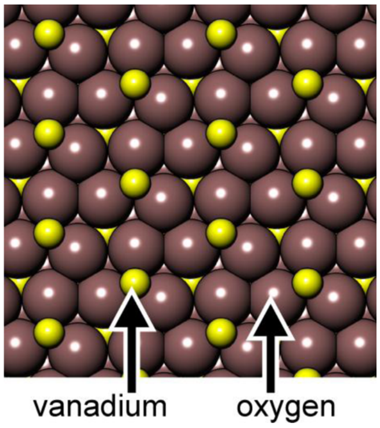

Figure 38. Structural model of vanadium-terminated $V_2O_3(0001)$.

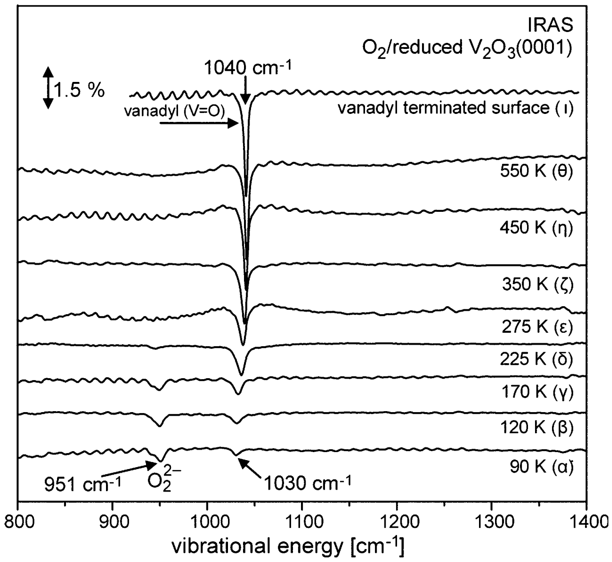

Figure 39. IRAS spectra of oxygen on reduced $V_2O_3(0001)$ as a function of temperature after dosing 15 L O_2 at 90 K. At the top a spectrum of the oxygen-terminated $V_2O_3(0001)$ surface is shown. All spectra are referenced to a spectrum of the reduced surface; that is, the spectra shown in this figure result from a division of an absorption spectrum of an oxygen-covered or oxygen-terminated surface by a spectrum of the reduced surface. Reprinted with permission from ref 98d. Copyright 2006 Elsevier.

Figure 39 displays IRAS spectra taken from a reduced $V_2O_3(0001)$ surface after exposure to O_2 at 90 K as a function of the annealing temperature. At low temperature, two bands at 951 and 1030 cm^{-1} are observed. The band at 1030 cm^{-1} is assigned to the vanadyl vibration;[98c] an assignment of this band to vibrations of the O_3 termination is not easily possible according to calculations.[99] The vanadyl-induced feature increases in intensity and shifts to higher frequency (up to 1040 cm^{-1}) upon annealing above 170 K, while the band at 951 cm^{-1} vanishes. The 951 cm^{-1} band falls into the 900−1100 cm^{-1} range,[107] which is typical of peroxo (O_2^{2-}) surface species, while superoxide O_2^{2-} species exhibit characteristic vibrations in the range of 1100−1150 cm^{-1}.[107] On the basis of this knowledge, the existence of peroxo species on the $V_2O_3(0001)$ surface was proposed.

Spin-polarized DFT calculations on the structure and vibrational properties of oxygen species adsorbed on $V_2O_3(0001)$ were performed to support this assignment. The surface was modeled by a finite cluster and by a periodic slab (sees Figure 40). In the optimized structure of the O_2/cluster complex, the O_2 ligand is aligned parallel to the surface in an η^2-mode with an O−O distance of 144.4 pm and V−O distance of 182.7 pm, whereas in the periodic structure the O_2 species are slightly tilted with respect to the surface plane in accord with the local C_{3v} symmetry of the VO_3 surface unit (upper part of Figure 40). The V−O distances are 180.3 and 183.6 pm, and the O−O distance is 143.6 pm.

The frequency calculations for the peroxo species on $V_2O_3(0001)$ yield a quite intense IR-active mode at 904 cm^{-1} (cluster model) or 960 cm^{-1} (periodic model). It corresponds to the O−O valence stretching of the peroxo species. The

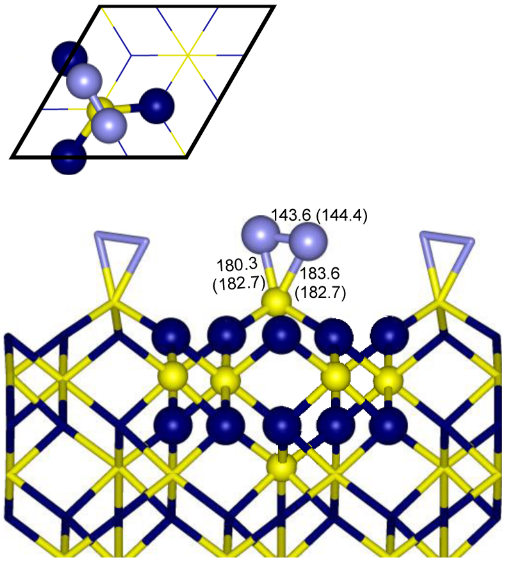

Figure 40. Side view of the O_2^{2-} species on the $V_2O_3(0001)$ surface. Vanadium atoms are yellow, oxygen atoms of the slab are dark blue, whereas those of O_2^{2-} are light blue. Balls and sticks are used to indicate the cluster model cut out from the $V_2O_3(0001)$ surface. Bond lengths for the slab and the cluster (in parentheses) are given in pm. The top view (upper part) shows the orientation of the O_2^{2-} species relative to the VO_3 surface unit. Reprinted with permission from ref 98d. Copyright 2006 Elsevier.

experimental vibrational energy of 951 cm^{-1} is in excellent agreement with the 960 cm^{-1} predicted for the peroxo species with the periodic model.

Water adsorption on $V_2O_3(0001)$ has been studied by different groups using photoelectron spectroscopy, vibrational spectroscopy, TPD, STM, DFT, and PED.[98e,108] XPS spectra of the O1s and V2p core level region of water on reduced and oxygen-terminated $V_2O_3(0001)$ are displayed in Figure 41 for different annealing temperatures. At temperatures $T \leq 165$ K, the typical levels of ice show up in the data. Further annealing leads to an O1s peak at around 533.5 eV in the case of the oxygen-terminated surface (Figure 41b). This level may be attributed to molecular water (a list of O1s binding energies of water on different substrates may be found in ref 109, p 16). No indication of water dissociation was observed.

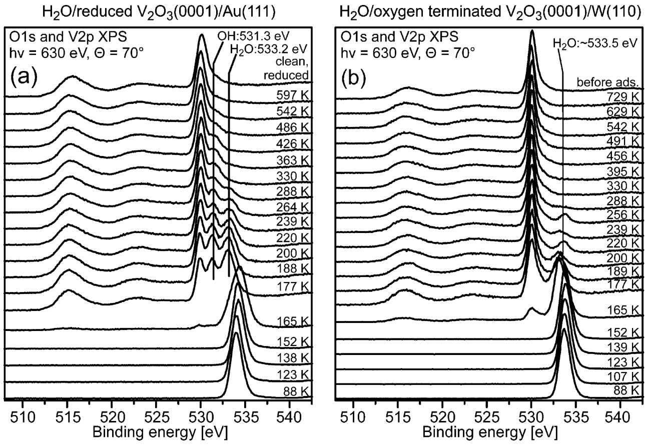

Figure 41. Photoelectron spectra of the O1s+V2p region of water on oxygen-terminated and reduced $V_2O_3(0001)$ as a function of the annealing temperature. Multilayers of water were adsorbed at 88 K. Before acquiring the spectra for a certain temperature, the sample was shortly annealed at this temperature. After this, the sample was cooled, and the spectra were recorded at low temperature. Adapted with permission from ref 98e. Copyright 2006 Elsevier.

In the XPS core level data of the reduced surface (Figure 41a), two water-induced O1s levels at 531.3 and 533.2 eV are found after removal of the ice layer ($T \geq 177$ K). The feature at higher binding energy may be assigned to molecular water, and the level at 531.3 eV in the spectra of the reduced surface is due to surface hydroxyl groups,[110] which disappear from the surface at $T \leq 600$ K, whereas the molecular water desorbs below 330 K. The OH coverage on the reduced surface was estimated using the O1s XPS intensities of the substrate and the hydroxyl groups with the result that at 188 K the hydroxyl coverage is ~1.6 groups per surface unit cell and that at 363 K the calculated hydroxyl coverage drops to ~1.1. These numbers represent only rough estimates because the inelastic mean free electron path length is not known exactly, and because electron diffraction effects, which may have a significant influence at kinetic energies near 100 eV, have not been considered. Using photoelectron diffraction, Kröger et al.[108b] concluded that the hydrogen atoms of the OH groups are coordinated to the oxygen layer below the surface vanadium layer. OH groups bound to the surface vanadium atoms were not observed. In this publication, it was estimated that 2/3 to all of the atoms of the oxygen layer are hydroxylated.

Figure 42 compares thermal desorption spectra of 2 L of H_2O on reduced and oxygen-terminated $V_2O_3(0001)$/Au(111).

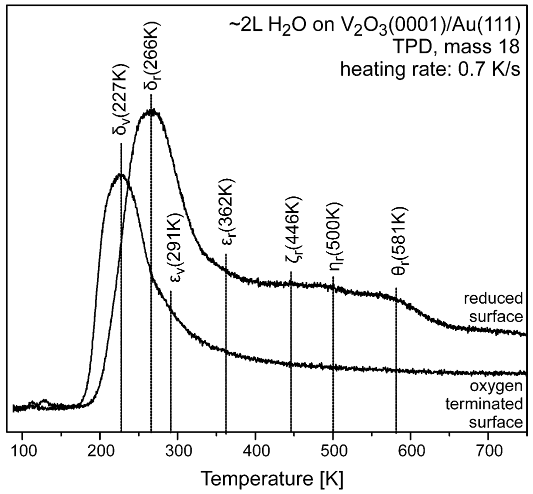

Figure 42. Comparison of TPD spectra obtained after dosing of 2 L of water on reduced and oxygen-terminated $V_2O_3(0001)$ (c). The identified desorption maxima are marked and enumerated by Greek letters in the spectra, and the desorption temperatures are indicated. The indices "r" and "v" refer to the reduced and the oxygen-terminated surface, respectively. Reproduced with permission from ref 98e. Copyright 2006 Elsevier.

The spectrum of water on the oxygen-terminated surface essentially only exhibits a broad desorption peak with a maximum at $T \approx 227$ K, which may be attributed to a molecular (sub)monolayer of water, as was also deduced from the O1s XPS data shown in Figure 41b. The intensity smoothly levels off toward higher temperature, and no additional structure appears (except for a weak shoulder at 291 K).

In the case of the reduced surface, the desorption peak of molecular water in Figure 42 is shifted toward higher temperature with its maximum now appearing at 266 K, which points toward a slightly stronger bond to the surface and/or within the layer. Additional broad structures are visible up to a temperature of about 600 K. Because this is approximately the temperature at which the hydroxyl-induced signals in the XPS data (Figure 41a) disappear, it is near at hand to assume that these desorption states are related to the disappearance of the hydroxyl groups. Because this process obviously leads to water desorption, the water fragments must recombine on the surface before desorption.

With the activity of vanadia for oxygen transfer reactions in mind, the reaction of methanol toward formaldehyde was studied for $V_2O_3(0001)$ and $V_2O_5(100)$. Special attention was paid to the role of surface hydroxyls during the reaction.

The production of formaldehyde from methanol via oxydehydrogenation consumes oxygen, which has to be provided by the substrate surface. To investigate the role of surface oxygen atoms in this process on $V_2O_3(0001)$, surfaces were produced where part of the surface oxygen atoms was removed. These surfaces were dosed with methanol, and the reaction was studied with several methods.

Figure 43 shows TPD data for a methanol adsorbate on $V_2O_3(0001)$ for different degrees of surface reduction. The mass cracking pattern of Methanol exhibits intensity at masses 29 and 31, while formaldehyde intensity is found at mass 29 but not at mass 31 according to data published on the NIST WebBook site.[111] Therefore, identical structures in the mass spectra at masses 29 and 31 are due to methanol, while structures that are found in the mass 29 spectrum, but not in the mass 31 spectrum, are a consequence of formaldehyde desorption. Considering this, it is clear from Figure 43B that formaldehyde desorption occurs between 470 and 620 K.

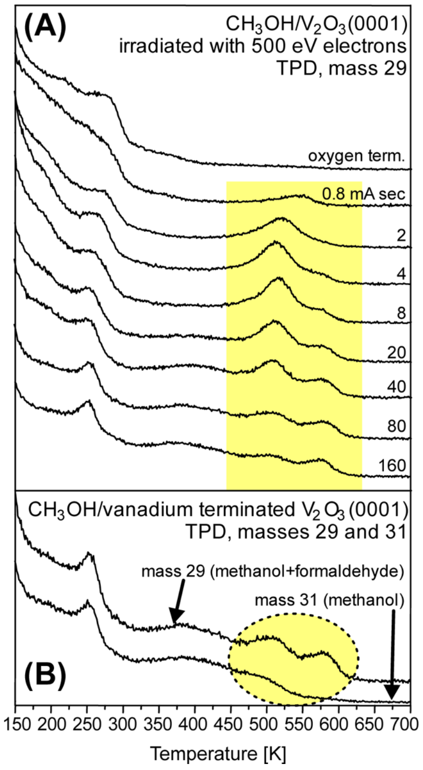

Figure 43. (A) Series of TPD spectra (mass 29: methanol +formaldehyde) of methanol on $V_2O_3(0001)$ as a function of the dose of electrons employed to produce surface oxygen vacancies. (B) TPD spectra of masses 29 (methanol+formaldehyde) and 31 (methanol only) of methanol on vanadium-terminated $V_2O_3(0001)$. Multilayer amounts of methanol were dosed at 90 K. Reprinted with permission from ref 98a. Copyright 2011 Springer.

Figure 43A shows that the nonreduced surface (oxygen-terminated) is inactive for formaldehyde production, while the electron-irradiated, reduced surfaces are active, with the formaldehyde yield depending on the degree of reduction. The low-temperature peak has an intensity maximum at an electron dose of 4−8 mC, while the intensity of the high-temperature state increases with increasing electron dose.

An electron dose of about 80 mC removes more or less all surface oxygen atoms according to STM data[106] (not shown here). From this it follows that the high-temperature peak is likely due to surface areas without vanadyl/O_3 oxygen atoms, while the low-temperature state is probably related to surface areas where such oxygen atoms are within reach.

STM was employed to study the formation of methoxy groups for low degrees of surface reduction. Figure 44 displays (from left to right) images of an as-prepared nonreduced surface, a surface reduced by electron irradiation, and a reduced surface after dosage of methanol at 90 K followed by a flash at 400 K to remove molecularly adsorbed methanol. Methoxy groups are clearly recognizable in the right image, together with some defects that are probably those seen in the image of the nonreduced surface because these are inactive for formaldehyde production (see Figure 43).

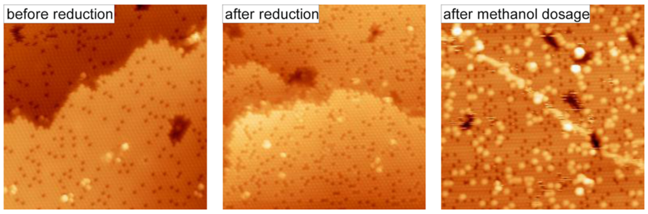

Figure 44. Room-temperature STM images of nonreduced $V_2O_3(0001)$ (left), reduced $V_2O_3(0001)$ (center), and methoxy covered $V_2O_3(0001)$ (right). Surface reduction was achieved by irradiation with 1.5 mC of 50 eV electrons. Tunneling voltage: −1.5 V. Tunneling current: 0.2 nA. Area: 25 × 25 nm^2. Adapted with permission from ref 98a. Copyright 2011 Springer.

The density of defects produced by electron irradiation and the density of methoxy groups are plotted in Figure 45 as a function of electron dose. Because the defects on the as-prepared surfaces are inactive, their density was subtracted from the defects density of the electron-irradiated surfaces.

Figure 45 indicates that one surface defect leads to the formation of two methoxy groups. This relationship is well fulfilled for the data obtained with 500 eV electrons, while for the data obtained with 50 eV electrons there is a deviation that may be related to experimental uncertainties but may also have physical, yet unidentified reasons.

The somewhat unexpected result that there are twice as many methoxy groups as electron-induced defects may be rationalized by considering that not only methoxy groups form when methanol is adsorbed, but also hydroxyl groups. These can react to form water, thereby producing additional oxygen vacancies.

When methanol is adsorbed at 85 K, the first step of the reaction occurs:

$$n\mathrm{CH_3OH} + n\mathrm{V} + n\mathrm{O} \rightarrow n\mathrm{CH_3OV} + n\mathrm{OH} \qquad (2)$$

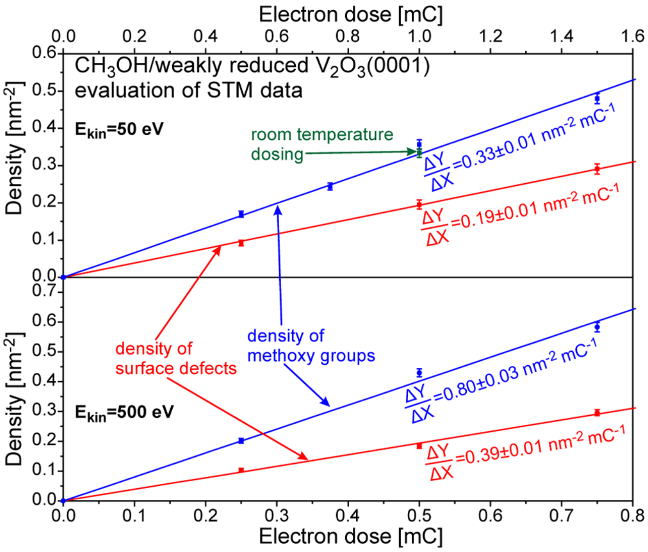

Figure 45. Density of defects induced by electron irradiation as a function of the electron dose for two electron energies (E = 50 eV and E = 500 eV) and the corresponding density of methoxy groups after methanol dosage at 90 K followed by a flash to 400 K as obtained from STM images. Reprinted with permission from ref 98a. Copyright 2011 Springer.

Here, n methanol molecules interact with n surface defects (vanadium sites, denoted by "V") and n surface oxygen sites ("O") to form n methoxy ("CH_3OV") and n hydroxy groups ("OH"). Water formation via reaction of two hydroxyl groups occurs at ~270 K (not shown here). This reaction also produces oxygen and vanadium sites (reaction step 3), which are available to react with adsorbed methanol to form additional methoxy and hydroxy groups (reaction step 4):

$$n\mathrm{OH} \rightarrow \frac{n}{2}\mathrm{H_2O} + \frac{n}{2}\mathrm{O} + \frac{n}{2}\mathrm{V} \tag{3}$$

$$\frac{n}{2}\mathrm{CH_3OH} + \frac{n}{2}\mathrm{V} + \frac{n}{2}\mathrm{O} \rightarrow \frac{n}{2}\mathrm{CH_3OV} + \frac{n}{2}\mathrm{OH} \tag{4}$$

In reaction step 5, again water is produced together with oxygen and vanadium sites, which react with methanol to form more methoxy and hydroxy groups (reaction step 6):

$$\frac{n}{2}\mathrm{OH} \rightarrow \frac{n}{4}\mathrm{H_2O} + \frac{n}{4}\mathrm{O} + \frac{n}{4}\mathrm{V} \tag{5}$$

$$\frac{n}{4}\mathrm{CH_3OH} + \frac{n}{4}\mathrm{V} + \frac{n}{4}\mathrm{O} \rightarrow \frac{n}{4}\mathrm{CH_3OV} + \frac{n}{4}\mathrm{OH} \tag{6}$$

The number of produced defect sites decreases more and more when the reaction goes on, and finally the reaction, which may be viewed as a self-limiting chain reaction, stops after some time when the number of produced/available defect sites approaches zero. In total, $2n$ methoxy groups are produced on a surface with n defects, which agrees well with the data in Figure 45:

$$\begin{aligned} &n\mathrm{CH_3OV} + \frac{n}{2}\mathrm{CH_3OV} + \frac{n}{4}\mathrm{CH_3OV} + \frac{n}{8}\mathrm{CH_3OV} + ... \\ &\quad = 2n\mathrm{CH_3OV} \end{aligned} \tag{7}$$

The formation of additional defects due to the reaction of hydroxyl groups to form water and the subsequent formation of additional methoxy groups starts at 270 K. As a consequence, the intensity of the methoxy C−O vibrational intensity increases when the sample is warmed from 240 to 270 K[98a] (not shown here).

Formaldehyde is also produced on metal-terminated $V_2O_3(0001)$, that is, on a surface where the surface oxygen layer was completely removed, However, STM data are not available in this case, but some conclusions may be drawn from the existing TPD, IRAS, and PES data. Figure 46B shows that water desorbs at ~240 K, and at this temperature the intensity of the methoxy C−O vibrational band increases significantly in infrared data[98a] (not shown here). This is similar to what was observed for the weakly reduced surface, and therefore it is near at hand to assume that a similar reaction mechanism is active for the metal-terminated surface. The water desorption temperature is somewhat different, which is probably due to the much higher degree of surface reduction.

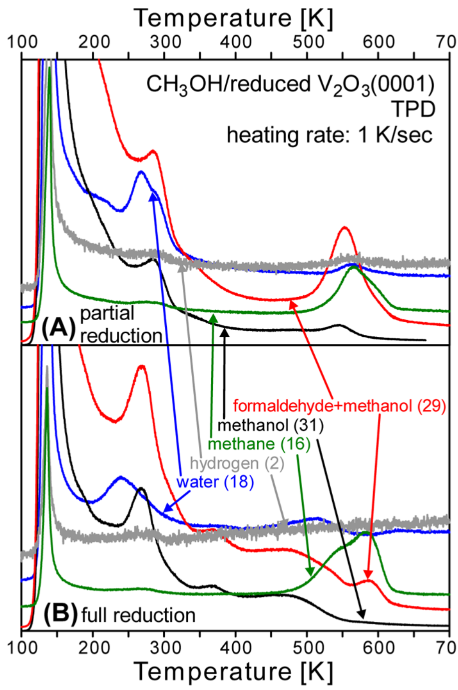

Figure 46. Thermal desorption spectra of methanol on partially and fully reduced $V_2O_3(0001)$. The top panel (A) shows data for a partially reduced surface (electron dose: 2 mC), and the bottom panel (B) displays data for a fully reduced surface (electron dose: 80 mC). Methanol was adsorbed in multilayer amounts at 90 K. Reprinted with permission from ref 98a. Copyright 2011 Springer.

TPD spectra of methanol adsorbed on a weakly reduced oxide layer containing a mixture of ^{16}O and ^{18}O are shown in Figure 47. In this case, formaldehyde with ^{18}O desorbs from the surface as demonstrated by the presence of formaldehyde intensity in the spectrum obtained for mass 31. Because the adsorbed methanol molecules did not contain ^{18}O, the ^{18}O in the formaldehyde must stem from the substrate. For chromia[112] and ceria[113] substrates, it was proposed that formaldehyde formation occurs via a dioxymethylene (O_2CH_2) intermediate. This is a CH_2 group coordinated to the substrate via two oxygen atoms. One atom would be the oxygen atom from the methanol molecule (^{16}O), and the other one would be a substrate oxygen atom (^{18}O). One of the bonds breaks when formaldehyde forms, and whether the molecule finally contains ^{18}O or ^{16}O depended on which bond was broken.

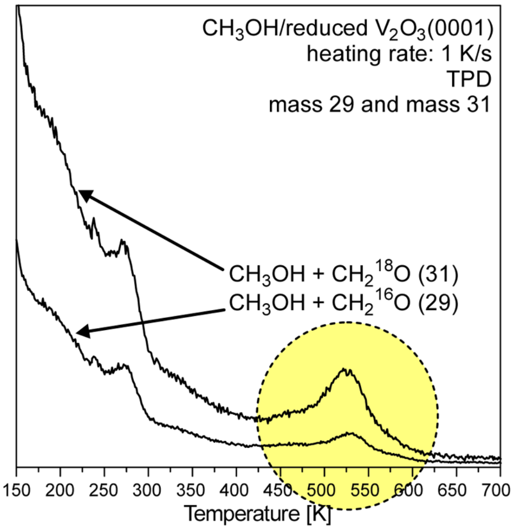

Figure 47. Thermal desorption spectra (mass 29 and 31) of methanol on a weakly reduced oxide layer (electron dose: 8 mC) containing a mixture of ^{16}O and ^{18}O. Reprinted with permission from ref 98a. Copyright 2011 Springer.

Figure 46 shows that also a considerable amount of methane desorbs. This reaction involves cleavage of the methoxy C−O bond and attachment of a surface hydrogen atom (net reaction: $CH_3O + H \rightarrow CH_4 + O$), which means that the abundance of hydrogen atoms is a relevant parameter for the methane yield. A comparison of panels A and B of Figure 46 reveals that the fully reduced surface is more active for methane formation than the weakly reduced one.

One source of hydrogen is the formation of formaldehyde from methoxy, which produces hydrogen atoms ($CH_3O \rightarrow CH_2O + H$). However, especially for the fully reduced surface it appears that there is also some hydrogen from the methoxy formation step, which has not reacted to form water at low temperature. Figure 46B shows that a considerable amount of methanol desorbs up to temperatures of ∼550 K, probably attributable to a reaction between methoxy and hydrogen, demonstrating that there must be hydrogen present even at 500 K. The water desorption peak at ∼515 K also indicates the presence of hydroxy groups. This is in agreement with results of a study of water on reduced $V_2O_3(0001)$, which show that some of the hydroxyl groups resulting from dissociative water adsorption are stable on a reduced surface up to a temperature of ∼600 K.[98e]

Figure 46B shows decreasing methanol desorption rates starting at ∼490 K while methane and formaldehyde formation sets in. Now the hydrogen is consumed for the formation of methane (such a mechanism was also suggested by Farfan−Arribas for methanol on defective $TiO_2(110)$[114]). Hydrogen desorption was not observed, and the water desorption peak is much smaller than the methane desorption peak, which is a clear sign of hydrogen consumption for the production of methane.

In summary, the abundance of hydroxyl groups at elevated temperature is a relevant control parameter for the selectivity of the oxide surface for formaldehyde formation. A way to decrease the methane yield might be to offer an attractive reaction partner for the surface hydroxyl groups such as, for instance, weakly bound oxygen. If the offered reaction partner reduces the hydrogen coverage effectively, then this may lead to a higher formaldehyde yield. Thus, a vanadium oxide with higher oxygen content like V_2O_5 might offer a higher selectivity toward formaldehyde with the price of a higher risk for further oxidation. The oxygen binding energy also plays a role in another aspect. When methane is formed, then the oxygen atom of the methoxy group remains on the surface. Therefore, methane formation is energetically more favorable when the binding energy of oxygen to the oxide is higher, which is another reason a high oxygen binding energy might steer the reaction toward methane formation.

6. VANADIUM OXIDE: $V_2O_5(001)$

$V_2O_5(001)$ layers have been prepared on Au(111) only.[6] Some efforts have also been undertaken to study $V_2O_5(001)$ single crystals.[115] The preparation of $V_2O_5(001)$ on Au(111) essentially consists of the deposition of metallic vanadium onto Au(111) followed by oxidation at 670 K in an ambient atmosphere of 50 mbar of O_2.[6] It was found to be preferable to grow the layers in three cycles of deposition of ∼5 Å of vanadium followed by oxidation to create films that cover the whole surface. A STM image of $V_2O_5(001)$ on Au(111) is shown in Figure 48, and a structural model of the V_2O_5 crystal structure is presented in Figure 49. The double rows visible in the STM image correspond to the vanadyl double rows of the (001) surface (see Figure 49). Because V_2O_5 consists of rather weakly interacting layers stacked along [001], it may be assumed that the structure of the surface layer is not much different from that of the bulk layers, which is also the result of DFT calculations.[116] The oxide layers exhibit a low defect

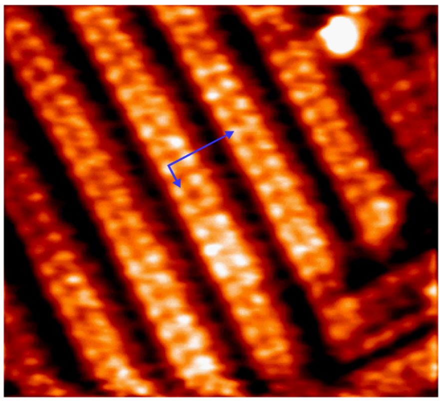

Figure 48. STM image of a $V_2O_5(001)$ layer on Au(111) prepared by oxidation of ∼10 Å of vanadium. Area: 64 × 58 Å^2. Tunneling conditions: V = 2 V, I = 0.2 nA. Adapted with permission from ref 6. Copyright 2008 American Chemical Society.

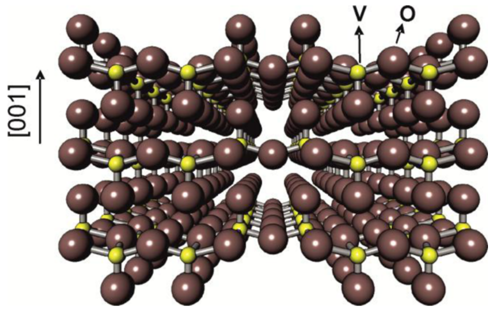

Figure 49. Structural model of the V_2O_5 crystal structure.

density and consist of (001) oriented crystallites with random azimuthal orientation (see Figure 50). These crystallites eventually coalesce to form a closed layer when the film thickness is increased. The layer thicknesses were typically in the range of 50 Å.

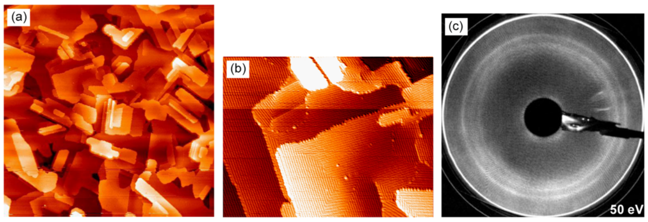

Figure 50. STM images of $V_2O_5(001)/Au(111)$. (a) 300 nm × 300 nm, 3.5 V, 0.2 nA, (b) 100 nm × 75.8 nm, 3 V, 0.2 nA (differentiated), and LEED pattern (c) obtained for a film formed by three successive depositions of 5 Å of vanadium and oxidation cycles. Adapted with permission from ref 6. Copyright 2008 American Chemical Society.

$V_2O_5(001)$ exhibits a lower oxygen defect formation energy than $V_2O_3(0001)$[117] so that one may expect that the path toward methane formation in the methanol partial oxidation reaction is suppressed in this case. The situation for a nonreduced surface is identical to the case of $V_2O_3(0001)$, in that such a surface is inactive with respect to partial oxidation of methanol.

Figure 51 compares TPD spectra (mass 29) obtained after dosing 5 L of CH_3OH at 100 K onto surfaces reduced with varying electron doses. The nonreduced surface seems to be inactive, which is in line with results for nonreduced multilayers of vanadium oxide on $TiO_2(110)$,[118] and similar to what was observed for nonreduced $V_2O_3(0001)$. On the other hand, the reduced surfaces are active for formaldehyde production. Masses characteristic for methanol, water, carbon dioxide, hydrogen, and methane were recorded, but only water, methanol, and formaldehyde could be detected. The formaldehyde desorption peak is at ∼510 K for low degrees of reduction, while intensity at lower temperature increases for electron doses of 3 mC and more. The temperature range for formaldehyde desorption from weakly reduced $V_2O_5(001)$ is similar to that observed for $V_2O_3(0001)$ and supported vanadium oxide layers and clusters,[118,119] which may be indicative of a common mechanism for hydrogen abstraction.

A STM image of $V_2O_5(001)$ reduced with an electron dose of 3 mC is displayed in Figure 52a. The dark depressions are missing vanadyl oxygen atoms as discussed by Guimond et al.[6] Figure 52b was obtained after methanol dosage. There are some bright structures, which are assigned to methoxy groups, and obviously not all defects are occupied. A flash to 560 K removes the methoxy groups, and image (c) is observed.

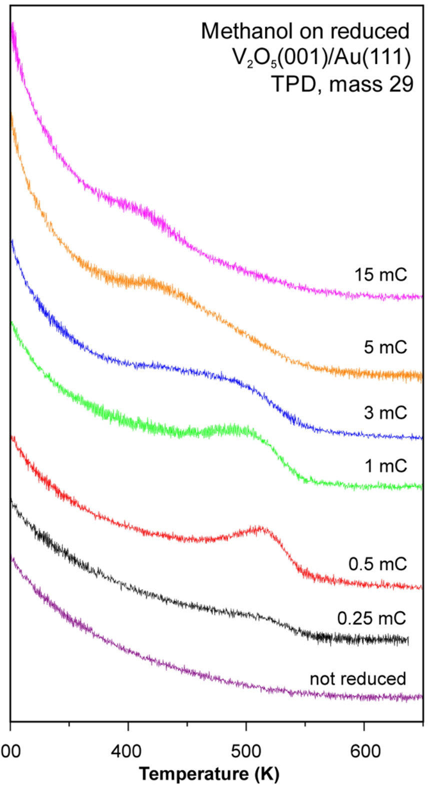

Figure 51. TPD spectra (mass 29, indicating formaldehyde) of 5 L of methanol adsorbed at 100 K on V_2O_5 reduced with various electron doses. The electron doses employed for reduction are indicated in mC. Adapted with permission from ref 98b. Copyright 2009 Royal Society of Chemistry.

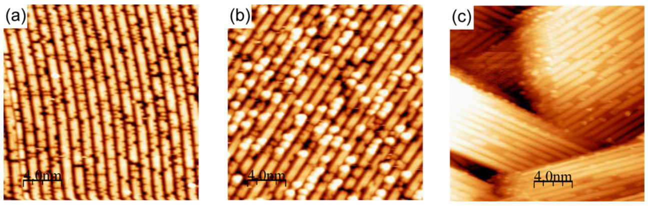

Figure 52. STM images of a $V_2O_5(001)$ film, (a) after reduction with 3 mC of electrons, (b) after subsequent exposure to 10 L of CH_3OH at room temperature, and (c) after flashing to 560 K. The imaged area is 20 × 20 nm^2 in all cases. Tunneling current: 0.2 nA. Bias voltage: 2.0 V (a) or 2.5 V (b,c). Adapted with permission from ref 98b. Copyright 2009 Royal Society of Chemistry.

The maximum amount of formaldehyde formed on $V_2O_5(001)$ films is smaller by about an order of magnitude than the amount formed on $V_2O_3(0001)$ films.[98a] It is not yet understood why this is the case, but one may speculate that extended defects, which are formed at higher degrees of reduction, are not active for formaldehyde production. An ingredient in this discussion may be found in the observation that for $V_2O_5(001)$ single crystals[120] and thin films,[6] severe reduction leads to structures resembling the structure of $V_6O_{13}(001)$. The chemical activity of this surface has not been studied yet.

A reaction that can explain the partial coverage of the reactive oxygen vacancies as seen in Figure 52B is the low-temperature recombination of hydroxyl groups with methoxy to form desorbing methanol. As a consequence, the defects occupied by methoxy at low temperature will be unoccupied at room temperature as observed with STM. Figure 53 shows a methanol desorption peak in the temperature range from 230 to 300 K, possibly resulting from this reaction.

The XPS data in Figure 54 indicate that this peak, indeed, can be attributed to a recombination reaction. The figure displays C1s spectra of methanol after annealing at different temperatures. At the bottom, two spectra of surfaces without methanol adsorbate are shown. The C1s peak at 283.8 eV in these spectra is assigned to a carbon contamination.

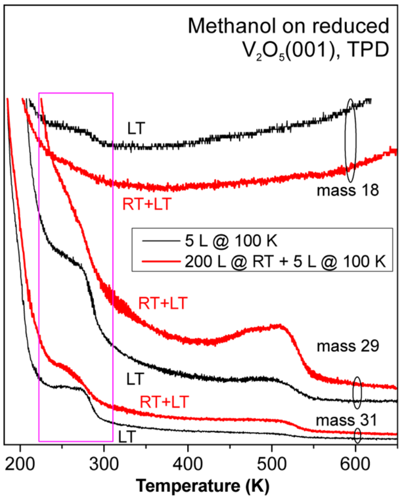

Figure 53. TPD spectra of methanol on $V_2O_5(001)$ reduced with an electron dose of 1 mC; black lines (label "LT") correspond to 5 L of methanol dosed at 100 K, and red lines (label "RT+LT") correspond to 200 L of methanol dosed at RT plus 5 L at 100 K. Reproduced with permission from ref 98b. Copyright 2009 Royal Society of Chemistry.

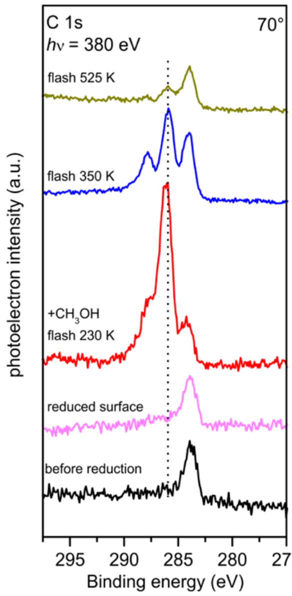

Figure 54. XPS C1s spectra of CH_3OH on $V_2O_5(001)/Au(111)$ measured at 100 K using synchrotron radiation with a photon energy of 380 eV. From bottom to top, the curves represent the situation before reduction, after reduction, and after subsequent methanol exposure at 100 K and flashing to 230, 350, and 525 K, respectively. The dotted line indicates the binding energy of methoxy: 286.2 eV. Reprinted with permission from ref 98b. Copyright 2009 Royal Society of Chemistry.

After methanol adsorption at 100 K, the sample was flashed to 230 K to desorb molecularly adsorbed methanol. The large C 1s peak at 286.2 eV in the corresponding C1s spectrum is attributed to methoxy, while the smaller peak at 288.0 eV is due to molecular methanol probably resulting from the adsorption of methanol from the residual gas atmosphere. The binding energies are similar to those found in the literature.[113,121]

Flashing to 350 K removes part of the methoxy from the surface, while it is more or less gone after flashing to 525 K. The latter is due to formaldehyde production, and the reduction of the C1s intensity after flashing at 350 K is attributed to hydroxyl+methoxy recombination followed by methanol desorption, which leads to the methanol desorption peak between 230 and 300 K in Figure 53. With this interpretation, the experimental results are consistently explained, but it does not explain why only part and not all of the methoxy groups recombine with hydroxyl groups to form methanol.

When dosing of methanol is performed at room temperature (RT), nearly complete coverage of the surface can be achieved by dosing large amounts of methanol. The dependence of the formaldehyde yield (as a measure for the methoxy coverage at high temperature) on the dosing time is shown in Figure 55 (■) for a fixed dosing rate of 0.38 L/s. According to STM, a methanol dose of 200 L at room temperature leads to the occupation of essentially all defect sites, which is not the case for a total dose of 10 L.

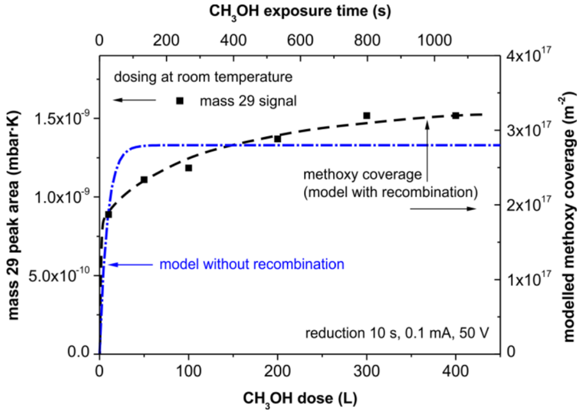

Figure 55. TPD formaldehyde peak area versus methanol dose at room temperature (solid squares) for CH_3OH on $V_2O_5(001)/Au(111)$. The surface was reduced with an electron dose of 1 mC. The dot−dashed (blue) line indicates the best fit to the RT data assuming a sticking coefficient that is proportional to the number of free adsorption sites and ignoring methanol−hydroxyl recombination. The dashed curve indicates the calculated methoxy coverage using a model that includes simultaneous recombination of methoxy and OH toward methanol and combination of OH to form water (see text). Adapted with permission from ref 98b. Copyright 2009 Royal Society of Chemistry.

A simple model where the methanol sticking rate is proportional to the number of unoccupied sites does not satisfactorily explain those experimental results. The best fit to the experimental data is the dot−dashed (blue) line in Figure 55, which significantly deviates from the data points, indicating a more complex reaction scheme. The first step of the scheme is certainly the scission of the methanol OH bonds on surface defects, which produces methoxy and hydroxyl groups:

$$V + VO + CH_3OH \rightarrow CH_3OV + VOH \qquad (8)$$

V, VO, VOH, and CH_3OH are a defect site, a vanadyl group, a hydroxyl group, and a methoxy group, respectively. As was already discussed, one follow-up reaction is the recombination of methoxy and hydroxyl to molecular methanol, which leaves uncovered defects after desorption. This is in line with Burcham and Wachs[122] who reported that dissociative chemisorption of methanol on supported V_2O_5 is reversible. However, there must be a reaction that prevents that all hydroxyl and methoxy groups recombine, because some methoxy groups are still on the surface at elevated temperature where they lead to the formation of formaldehyde at above 500 K. This reaction is the combination of two hydroxyl groups to form water. It removes hydroxyl groups out of the system and prevents recombination of the corresponding methoxy groups with hydroxyl to methanol. These methoxy groups are the source for the produced formaldehyde because they have to stay on the surface until they react toward formaldehyde at sufficiently high temperature. Both reactions, water formation as well as methanol recombination, produce unoccupied adsorption sites:

$$\mathrm{VOH} + \mathrm{VOH} \rightarrow \mathrm{VO} + \mathrm{V} + \mathrm{H_2O} \quad \text{(water formation)} \tag{9}$$

$$\mathrm{VOH} + \mathrm{CH_3OV} \rightarrow \mathrm{VO} + \mathrm{V} + \mathrm{CH_3OH} \quad \text{(methanol formation)} \tag{10}$$

The methoxy groups could clearly be observed with STM (see Figure 52B) and XPS (see Figure 54), and methanol desorption was detected via TPD (see Figure 53). However, there is no clear experimental evidence for the presence of hydroxyls. Room-temperature STM did not show features attributable to hydroxyl groups, which may simply mean that they react below room temperature. On the other, the height of hydroxyl groups in STM images is usually in the range of just 0.2 Å, which might make it hard to identify them in the neighborhood of methoxy groups characterized by a height of ~1.5 Å in STM images. Possibly due to the low coverage, XPS could not identify them .

Figure 55 shows that the formaldehyde yield increases slowly with increasing methanol dosing time. This is a consequence of the permanent removal of hydroxyl groups by water formation during dosing until finally all adsorption sites are covered with methoxy groups, which cannot desorb due to the lack of hydroxyl groups.

The two coupled surface reactions may be modeled by two coupled differential equations:

$$N_{\mathrm{tot}}\frac{\mathrm{d}\theta_{\mathrm{M}}}{\mathrm{d}t} = S(\theta)\cdot\Phi_{\mathrm{M}} - N_{\mathrm{tot}}\theta_{\mathrm{M}}\theta_{\mathrm{OH}}\nu\,\exp\left(-\frac{E_1}{kT}\right) \tag{11}$$

$$N_{\mathrm{tot}}\frac{\mathrm{d}\theta_{\mathrm{OH}}}{\mathrm{d}t} = S(\theta)\cdot\Phi_{\mathrm{M}} - 2N_{\mathrm{tot}}\theta_{\mathrm{OH}}^2\nu\,\exp\left(-\frac{E_2}{kT}\right) - N_{\mathrm{tot}}\theta_{\mathrm{M}}\theta_{\mathrm{OH}}\nu\,\exp\left(-\frac{E_1}{kT}\right) \tag{12}$$

θ_{M} and θ_{OH} are the methoxy and the hydroxyl coverage, E_1 and E_2 are the energy barriers for methoxy−OH recombination and OH combination, t is the time, k is Boltzmann's constant, and T is the adsorption temperature (RT = 298 K). ν, the attempt frequency, was set to 10^{13} s^{-1}, and N_{tot}, the number of vanadyl lattice sites, is 4.8×10^{18} m^{-2}. Φ_{M}, the flux of methanol molecules per unit area and time, was set to 1.35×10^{18} molecules m^{-2} s^{-1}, which corresponds to 0.38 L/s as chosen for the experiment.

The coverage-dependent sticking coefficient $S(\theta)$ was set to:

$$S(\theta) = \frac{N_0 - N_{\mathrm{M}}}{N_{\mathrm{tot}}} \tag{13}$$

N_0 is the number of available adsorption sites per unit area, and N_{M} is the number of methoxy groups per unit area ($N_{\mathrm{M}} = \theta_{\mathrm{M}}N_{\mathrm{tot}}$). In eq 13, the sticking coefficient is proportional to the number of free adsorption sites: if a molecule hits a free defect site then it will adsorb, otherwise it will not adsorb. Under the chosen experimental conditions, the rate of methanol and water formation is smaller by 3 orders of magnitude than the rate at which methanol molecules hit the surface. Therefore, the adsorption sites will always be nearly completely covered, and the choice of the sticking coefficient is not a critical issue.

Surface diffusion is not considered in this model. It is likely that surface diffusion plays a role because the defect density is moderate. However, if the diffusion process is much faster than the water and methanol formation reactions, then it can be neglected. The effect of adsorption on multiple defects was also neglected because STM shows that 90% of the methoxy groups were bound to single defects. In view of the limited density of experimental data, it would not have been possible to fit parameters related to adsorption on multiple defect properly.

The set of differential eqs 11 and 12 was solved numerically. N_0 was set to 7.5% of N_{tot} in agreement with STM data. The calculations were performed in two steps. In the first step, the surface was exposed to a constant flux of methanol for a defined time. In the second step, the methanol flux was set to zero, and the calculation was stopped when the hydroxyl coverage θ_{OH} approached zero due to water formation. A number of calculations for different dosing times and different energy barriers E_1 and E_2 were performed to fit the calculated data to the experimental ones. The best-fit curve, which was calculated for $E_1 = E_2 = 0.85$ eV, is shown as a dashed line in Figure 55. The agreement between the experimental data and the calculated numbers is very good.

Values for the energy barriers can also be estimated from TPD spectra. A simple method is the use of the Redhead equation,[30] which correlates the temperatures of desorption peak maxima with activation energies. This method is usable for simple desorption cases but not for the present situation of two coupled reactions. Therefore, a set of two coupled differential equations has been set up for the description of the dependence of the methoxy and hydroxyl surface coverages on the temperature T for a constant heating rate β:

$$\frac{\mathrm{d}\theta_{\mathrm{M}}}{\mathrm{d}t} = \frac{\nu}{\beta}\theta_{\mathrm{M}}\theta_{\mathrm{OH}}\,\exp\left(-\frac{E_1}{kT}\right) \tag{14}$$

$$\frac{\mathrm{d}\theta_{\mathrm{OH}}}{\mathrm{d}t} = -2\frac{\nu}{\beta}\theta_{\mathrm{OH}}^2\,\exp\left(-\frac{E_2}{kT}\right) - \frac{\nu}{\beta}\theta_{\mathrm{M}}\theta_{\mathrm{OH}}\nu\,\exp\left(-\frac{E_1}{kT}\right) \tag{15}$$

The TPD signals of methanol and water (I_{M} and I_{W}) are proportional to the methoxy−OH recombination and the OH combination rates:

$$I_{\mathrm{M}} \propto \frac{\nu}{\beta}\theta_{\mathrm{M}}\theta_{\mathrm{OH}}\,\exp\left(-\frac{E_1}{kT}\right) \tag{16}$$

$$I_{\mathrm{W}} \propto \frac{\nu}{\beta}\theta_{\mathrm{OH}}^2\,\exp\left(-\frac{E_2}{kT}\right) \tag{17}$$

The set of eqs 14 and 15 was solved numerically, assuming that at the starting temperature for the calculation, 100 K, all sites are covered, that is, $\theta_{\mathrm{M}}(100\text{ K}) = \theta_{\mathrm{OH}}(100\text{ K}) = 0.075$. A good agreement with the experimentally observed methanol desorption temperature (~275 K according to Figure 53) is obtained for $E_1 = E_2 = 0.75$ eV. These values are lower by 0.1 eV than those obtained via modeling the methoxy coverage as a function of dosing time at room temperature (see Figure 55).

In view of the simplifications used in the models, we feel that this is a reasonable agreement.

Figure 56 visualizes the temperature dependence of the computed methanol and water desorption rates (panel b), and the calculated methoxy and hydroxyl coverages (panel a). The methoxy coverage after complete OH loss is about 50% of the initial methoxy coverage. This is in reasonable agreement with the XPS data presented in Figure 54, which show that the methoxy coverage at 350 K is about one-half as high as the coverage at 230 K. Figure 56b also reveals similar desorption temperatures of water and methanol. This fits quite well to the observed intensity in the water desorption spectra (mass 18) in Figure 53 between 250 and 300 K. Part of the intensity may also result from the methanol desorption occurring at about the same temperature: exchange reactions at the walls of the mass spectrometer housing and the mass spectrometer itself lead to water formation when methanol desorbs.

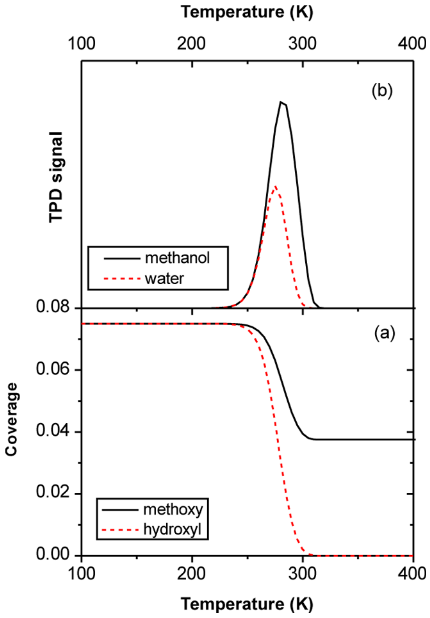

Figure 56. (a) Calculated methoxy coverage (solid line) and OH coverage (dashed line) versus temperature for a model that includes the recombination of methoxy and OH and the simultaneous combination of OH groups. The corresponding calculated TPD signals for methanol (solid line) and water (dashed line) are plotted in (b). Reprinted with permission from ref 98b. Copyright 2009 Royal Society of Chemistry.

DFT calculations using a 3 × 1 surface unit cell support the experimental observation of a defect-free regular $V_2O_5(001)$ interacting only weakly with methanol. The calculated adsorption energy is only 0.16 eV.[98b] The formation of a single vanadyl oxygen vacancy on a 3 × 1 surface requires an energy of 1.84 eV in agreement with literature results.[116,123] This energy is rather small because the reduced vanadium ion forms a bond to the vanadyl oxygen below (belonging to the second layer), and the oxidation states of the two vanadium ions involved in the resulting V−O−V sequence are +4/+4 instead of +3/+5 because this lowers the energy of the reduced state. The adsorption energy of molecular methanol is rather small: for methanol bound in the geometry shown in Figure 57A, an energy of 0.64 eV was obtained. A slightly smaller adsorption energy (0.01 eV less) was found for a geometry where a hydrogen atom of the methanol binds to the vanadyl oxygen at the other side of the double row.

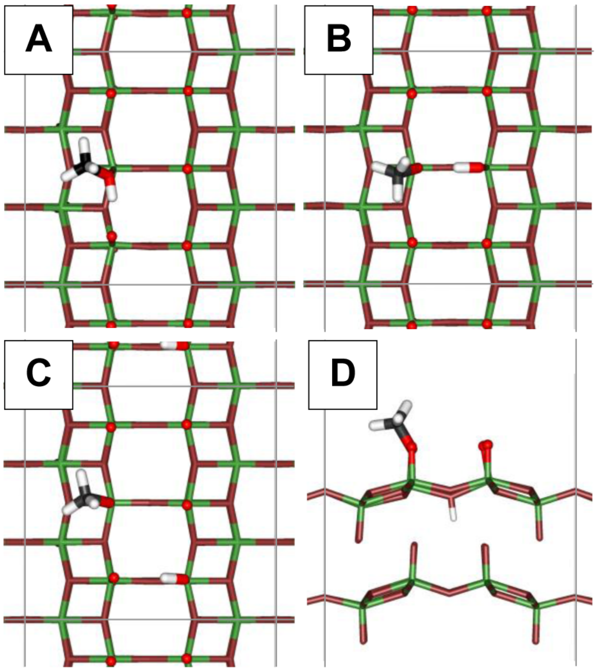

Figure 57. Calculated structures for methanol adsorption on an isolated defect. Reprinted with permission from ref 98b. Copyright 2009 Royal Society of Chemistry.

Figure 57B and C shows structures of dissociated methanol molecules with the hydrogen atoms on different positions on the surface. The adsorption energies are 0.41 and 0.57 eV, respectively. If hydrogen is bound to a vanadyl oxygen atom next to the methoxy group in the same vanadyl row, then the adsorption energy is even smaller (0.34 eV). Dissociation is energetically not favorable in all of these cases because the molecularly adsorbed state has a higher adsorption energy. This is different for the structure shown in Figure 57D where the hydrogen atom is located below the surface. In this case, the adsorption energy is 0.67 eV, which is 0.03 eV higher than the adsorption energy of molecular methanol.

Figure 58A illustrates the most stable adsorption geometry of molecular water with a calculated adsorption energy of 0.64 eV. For dissociative adsorption, the most stable adsorption geometry is shown in Figure 58B. The hydroxyl groups form hydrogen bonds to oxygen atoms at opposite vanadyl rows, which stabilizes the structure. This arrangement has a computed adsorption energy of 0.44 eV, indicating that

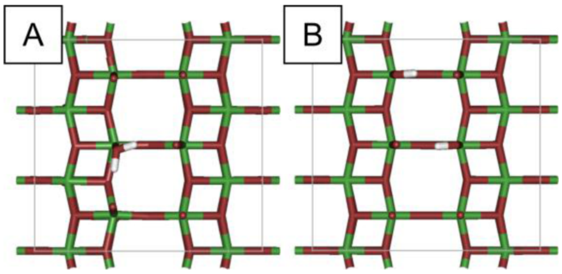

Figure 58. Calculated structures for water adsorption on an isolated defect. Adapted with permission from ref 98b. Copyright 2009 Royal Society of Chemistry.

dissociative adsorption is clearly disfavored, and that hydroxyls on the surface will react to form water as soon as the temperature is high enough to overcome potentially existing reactions barriers.

7. RUTHENIUM OXIDE: $RuO_2(110)$

Ruthenium oxide films have been invoked to explain the unusually high reactivity of Ru catalysts among the Pt group metals in CO oxidation. The original ideas of Peden and Goodman[124] suggesting a dense (1 × 1) phase of chemisorbed oxygen on Ru(0001) as the active phase for CO oxidation have been revisited by Over and co-workers[125] who proposed that, under technologically relevant conditions, the Ru catalyst is represented not by metal but the $RuO_2(110)$ surface. Further studies, performed in several research groups, indicated that the active phase might be a ruthenium oxide thin film, sometimes referred to as "surface oxide".[126]

Most of the studies on the formation of ruthenium oxide films were performed on Ru(0001) single crystals. It is well documented that oxygen chemisorbs on Ru(0001) in several ordered structures, for example, O(2 × 2), O(2 × 1), and 3O(2 × 2).[127] The O(1 × 1) phase can be formed at high oxygen pressures or by exposing to more oxidizing agent like NO_2, both at elevated temperatures (>600 K).[128]

The initial stages of the oxide formation have been addressed both experimentally and theoretically. Böttcher and Niehus[129] provided strong evidence for the formation of subsurface oxygen on Ru(0001) using TPD, LEED, and He^+ ISS. The incorporation of oxygen was performed via dissociative chemisorption of NO_2, O_2, and N_2O. For sample temperatures below 800 K, oxygen penetration into the subsurface region occurred only when oxygen molecules impinged on the saturated O(1 × 1)-layer. Interestingly, a thermally induced transformation of this phase into subsurface oxygen was not found, even at temperatures close to the onset of oxygen desorption (i.e., ~1000 K). In the presence of subsurface oxygen, accompanied by the appearance of new faint diffraction spots in LEED, later assigned to $RuO_2(110)$, a new O_2 desorption peak developed at ~400−450 K.

DFT calculations by Reuter et al.[130] suggested that oxygen first occupies the surface hcp sites in amounts up to 1 ML, and only then does the additional oxygen go subsurface, where it preferentially forms islands with the hexagonal O−Ru−O trilayer structure (see Figure 59a,b). The total energy is further minimized by a small lateral displacement (stretch) of the O−Ru−O layer that is relatively weakly coupled to the underlying metal. From a thermodynamic point of view, such a process could, in principle, be continued until a critical film thickness was approached, where the transformation toward the more thermodynamically stable $RuO_2(110)$ structure occurs.

Certainly, the transition from oxygen adsorption to oxide formation on Ru(0001) is very complex and involves the coexistence of various phases as directly shown with LEEM.[131] Although the observed quasi-(2 × 2) micro-LEED pattern was assigned to the formation of an O−Ru−O trilayer, and also Blume et al.[126b] suggested the transient surface oxide to be related to the O−Ru−O structure, this trilayer has not been yet identified. Furthermore, one-dimensional oxidic structures[132] have recently been reported for the surface possessing 1−2 ML of oxygen, which were tentatively assigned to the intermediate state for the formation of the $RuO_2(110)$ phase.

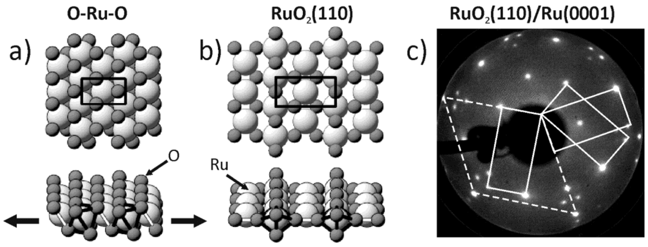

Figure 59. (a,b) Formation of the $RuO_2(110)$ surface via the formation of an O−Ru−O trilayer with oxygen atoms occupying surface and subsurface sites of Ru(0001). Top and perspective views are shown; the rectangular surface unit cells are indicated. The $RuO_2(110)$ surface is achieved by expanding the trilayer in the directions indicated by the arrows. (Adapted with permission from ref 130. Copyright 2002 Elsevier). (c) Typical LEED pattern (60 eV) of the thin ruthenium oxide film on Ru(0001). The unit cells of Ru(0001) (dashed line) and three rotational domains of $RuO_2(110)$ (solid lines) are indicated.

The atomic geometry of the "oxygen-rich" Ru(0001) surfaces was studied by LEED I/V in combination with DFT calculations.[133] The surface, prepared by exposure to ~10^6 L of O_2 at 600 K, was not uniform: It consisted of areas covered by a O(1 × 1) overlayer together with thin (10−20 Å) patches of $RuO_2(110)$. Both structures extend over several tens of micrometers across the surface as imaged by STM.[125a] The $RuO_2(110)$ domains are aligned with its $[\bar{1}10]$ axis along the three $[10\bar{1}0]$ high-symmetry directions of the Ru(0001) substrate. From the LEED pattern (see Figure 59c), the dimensions of the real space unit cell are estimated to be 6.4 Å × 3.1 Å, which agrees well with the unit cell of a $RuO_2(110)$-(1 × 1) surface, that is, 6.38 Å × 3.11 Å. The $RuO_2(110)$ domains grow incommensurately to the underlying Ru(0001) substrate. Because the $RuO_2(110)$ oxide film with its rectangular unit cell exhibits no 3-fold symmetry as does Ru(0001), three rotational domains coexist on the Ru(10001) surface.

It is believed that the $RuO_2(110)$ film grows at temperatures above 550 K via a nucleation and growth mechanism, which could also be considered as an autocatalytic oxidation process of ruthenium.[134] Interestingly, SXRD experiments[135] showed that the grown $RuO_2(110)$ films on Ru(0001) were almost of the same average thickness (~1.6 nm) in a wide range of temperatures (550−650 K) and pressures (10^{-4}−10 mbar) studied, thus indicating a self-limited growth of the oxide film. From the *l*-scans in SXRD patterns, which probe the structure normal to the surface, the $RuO_2(110)$ film surface is very flat,[133] as was confirmed by STM.[125a,136] The atomic structure of the interface between metallic and oxide phases is yet unknown.

There were few attempts to grow RuO_2 films exposing other surface planes. On the basis of the LEED I/V results, corroborated by DFT calculations, Kim et al.[137] showed that the $RuO_2(100)$ film can be grown on a Ru($10\bar{1}0$) single-crystal surface. The lattice constant of $RuO_2(100)$ is 4.5% compressed along the [010] direction, which is aligned with the [0001] direction of Ru($10\bar{1}0$), but fully relaxed in the [001] direction. The $RuO_2(100)$ surface is terminated by bridging O atoms, with Ru−O bond lengths being in the range of 1.90−2.05 Å, typical for bulk RuO_2. Some structural deviation from the bulk-truncated $RuO_2(100)$ surface was explained by the unidirectional compression of the epitaxial $RuO_2(100)$ film.

Reuter and Scheffler[138] addressed composition, structure, and stability of $RuO_2(110)$ as a function of oxygen pressure. The "stoichiometric" termination (i.e., terminated with O atoms in the bridging positions; see Figure 60a) is the most stable only at low oxygen chemical potentials, that is, low

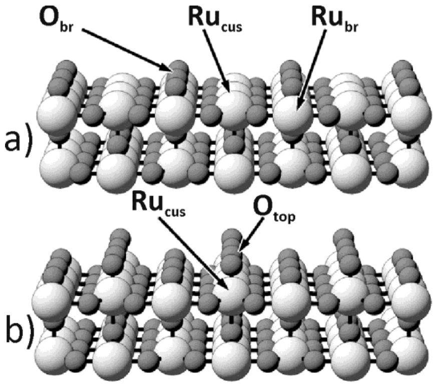

Figure 60. The most stable terminations of $RuO_2(110)$ predicted by DFT. (a) Stoichiometric $RuO_2(110)$-O_{br} termination is the most stable at low oxygen chemical potentials (i.e., low pressures and high temperatures). (b) $RuO_2(110)$-O_{top} termination, where O atoms sit atop the formerly under-coordinated Ru_{cus} atoms, is the most stable at high oxygen chemical potentials. Adapted with permission from ref 138. Copyright 2001 American Physical Society.

pressures and/or high temperatures. At technically relevant oxygen pressure the surface is predicted to contain additional terminal O atoms (Figure 60b). These O species were identified by HREELS via a vibrational band at 103 meV characteristic for double bond metal−oxygen species (Figure 61).[139] Also, TPD studies revealed that exposing of the stoichiometric $RuO_2(110)$ surface to O_2 leads to the formation of two additional surface species: a molecularly chemisorbed state O(γ) bridging two neighboring coordinatively unsaturated Ru atoms (Ru_{cus}) and weakly bound O(δ) atoms in a terminal position above the Ru_{cus} atoms. It has been proposed that the reactivity of the $RuO_2(110)$ surface is determined by the Ru_{cus} atoms, which accommodate atop O and CO species.[125c,140] The interplay between the different oxygen species apparently accounts for the high sticking coefficient for dissociative adsorption as well as for the continuous restoration of the surface structure in the course of catalytic oxidation reactions.

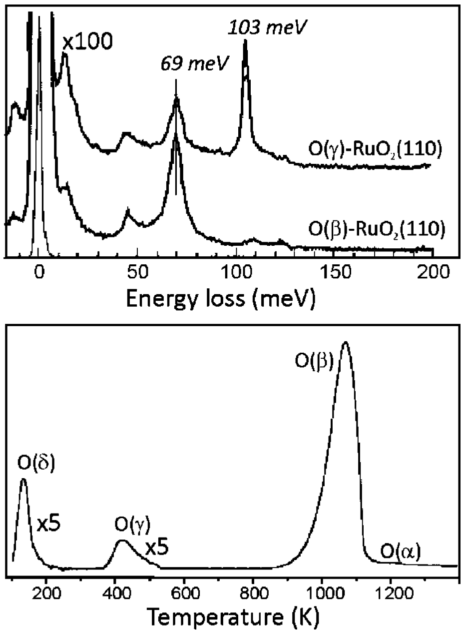

Figure 61. (Top panel) HREEL spectra of the $RuO_2(110)$ surface exposing only O(β) and both O(β) and O(γ) species (O_{br} and O_{top} species in Figure 60, respectively). (Bottom) TPD spectrum of oxygen (32 amu) desorbed from a ruthenium oxide film grown on Ru(0001). The desorption states O(α), O(β), O(γ), and O(δ) correspond to chemisorbed oxygen on Ru(0001), lattice oxygen of $RuO_2(110)$, atop oxygen on $RuO_2(110)$, and molecular oxygen on $RuO_2(110)$, respectively. Adapted with permission from ref 139. Copyright 2001 American Chemical Society.

Not surprisingly, the reactivity studies of the RuO_2 films were performed primarily with respect to CO oxidation. (For other reactions, the reader is referred to the very recent comprehensive review of Over).[134] As was already mentioned above, several oxygen-containing surface structures on Ru have been suggested as the most active in CO oxidation: O(1 × 1)-Ru(0001),[124] a crystalline $RuO_2(110)$ film,[125a−c] and ill-defined surface oxides.[126a,b] There are still ongoing debates on the most active phase in this reaction.[141] Nonetheless, a general consensus is that the binding energy of oxygen species involved in the reaction has to be sufficiently small to render the system catalytically active. It is fair to say that the experimental results critically depend on the surface preparation and reaction conditions (pressure, temperature, CO/O_2 ratio). Mass transport effects bring additional complexity into such studies and become more critical at atmospheric pressures.[142] Therefore, direct comparison of the results obtained in different research groups is often difficult, if not impossible. Note also that one has to discriminate the structure and reactivity of oxide films formed under the reaction conditions and those prepared prior to the reaction.

The complex structure−activity correlation in the CO oxidation on ruthenium has nicely been illustrated by Over et al.[143] using a high pressure cell of a SXRD setup as a small batch reactor connected to a mass spectrometer for the gas composition analysis. At total pressures of reactants in the 100 mbar range, the catalytic system revealed two distinct active phases depending on the reaction conditions: a nonoxidized phase and $RuO_2(110)$. Both phases were stable over a wide pressure and temperature range. Below a reaction temperature of 520 K, the experimental TOF numbers were almost identical for the both phases. Above 520 K, $RuO_2(110)$ was much more active than the nonoxide phase. The activity of the catalyst increased substantially, whenever the catalyst underwent structural changes either by reducing $RuO_2(110)$ or by forming $RuO_2(110)$.

Gao et al.[144] performed similar studies at near-atmospheric pressures using the entire UHV chamber as the reactor, and the activity was measured from the total pressure changes. In addition, CO surface species were monitored in situ with PM-IRAS. At relatively high temperatures (>550 K) and net oxidizing reaction conditions, $RuO_2(110)$ was formed that exhibited CO oxidation reactivity several times higher than O(1 × 1)-Ru(0001) on a per surface area basis. Under stoichiometric and reducing reaction conditions, RuO_2 seemingly converted to a surface oxide and then to a chemisorbed oxygen phase between 400 and 600 K. Under net oxidizing reaction conditions, RuO_2 was stable and displayed very high reactivity at temperatures as low as 450 K. The authors stressed, however, that this high reactivity regime for RuO_2 is restricted (1) to very oxidizing reaction conditions, (2) to very low reaction temperatures, and (3) to short reaction times. Interestingly, the authors observed a regime with a “negative” activation energy. To explain the rate decreasing with the temperature in the range 400−475 K in the mixture of 8 Torr CO and 40 Torr O_2, the authors invoked the formation of a carbonate, which deactivates the active sites at low temperatures, but dissociates upon approaching 500 K (see also ref 136).

Recently, CO oxidation at near-atmospheric pressures and low temperatures (400−470 K) has been studied over ruthenium oxide films grown on Ru(0001).[132] In particular, the relation between the reactivity and the film thickness was the focus of this study. The surfaces were prepared under vacuum conditions prior to the reactivity measurements carried out in a small circulating flow reactor using gas chromatography. The thickness of the films was varied by the oxygen pressure and oxidation temperature and monitored by AES. The reactivity of the nonoxidic Ru surfaces with solely chemisorbed oxygen ad-layers was also examined, for comparison.

Figure 62 shows the reactivity (TOF) of the films under net oxidizing conditions (10 mbar CO and 50 mbar O_2, He balance to 1 bar) as a function of the nominal film thickness. A steep increase in the reactivity upon oxygen incorporation into the Ru(0001) surface (i.e., the oxygen content exceeds 1 ML) is clearly seen. Basically, at these reaction conditions, CO oxidation sets in only in the presence of the oxide phase. Increasing the film thickness further enhances the reactivity, although to the lower extent. (Note that the film thickness almost did not change during the reaction as judged by AES.) Therefore, the results suggest that the presence of a very thin oxide layer is, in principle, sufficient to show superior catalytic activity.

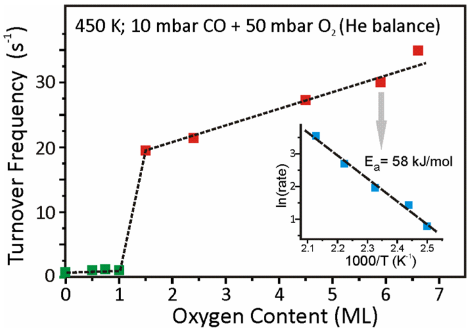

Figure 62. CO_2 formation rate (TOF) as a function of oxygen content in the RuO_x films measured prior to the reactivity measurements (red symbols).[132] The results for ordered chemisorbed layers are shown, for comparison (green symbols). The reaction was performed in the circulating mixture of 10 mbar CO and 50 mbar O_2 (He balance) at 450 K. The Arrhenius plot for the reaction rate on ~5 ML oxide films is shown in the inset.

Upon exposure to 10 mbar O_2 at 450 K, all films studied showed the O(γ) desorption signal at ~420 K, previously assigned to terminal oxygen adsorbed on top of Ru_{cus} atoms, and the most intense O(β) peak centered at ~1010 K resulting from the lattice oxygen in RuO_2(110) (see Figure 61). Meanwhile, all oxygen ad-layers on Ru(0001) showed only strongly bound O(α) states with desorption temperatures above 1000 K. The intensity of both O(γ) and O(β) peaks scaled with the nominal film thickness. Therefore, increase of the reaction rate observed between 1 and 7 ML, as shown in Figure 62, may be explained by the increased number of the surface active sites associated with weakly bound O(γ) oxygen species.

The Arrhenius plot, measured for the 5 ML films in the reaction mixture of 10 mbar CO and 50 mbar O_2 in the temperature range of 400−470 K (inset in Figure 62), yields the activation energy of 58 ± 4 kJ/mol. This value is considerably lower than 78 ± 10 kJ/mol reported by Over et al.[143] for the RuO_2(110) films at the nearly stoichiometric CO/O_2 ratios (i.e., 14 mbar CO + 5.5 mbar O_2) at 470−670 K. The first-order reaction for CO and practically zero order for O_2, observed in experiments at 450 K, again, deviate from the results of Over et al.,[143] where zero orders for both CO and O_2 were reported. These authors noted, however, that the reaction orders were determined only qualitatively, for example, by varying partial pressures of both gases simultaneously. Nonetheless, the comparison clearly manifests the complexity and diversity of the reaction pathways occurring on ruthenium oxide films even in this rather simple reaction.

Another interesting aspect, which remains unexplored on this system, is the role of the film surface ordering on reactivity. To address this issue, reactivities of the well-ordered films and disordered films, which were prepared by mild Ar^+-sputtering and reoxidation in 10^{-4} mbar O_2 at 450 K, that is, much below the temperature used for the preparation of ordered films (~700 K), were compared. The treatment resulted in the disappearance of the diffraction spots of the RuO_2(110) phase, although no considerable changes in the surface stoichiometry were observed by AES. It has turned out that the disordered films showed a higher reaction rate than did the ordered films. In principle, this finding agrees well with the previous high pressure (0.1 mbar, CO/O_2 = 1) XPS studies[126b] showing no direct correlation between the high CO_2 production rate and the formation of the stoichiometric RuO_2 phase as judged by XPS.

It therefore appears that surface ordering and thickness of ruthenium oxide films on Ru(0001) are, in fact, not critical for their superior catalytic activity in CO oxidation, at least at low temperatures. The decisive parameter is most likely the presence of weakly bound oxygen species on the RuO_2(110) films.

8. IRON OXIDES: Fe_3O_4(111) AND Fe_2O_3(0001)

Iron oxides are one of the most widespread materials on our planet, for example, as iron ores, rust, etc. A number of iron oxide phases with different stoichiometries and structures exist as naturally grown crystals, for example, FeO (wüstite), Fe_3O_4 (magnetite), α-Fe_2O_3 (hematite), and γ-Fe_2O_3 (maghemite).[145]

FeO crystallizes in the cubic sodium chloride structure, where the O^{2-} anions form a close-packed fcc sublattice with Fe^{2+} cations located in the octahedral interstitials. Under thermal equilibrium, this phase is stable only at high temperatures (>843 K), otherwise it disproportionates into metallic (α-Fe) and Fe_3O_4 phases.[145b] Fe_3O_4 (magnetite) crystallizes in the inverse spinel structure, where the O^{2-} anions form a fcc sublattice with the tetrahedral interstitials occupied by Fe^{3+} and octahedral interstitials occupied by equal numbers of Fe^{2+} and Fe^{3+} cations. α-Fe_2O_3 (hematite) crystallizes in the corundum structure, where O^{2-} form a hcp sublattice with Fe^{3+} cations located in octahedral interstitials. γ-Fe_2O_3 (maghemite) is a metastable phase with an inverse spinel crystal structure and can be considered as an Fe^{2+}-deficient magnetite. According to the Fe−O phase diagram,[146] only α-Fe_2O_3 (hematite) is stable at the ambient conditions.

Despite different stoichiometries and crystal structures, these iron oxide phases have a common structure feature, the oxygen

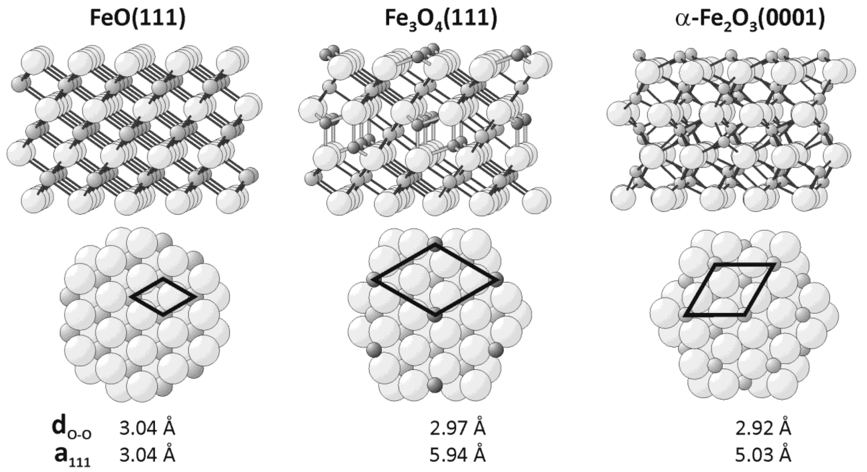

Figure 63. Perspective (top panel) and top (bottom panel) views of the most stable iron oxide phases. The in-plane O−O distance (d_{O-O}) and unit cell size (a_{111}) are indicated for each structure. The surface unit cells are shown for each surface, which can be viewed as (1 × 1), (2 × 2), and ($\sqrt{3} \times \sqrt{3}$)R30° with respect to the oxygen layer in FeO(111), $Fe_3O_4(111)$, and α-$Fe_2O_3(0001)$, respectively.

sublattice that forms a close-packed layer, more clearly visible when projected onto FeO(111), $Fe_3O_4(111)$, and $Fe_2O_3(0001)$ surface planes (Figure 63). The two-dimensional cells in the oxygen layers have dimensions of 3.04 Å for FeO, 2.97 Å for Fe_3O_4, and 2.90 Å for α-Fe_2O_3 (in the latter case, slight lateral distortions away from a perfect hexagonal layer exist). Because of the different iron cation positions between the oxygen planes, the surface unit cells have dimensions of 3.04 Å for FeO(111), 5.94 Å for $Fe_3O_4(111)$, and 5.02 Å for α-$Fe_2O_3(0001)$ corresponding to (1 × 1), (2 × 2), and ($\sqrt{3} \times \sqrt{3}$)R30° superstructure cells when referred to the (1 × 1) cell in the oxygen plane of the respective oxide.

Iron oxide overlayers are naturally formed as passivating films on iron metallic surfaces. Although the experimental results for iron single-crystal surfaces[147] showed the formation of iron oxides with a stoichiometry depending on the preparation conditions, these films were poorly ordered. For example, oxidation of Fe(111) at 500 K resulted in the formation of large islands of Fe_3O_4 interspersed with patches of uncovered substrate.[148] Oxidation of Fe(110) by molecular oxygen results in an FeO(111) film, the quality of which can be improved by using atomic oxygen during additional iron deposition.[149]

Because heteroepitaxial growth offers best control of film stoichiometry, thickness, and morphology, well-ordered iron oxide films were grown on metal substrates, primarily on Pt(111), and to a much lesser extent on other metals, for example, Ru(0001),[150] Ag(111),[151] Ag(100),[152] Au(111),[153] Cu(110).[154] Note also that, due to the relatively good electrical conductivity of the iron oxides (in particular of Fe_3O_4, where the high conductivity is attributed to electron hopping between the Fe^{2+} and Fe^{3+} ions), numerous surface science studies have been performed on single-crystal surfaces, notably by Thornton's and Shvetz's groups, which provided an additional basis for understanding of the atomic structure and properties of iron oxide films. An excellent review on the structure of iron oxide films grown on Pt(111) has been written by Weiss and Ranke[155] based on the results published up to the year 2001. Although we cannot avoid some overlap with this review, we will mainly refer to the most recent results in this field.

The preparation of well-ordered iron oxide films on Pt(111) was first reported by Somorjai and co-workers in 1988.[156] Using LEED, AES, ISS, and TPD, the authors showed the formation of differently ordered structures as a function of the film thickness. First atomic resolution STM images in combination with theoretical image simulations of Galloway et al.[157] and photoelectron diffraction experiments of Kim et al.[158] showed that the thinnest iron oxide film on Pt(111) consists of an O-terminated single layer of FeO(111). (Note that this film does not represent a FeO bulk oxide, which requires at least three Fe−O bilayer repeat units in the (111) orientation.) An O−Fe interlayer distance of 0.68 Å was measured, which is considerably smaller than 1.25 Å in the FeO bulk. (Later, the value 0.62 Å was computed by DFT calculations.[159]) The considerable relaxation in the FeO(111) monolayer was attributed to the strong interaction with a Pt(111) support to compensate polar instability of the (111) plane of oxides sharing the rock-salt crystal structure. Because of the ~10% mismatch between the FeO(111) and Pt(111) lattices, these films exhibit characteristic Moire patterns, clearly observed by LEED and STM (see Figure 64a), which have been ascribed as ($\sqrt{84} \times \sqrt{84}$)R10.9° and ($\sqrt{91} \times \sqrt{91}$)R5.2° coincidence structures.[157a,160] Interestingly, a monolayer FeO(111) film was found to grow also on a Pt(100) substrate.[161] Several coincidence structures were identified by high-resolution STM and LEED I/V analysis such as FeO(111)/Pt(100)-c(2 × 10) and -(2 × 9).[161a]

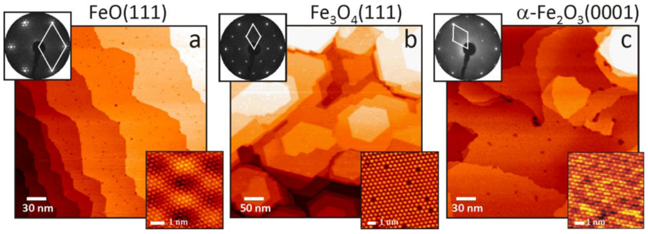

Figure 64. Large-scale and high-resolution STM images of iron oxide films grown on Pt(111). The upper insets show LEED patterns (60 eV) with the unit cells indicated (see structure models in Figure 63).

Multilayer iron oxide films, grown on Pt(111) using cycles of iron deposition and oxidation at typical oxygen pressures of 10^{-6} mbar, were identified as $Fe_3O_4(111)$ films (Figure 64b). It was shown by STM that these films grow via a Stranski−Krastanov mode.[162] First, quantitative analysis of film surfaces by LEED was performed by Weiss et al.[163] and later reexamined by Ritter and Weiss.[164] The results suggested that the surface exposes 1/4 ML of iron ions (Fe_{tet1} in Figure 65a) over a slightly distorted hcp oxygen layer. The outermost iron plane is relaxed inward toward the underlying oxygen plane by about 40% of the corresponding bulk spacing, followed by strong relaxations of the next three interlayer spacings. It was suggested that both the minimization of the number of dangling bonds and that of the electrostatic surface energy are the driving forces for these relaxations due to the mixed bond character that lies between a pure ionic and a pure covalent bond.

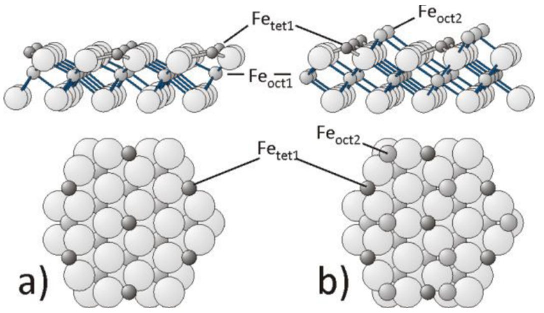

Figure 65. Perspective and top views of the most frequently discussed terminations of $Fe_3O_4(111)$.

STM studies of the $Fe_3O_4(111)$ films[162,165] revealed wide flat terraces of a singly terminated surface showing lattice of protrusions with a 6 Å periodicity (see Figure 64b), in agreement with the surface unit cell 5.94 Å of $Fe_3O_4(111)$. The protrusions were assigned to the topmost Fe_{tet1} atoms, whose Fe 3d states dominated near the Fermi level as shown by DFT calculations.[165] The most abundant defects were imaged as missing protrusions, and thus assigned to iron vacancies in the topmost Fe layer. This finding was additionally confirmed by LEED I/V results where different types of vacancy defects have been simulated.

The proposed surface structure substantially differed from the structure model suggested on the basis of STM results of natural $Fe_3O_4(111)$ single crystals. Depending on the surface preparation, Lennie et al.[166] observed two coexisting surface structures. One surface, dominated upon annealing in oxygen (10^{-7} mbar O_2, 1173 K, 30 min), was assigned to 3/4 ML of Fe_{oct1} atoms and 1/4 ML of O atoms such that a trimer of Fe atoms is capped by an O atom, ultimately resulting in a single protrusion in the lattice with a 6 Å periodicity. (In more recent studies, this group has revisited this structure and no longer favors this model; see below.) The second surface that became more evident upon UHV annealing (1073 K, 20 min) was attributed to unreconstructed (111) termination that exposes the Fe_{oct2}−Fe_{tet1} layers (totally 1/2 ML of iron; see Figure 65b). The authors suggested that differences between this surface model and that of derived from LEED analysis of thin films may arise from differences in substrates or surface preparation techniques. The preferential sputtering effects during the Ar^+ bombardment used for surface cleaning of the iron oxide crystal may also contribute to the discrepancy observed. The conditions used by Lennie et al.[166] for the preparation of single-crystal surfaces are much more reducible than those typically used for the film preparation. Indeed, further STM study of a heavily reduced $Fe_3O_4(111)$ crystal surface[167] showed a so-called "biphase ordering", the phenomenon that was first observed on the α-$Fe_2O_3(0001)$ crystal surfaces.[168] The surface showed several long-range ordered structures with a periodicity of ~40 and ~60 Å. Atomically resolved STM images led Condon et al.[167] to conclude that the selvedge can exist as a superlattice of coexisting $Fe_3O_4(111)$ and $FeO_{1-x}(111)$ islands. The origin of these superstructures was then revisited by Shvets and coworkers, who assigned those to electron−lattice instability, resulting in giant localized polaron and/or charge density waves, rather than in a mosaic of different iron oxide terminations.[169] In turn, this assignment was questioned by Paul et al.,[170] who reported a variety of other superstructures under reducing conditions, which have been identified in terms of $Fe_{1-x}O$ overlayer on top of bulk (111) magnetite.

Basically, the same long-range ordered structures were observed on the $Fe_3O_4(111)$ films, prepared at low oxidation temperatures (~900 K), albeit as minority species.[165] The presence of a regular surface surrounding the superstructures (see Figure 66) allowed surface structure modeling based on registry analysis of protrusions. In addition, the STM studies revealed that the $Fe_3O_4(111)$ films seem to be quite reactive even toward the residual gases in UHV, whereas the FeO(111) films were totally inert.[165,171] The adventitious ad-species, often observed on the $Fe_3O_4(111)$ films, showed a bias-dependent contrast. Those appeared as protrusions at positive bias and as depressions at negative bias. In the latter case, they can easily be messed up with the vacancy defects always appearing as depressions regardless of the bias magnitude and polarity. STM "movies" revealed a surface diffusion of ad-species via hopping.[171] Tentatively, these have been assigned to water related species (see also ref 172). The results indicate that the structure identification of iron oxides surfaces on the basis of solely STM images may be dubious.

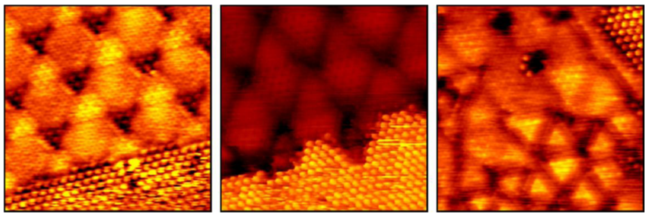

Figure 66. STM images (14 nm × 14 nm) illustrating various superstructures observed on the $Fe_3O_4(111)$ films prepared by oxidation at ~900 K.[165] The "regular" surface, seen in these images as a hexagonal lattice of protrusions with a 6 Å periodicity, dominates the surface.

In attempts to identify surface termination of the $Fe_3O_4(111)$ films, the adsorption of CO as a probe molecule was studied, because CO does not dissociate on oxide surfaces under typical UHV conditions. Combined TPD, IRAS, and HREELS results[173] showed the presence of three adsorption states of CO, which were clearly distinguished by desorption temperature (T_d) and CO stretching frequency (ν), that is, $T_d \approx 110$ K, $\nu = 2140$−2115 cm^{-1}; 180 K, 2080 cm^{-1}; and 230 K, 2207 cm^{-1}. Among the bulk-truncated structure models, the CO adsorption results favored the double Fe layers termination (i.e., 1/4 ML of $Fe^{2+}{}_{oct}$ over 1/4 ML on $Fe^{3+}{}_{tet}$; see Figure 65b) like the one observed by Lennie et al.[166] on a $Fe_3O_4(111)$ single crystal. The proposed model has less excess charge than others. The most strongly bound CO was associated with Fe^{3+} species on the step edges.[174] Unfortunately, these samples lacked STM characterization, which would otherwise allow one to establish the direct relationship between the surface morphology and the composition of the topmost layer that the CO adsorption is sensitive to. Nonetheless, the absolute numbers for CO coverage measured in these experiments (~0.2 ML, at most) indicated the presence of several rather than a single termination, although one might dominate the surface depending on the preparation. For example, the "as-prepared" films showed morphology and CO adsorption properties different from those of the films annealed in UHV to $T > 800$ K. The presence of small two-dimensional islands and clusters, often observed in STM[169a,170,171] and also detected in LEEM experiments,[175] certainly affects establishing the "average" structure.

In contrast to CO, water often dissociates on oxide surfaces.[109] Weiss and co-workers reported several studies on the interaction of water with the iron oxide films.[176] On the FeO(111) monolayer films, water only weakly adsorbs and desorbs intact upon heating above 200 K. (Very recent studies showed that the FeO(111)/Pt(111) film is inert toward water vapor in the pressure range up to several mbar's, but only in the oxygen-free ambient).[177] In contrast, water readily dissociates on the Fe_3O_4(111) films, resulting in hydroxyl groups as detected by UPS/XPS,[176a,b] HREELS,[173] and IRAS.[178] On the basis of a quantitative comparison between the hydroxyl saturation coverage and the defect concentrations, Joseph et al.[176b] ruled out a purely defect-mediated dissociation of water. It was proposed that water dissociation occurs on the regular surface, with OH^- groups bonded to iron cations and the H^+ species to oxygen anions both exposed at the Fe_{tet1}-terminated Fe_3O_4(111) surface (see Figure 67).

Kendelewicz et al.[179] have examined changes in the electronic structure of magnetite (111) single-crystal surfaces after reaction with water vapor ranging from 10^{-9} to 9 Torr and liquid water at 298 K using XPS with a synchrotron radiation source. The results suggested the formation of the hydroxyl groups initially on defect sites. Hydroxylation extends even several layers deep into the bulk at higher water vapor pressures, with a threshold at $\sim 10^{-3}$ mbar at 300 K. Recently, Cutting et al.[180] studied the reaction of a Fe_3O_4(111) crystal with water vapor by STM and UPS/XPS as a function of water partial pressure and temperature. The results point to dissociation to form surface hydroxyls at a partial pressure of 10^{-6} mbar H_2O and a substrate temperature of about 200 K. The comparison with the previous results of Kendelewicz et al.[179] led the authors to the conclusion that an intermolecular mechanism of dissociation is involved. The STM results indicated that dissociation takes place on a termination of Fe_3O_4(111) thought to contain a 1/4 ML of Fe^{3+} ions on top of a close-packed oxygen monolayer, that is, the same termination (see Figure 65a) suggested by experiments on thin films.[173]

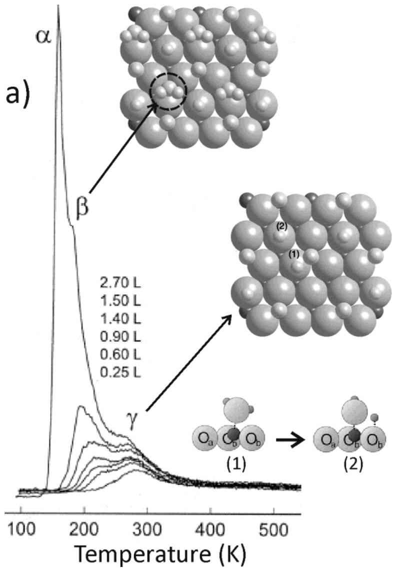

Figure 67. TPD spectra of H_2O adsorbed on Fe_3O_4(111) films at 100 K as a function of water exposure (in langmuirs). The γ peak is assigned to dissociatively adsorbed water on a regular, Fe_{tet1}-terminated surface, resulting in OH^- and H^+ species via heterolytic dissociation as indicated by initial (1) and final (2) states. The β peak is assigned to monomeric water molecules coadsorbed with γ species. Adapted with permission from refs 176a,b. Copyright 2000 American Chemical Society.

Thornton, Vaughan, and co-workers extended adsorption studies of magnetite (111) crystals to formic acid, pyridine, and carbon tetrachloride,[181] which provided additional information to shed light on the surface termination. Solely on the basis of STM images, the authors proposed new, previously not discussed, terminations. One surface termination was thought to be 1/4 ML of Fe_{tet1} ions but each capped by a single oxygen. Another surface termination, previously thought to expose 1/2 ML of equal numbers of octahedral and tetrahedral Fe ions over a close packed oxygen layer, was now regarded as the same arrangement but again with each Fe capped with an oxygen. All of these models imply the formation of ferryl (Fe═O) surface species, which were, however, never observed using IRAS and HREELS of the Fe_3O_4(111) films (but on α-Fe_2O_3(0001) films,[182] see below), which otherwise should show the vibrational band at around 1000 cm^{-1} characteristic for stretching vibrations of metal−oxygen double bond species.[183]

Certainly, the surface structures of Fe_3O_4(111) were the subject of theoretical calculations. One of the first ab initio periodic Hartree−Fock calculations of Ahdjoudj et al.[184] suggested the surface to consist of two outermost iron layers (Fe_{oct2}−Fe_{tet1}), shown in Figure 65b, as the most stable among those arising from an ideal cleavage of bulk. The authors also considered other models, deviating from the bulk stoichiometry, imposing a symmetry between the layers to cancel the net dipole moment of the entire slab. One of the most stable geometries has been found as Fe_{oct2}−Fe_{tet1}−O where all octahedral iron cations are in a +2 valence state, and all tetrahedral ions in a +3 state, that is, in good agreement with CO adsorption results of Lemire et al.[173] Moreover, if switching layers is permitted, the calculations showed that Fe_{tet1} ions go inward and exchange with the underlying oxygen layer. The main driving force for the permutation is the reduction of the local dipole perpendicular to the surface, but the switch seems to require overcoming a barrier. It should be mentioned that the authors were aware that their previous tensor LEED calculations do not match this model well.

Later, bulk-derived terminations of Fe_3O_4(111) were studied by Zhu et al.[185] employing GGA and LDA+U approach at equilibrium with an oxygen environment. Again, the Fe_{oct2}−Fe_{tet1} termination was found to be the most stable. Huang et al.,[186] using GGA+PBE functional, found that the Fe_{tet1} ions in the Fe_{oct2}−Fe_{tet1} terminated model relax even below the underlying O layer, that is, in agreement with the predictions of Ahdjoudj et al.[184] Later, GGA+U approximation was used by Grillo et al.,[187] in particular for the Fe_{oct2}−Fe_{tet1} and Fe_{tet1}-

terminated structures. The results showed that the Fe_{tet1}-terminated surface has the lowest surface energy over the range of relevant oxygen pressures both at 300 and at 1200 K. The authors mentioned, however, that the rates at which oxygen and iron evaporate from the surface might be decisive in the experimentally observed final surface stoichiometry. In such case, the $Fe_{oct2}-Fe_{tet1}$ surface could also appear under oxygen-poor conditions at high temperatures. Very recently, Yu et al.,[188] employing the GGA+U approximation, found that $Fe_{oct2}-Fe_{tet1}$ and Fe_{tet1}-terminated surfaces are, in fact, very close in energy, albeit far more stable than any other, in particular, the O-terminated structures. The charge density plot has revealed that the topmost iron layer is reduced to Fe^{2+}, that is, in agreement with CO adsorption studies of Lemire et al. on the thin films.[173]

Surface science studies on the preparation of magnetite films in other than (111) orientations are rather limited. The $Fe_3O_4(001)$ films grow pseudomorphically on a MgO(001) substrate using MBE.[189] Commonly, the MgO substrates are annealed in oxygen at elevated temperatures prior to the Fe deposition and are kept at ~500 K during the deposition. The growth conditions are critical because the films could be either FeO_x if there is insufficient oxygen or Fe_2O_3 if too high an oxygen pressure used.[189i] The prepared films were quite thick, typically 50−500 nm, and showed atomically flat surfaces in STM.[189c,d] The film surfaces exhibited $(\sqrt{2} \times \sqrt{2})R45°$ reconstruction, also was observed on a $Fe_3O_4(001)$ single crystal.[190] This reconstruction was originally discussed in terms of surface charge neutrality as a driving force. The bulk derived $Fe_3O_4(001)$ surfaces are terminated by either only tetrahedral iron (the so-called A layer) or mixed oxygen and octahedral iron (the so-called B layer). Neither of these terminations is charge compensated. Therefore, the surface structure models considered removal of some surface ions to have a nonpolar surface.[189c]

LEED, XPS, and XPD studies of the MBE grown films by Chambers and co-workers[189b,c] suggested that the surface is terminated with 1/2 ML of tetrahedrally coordinated Fe^{3+} (the so-called A termination; see Figure 68). In addition, the first four interlayer spacings were found to relax by −14%, −57%, −19%, and +29% of the respective bulk value. Mijiritskii and Boerma,[193] based on LEIS measurements in combination with the time-of-flight technique, basically supported this model, albeit the topmost layer was found to relax inward by about 40% (cf., 14% in ref 189c). Later, Chambers and co-workers[194] revisited their own model by analysis of atomically resolved STM images. STM results were best interpreted by assuming an autocompensated B-layer termination (see Figures 68 and 69), which consists of a layer of octahedrally coordinated iron, and tetrahedrally coordinated oxygen, along with one oxygen vacancy per unit cell. The authors noted, however, that the surface termination seemed to critically depend on the method of surface preparation and sample history.

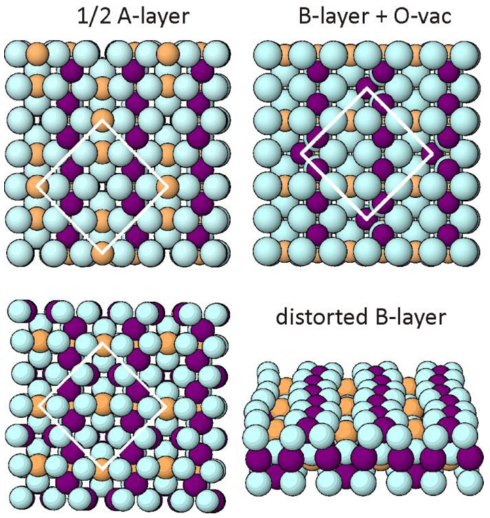

Figure 68. Top panel: Top view of the $(\sqrt{2} \times \sqrt{2})R45°$-reconstructed $Fe_3O_4(001)$ surface exposing a half-filled A-layer (the A-termination) and a B-layer with oxygen vacancies above an octahedral iron (the B-termination). Bottom panel: Top and perspective views of the B-layer exhibiting Jahn−Teller distortion with a wavelike displacement of Fe and O atoms. The $(\sqrt{2} \times \sqrt{2})R45°$ unit cell is indicated. Adapted with permission from refs 191 and 192. Copyright 2005 American Physical Society. Copyright 2008 Elsevier.

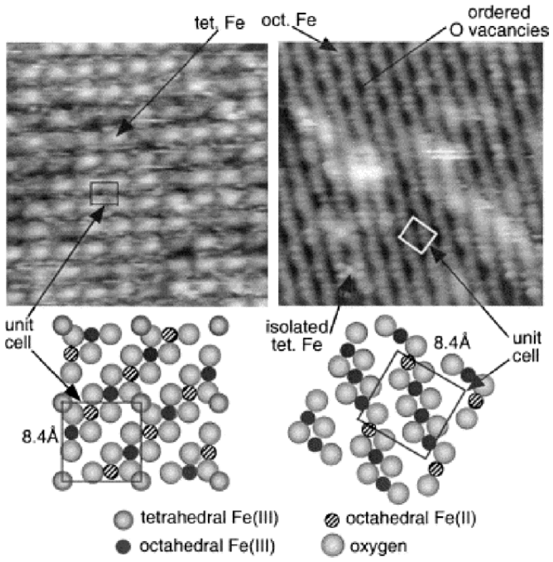

Figure 69. STM images and corresponding models of the $(\sqrt{2} \times \sqrt{2})R45°$- reconstructed surface of $Fe_3O_4(001)$ films grown on MgO(001). (Left) The tetrahedral Fe termination; (right) the octahedral Fe/tetrahedral O termination, with an ordered array of oxygen vacancies. Reprinted with permission from ref 189a. Copyright 2000 Elsevier.

XPS and Raman spectroscopy results of Ruby et al.[195] of thermal stability of the $Fe_3O_4(001)$ films grown on MgO(001) showed Mg migration into the 5 nm-thick films heated at 600 K in synthetic air, thus resulting in ternary compounds like $(Mg_xFe_{1-x})Fe_2O_4$. Meanwhile, the thicker films underwent a $Fe_3O_4 \rightarrow \gamma\text{-}Fe_2O_3$ transformation, that is, the same as observed for bulk materials. The Mg diffusion from the substrate was also detected upon annealing in UHV.[194,196] To better control the surface stoichiometry of the prepared films, Korecki and co-workers[197] suggested preparation of the $Fe_3O_4(001)$ films on an ~20 nm-thick Fe(001) film grown on top of MgO(001) as a buffer layer to block the Mg diffusion to the surface. Beside the better quality of the resulted films (see Figure 70), the comparison revealed that the presence of the Fe blocking layer results in the Fe-rich surface termination different from the B-layer derived model. STM images of these films appear to exhibit Fe dimer species similar to those originally proposed by Rustad et al.[198] on the basis of molecular dynamics simulations.

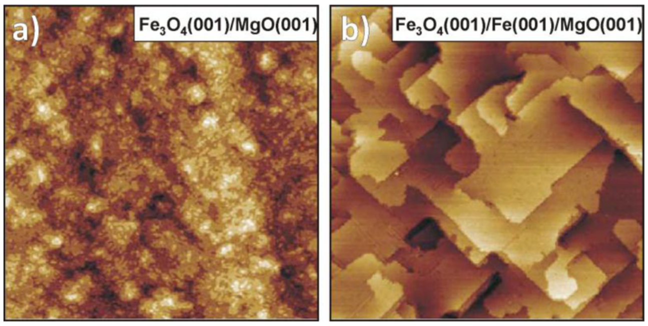

Figure 70. Large-scale STM images (200 nm × 200 nm) of the Fe$_3$O$_4$(001) films MBE-grown directly on MgO(001) (a) and on an additional 20 nm-thick Fe(001) buffer layer on MgO(001) (b). Adapted with permission from ref 197. Copyright 2006 American Physical Society.

In attempts to resolve the long-standing debate on surface terminations, Pentcheva et al.[191] performed a full structural optimization of the models proposed in the literature as well as of the two bulk truncations. The results indicated that the simple ionic picture is not applicable to magnetite. The surface phase diagram constructed in the framework of ab initio thermodynamics revealed that a modified B-layer is stabilized over a broad range of oxygen pressures. Instead of an ordering of surface defects in previously proposed models, the stabilization involves Jahn–Teller distortion with a wavelike displacement of Fe and O atoms in the top B layer, whereby the $(\sqrt{2} \times \sqrt{2})R45°$ superstructure is formed as shown in Figure 68. The DFT results were in fairly good agreement with LEED I/V measurements performed on a Fe$_3$O$_4$(001) crystal (Pendry factor 0.34).[192] Finally, very recent DFT studies of Yu et al.[188] suggested surface energies for the "conventional" A- and B-terminated surfaces in close energetic proximity to other structures, which renders their observations were sensitive to the preparation conditions as many experimental studies reported, indeed.

Recently, Parkinson et al.,[199] utilizing STM, LEIS, and LEED to the synthetic Fe$_3$O$_4$(001) crystal, showed that both the B-termination and a metastable A-termination can be reproducibly prepared within one sputter/anneal cycle through variation of the annealing temperature. More specifically, annealing the Ar$^+$ sputtered surface to 350 °C produces an A-terminated surface with a $(\sqrt{2} \times \sqrt{2})R45°$ superstructure. Within the superstructure, both single Fe atoms and Fe dimer species were observed. The surface was reoxidized upon annealing to higher temperatures, eventually leading to the recovery of the energetically favorable Jahn–Teller distorted surface at 700 °C. The authors concluded that charge compensation arguments based on nominal bulk charges are unreliable for predicting the surface structure of magnetite.

The studies on the preparation of Fe$_3$O$_4$ films in the (110) orientation are scarce. Basically, in a way the Fe$_3$O$_4$(001) films were grown on Mg(001), the Fe$_3$O$_4$(110) films could be prepared on a MgO(110) substrate.[200] Although STM studies revealed one-dimensional reconstruction similar to that observed on a vacuum-annealed (110) single crystal,[201] again, one has to take measures against Mg migration into the iron oxide film. Combined STM/STS and AES results of Maris et al.[200] indicated the segregation of Mg^{2+} through the entire film. The authors suggested a model with a bulk A-type layer containing both octahedral and tetrahedral Fe ions. The Mg^{2+} ions were proposed to intercalate at the interstitial positions in the subsurface region.

Now we address the preparation and the atomic structure of the hematite films, which seems to remain the most challenging and controversial among the iron oxides. According to the bulk phase diagram, Fe$_2$O$_3$ is stable at low temperatures, that is, below 600 K, at any oxygen ambient pressure.[146,155] However, the preparation of the clean Fe$_2$O$_3$ surfaces in UHV using ion sputtering and subsequent annealing in oxygen resulted in surfaces considerably different from that of the bulk as first shown by Henrich and co-workers.[202] The resulting surfaces showed LEED patterns either identical to that observed on Fe$_3$O$_4$(111) or with "floreted" diffraction spots (see, for instance, Figure 71), which were originally attributed to multiple scattering across the interface formed by a thin FeO(111) layer on top of α-Fe$_2$O$_3$(0001).[202b] Further STM studies of Condon et al.[203] showed surface structures very similar, indeed, to those obtained on Fe$_3$O$_4$(111) crystals. More reduced hematite surfaces (typically formed by high temperature annealing in UHV or at low oxygen pressures, i.e., $<10^{-6}$ mbar O$_2$) showed complex surface topography, which allowed one to conclude that the associated floreting in LEED is caused by the long-range order of the superlattice, formed by coexisting FeO(111) and Fe$_2$O$_3$(0001) islands (thereafter referred to as "biphase ordering"),[168,204] and not by multiple scattering. This model was recently revisited by Lanier et al.,[205] who suggested a layered structure of a thin, less than one unit cell thick, Fe$_3$O$_4$(111)-derived overlayer on top of O-terminated α-Fe$_2$O$_3$(0001).

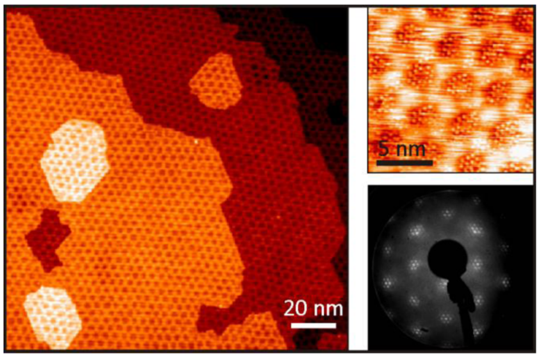

Figure 71. STM images and LEED pattern of the Fe$_2$O$_3$(0001) films grown on Pt(111) under oxygen-lean conditions. (The film is prepared by several cycles of Fe deposition at 300 K and oxidation in 10^{-5} mbar at 900 K; final oxidation was performed at 1100 K).[209]

For the first time, atomically resolved STM images of the unreconstructed hematite (0001) surface were reported by Eggleston and Hochella,[206] who used STM in air to examine natural single crystals cleaved in air. High-resolution STM images revealed a hexagonal array of protrusions with a ~3 Å periodicity, but sometimes with a ~5 Å periodicity, as expected for the O and Fe sublattices in the hematite. However, these studies lacked any additional structural information.

Fujii et al.[207] grew hematite films on sapphire with an MBE technique using NO$_2$ instead of conventional O$_2$. Despite the large (~6%) lattice mismatch between α-Al$_2$O$_3$(0001) and α-Fe$_2$O$_3$(0001), the films exhibited layer-by-layer growth up to a thickness of about a few monolayers. After that, a three-dimensional RHEED pattern developed. Indeed, AFM studies of ~10 ML-thick films showed clustering of three-dimensional nanoparticles.[208] Nonetheless, such systems suffer from low electrical conductivity that renders their surface structure characterization very difficult.

Because the preparation of iron oxide films on metal substrates typically includes a disordered overlayer of iron in different valence states, which is to some extent similar to the hematite crystal surface subjected to ion sputtering, the final structures for both single crystal and thin film systems are mainly determined by high temperature annealing in oxygen. It has been noticed that the formation of unreconstructed α-$Fe_2O_3(0001)$ films occurs at high oxygen pressures, for example, above 10^{-3} mbar.[176c,210] The films prepared either by cycles of Fe deposition and oxidation in 10^{-5} mbar O_2 or by oxidation of a preformed $Fe_3O_4(111)$ film in 10^{-5} mbar at 1000−1100 K showed STM and LEED data characteristic for the biphase-ordered surfaces (Figure 71).

From simple electrostatic considerations, the hematite surface is expected to be terminated by 1/3 ML of Fe over the close-packed oxygen layer as depicted in Figure 63. However, DFT calculations predicted this to be the case only at low oxygen pressures, whereas a bulk-derived oxygen-terminated surface becomes lower in energy at high pressures.[211] Both surfaces are found to be unreconstructed, but strongly relaxed.

The pressure dependence of the hematite surface structure has been shown by STM studies of α-$Fe_2O_3(0001)$ films grown on Pt(111) at different oxygen pressures ranging from 10^{-5} to 1 mbar.[210a] Two surface structures were imaged, which (i) are separated by a step of ∼1.2 Å, (ii) both showed a lattice of protrusions with a ∼5 Å periodicity, but of (iii) clearly different corrugation amplitude (see Figure 72). One structure increased in coverage, while another decreased with increasing oxygen pressure used for the high temperature oxidation. Following the theoretical predictions, these two structures were assigned to the 1 ML O- and 1/3 ML Fe-terminated surfaces, respectively.[210a,212]

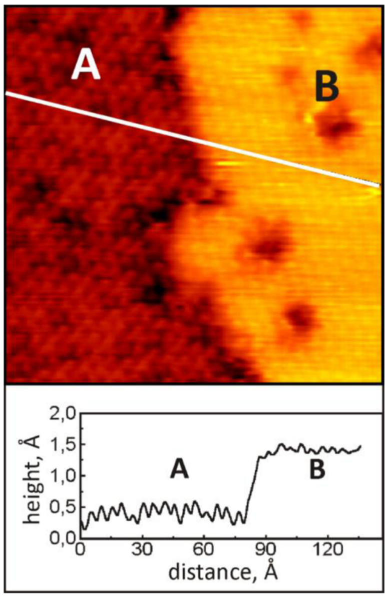

Figure 72. High-resolution STM image (12 nm × 12 nm) and profile line observed for an $Fe_2O_3(0001)$ film, prepared by the growth of $Fe_3O_4(111)$ film on Pt(111) and subsequent oxidation in 0.1 mbar at 1100 K.[210a]

Further LEED studies of similarly prepared films by Ketteler et al.[210b] showed that structural fit of the I/V curves is significantly improved under the assumption that the surface, prepared at 10^{-5} mbar O_2, is additionally terminated by OH species formed as a result of interaction with traces of water in the UHV background, whereas the films prepared at 1 mbar are fully O-terminated. In contrast, Chambers and Yi[213] employing photoelectron diffraction on the films prepared by oxygen plasma assisted MBE on α-$Al_2O_3(0001)$ concluded that the resulting surface is Fe-terminated, despite the highly oxidizing conditions used in these experiments. This finding was considered by the authors as evidence for an autocompensation principle that predicts stability of hematite surfaces.

At this point, it is instructive to recall that surface structures of metal oxides with corundum structure often deviate from those derived by bulk truncation. In particular, $Cr_2O_3(0001)$ films on Cr(110) and $V_2O_3(0001)$ films (and particles) may expose metal−oxygen double bond species (e.g., Cr=O, V=O) that are absent in the bulk structure (see previous sections). However, in contrast to chromyl and vanadyl species, which are well documented in the chemistry of Cr and V compounds, the presence of Fe=O species on iron oxides is thought to be unexpected, as these are only known for mononuclear Fe complexes like in heme-containing enzymes (see, for instance, ref 214). Nonetheless, Bergmeyer et al.[215] and then Rohrbach et al.[75] have considered Fe=O-terminated structures in the DFT calculations, which showed the relative stability of such surface at intermediate oxygen chemical potentials (see Figure 73), although the stability plots derived in these two studies strongly depended on whether the calculations were performed at the GGA level or included a Hubbard-type on-site Coulomb repulsion (the DFT+U approach).

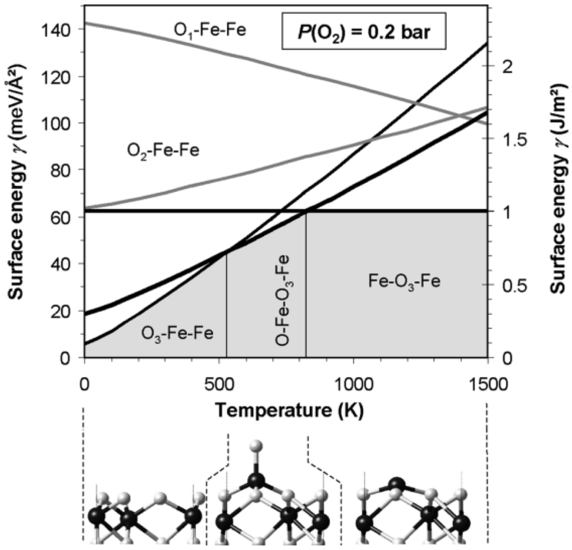

Figure 73. Free energy of a $Fe_2O_3(0001)$ surface, calculated at the DFT-GGA level, as a function of temperature for a constant oxygen partial pressure of 0.2 mbar. The most stable structures are depicted. Reprinted with permission from ref 215. Copyright 2004 American Physical Society.

It is well-known that metal−oxygen double bond species exhibit a characteristic vibrational band around 1000 cm^{-1} assigned to M=O stretching vibrations.[183] Bearing this in mind, IRAS studies of the hematite films grown on Pt(111) have been performed. The IRA spectra revealed, indeed, a prominent signal at ~990 cm^{-1} that grew in intensity and blue-shifted at increasing oxygen pressure, thus providing first direct evidence for the formation of Fe═O species on iron oxide surfaces.[182] The ferryl groups are formed by placing oxygen on top of the iron cations (Figure 73), which in turn terminate the surface at low oxygen chemical potentials, and as such may explain the difference in the corrugation amplitude observed in STM images, where Fe states are probed (Figure 72).[210a] DFT-optimized calculations[182] of a Fe═O stretching frequency yield 981 cm^{-1}, that is, in excellent agreement with the experimental values (~990 cm^{-1}), further supporting the band assignment. Furthermore, CO adsorption on these films revealed an IR peak at 2185 cm^{-1} due to atop CO species on the Fe^{3+} cations,[216] and caused a small shift of the Fe═O band, thus indicating that CO adsorbed on iron cation interacts with neighboring ferryl groups. The results also show that the surface of the hematite films is not uniform and may consist of coexisting different structures.

Jarvis and Chaka[217] theoretically address the question about how molecular oxygen can be dissociated on a surface where reactive iron centers are ~5 Å apart. The authors proposed a cooperative bimolecular mechanism that provides a reasonable pathway (a barrier of only 0.2 eV) for the formation of the ferryl surface termination and should be readily reversible.

Ferryl termination has been invoked by Barbier et al.[218] in the analysis of SXRD data observed for a natural hematite crystal in situ. A transition from oxygen-, to ferryl-, and back to oxygen-terminated surfaces was observed in a reduction−reoxidation cycle. The authors also noted that the results better agree with DFT calculations using the GGA approach rather than calculations at the GGA+*U* level, albeit the latter more accurately describes the bulk properties of hematite.

There are a limited number of studies in the literature on the reactivity of iron oxide thin films beyond adsorption studies of CO and water, discussed above. Weiss and co-workers studied ethylbenzene (EB) dehydrogenation into styrene on different iron oxide films.[155,219] TPD studies showed that styrene adsorbs more strongly than EB on all films, and both molecules adsorb on $Fe_3O_4(111)$ more stronger than on $Fe_2O_3(0001)$ (Figure 74).[219,220] Stationary reaction experiments, performed in a 5:1 mixture of water and EB with a total gas pressure of 3×10^{-6} mbar at 873 K, showed no styrene formation on any films as measured with a mass spectrometer placed in front of the sample.[155]

The catalytic activities of the films at more technically relevant conditions were investigated, using a designated batch reactor with an extremely small volume, in a water−EB mixture of 10:1 and a total gas pressure of 0.6 mbar, where gas composition was determined with a gas chromatograph combined with mass spectrometry.[219b] The experiments showed no styrene formation on the $Fe_3O_4(111)$ films, which can readily be explained by the strong chemisorption of the initially formed styrene inhibiting further EB adsorption. On $Fe_2O_3(0001)$ films, styrene production was found to increase with increasing surface defect concentration as judged by LEED of the films prior to the reaction.[221] The results suggested surface defects as active sites for the dehydrogenation of EB to styrene on unpromoted α-$Fe_2O_3(0001)$. These defects can be steps, vacancies, etc. Weiss and Schlögl[219a] proposed that most likely oxygen anions with a higher basicity are exposed at these defect sites, which can effectively deprotonate the C−H groups of the ethyl group of the EB molecule. Simultaneously or subsequently to this deprotonation, an electron must be transferred from the reaction intermediate to an acidic Fe^{3+} site. This may be one reason that Fe_3O_4 is inactive, because less Fe^{3+} species exist in this phase as compared to $Fe_2O_3(0001)$.

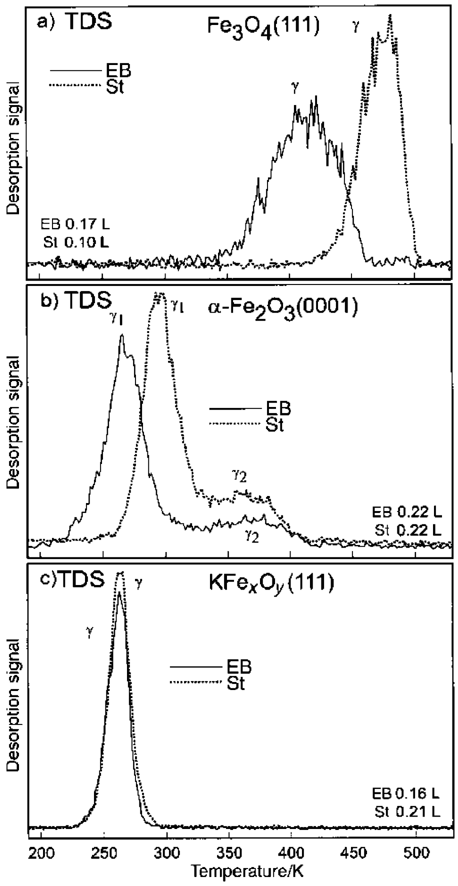

Figure 74. Comparison of TPD spectra of ethylbenzene (EB) and styrene (St) adsorbed at 100 K on $Fe_3O_4(111)$, α-$Fe_2O_3(0001)$, and K-doped $Fe_3O_4(111)$ films (denoted $KFe_xO_y(111)$) at low exposures such that only strongly bound states were populated. Reprinted with permission from ref 219b. Copyright 2000 Springer.

Kuhrs et al.[219b] additionally studied well-ordered K-doped $Fe_3O_4(111)$ films, prepared by K deposition and UHV annealing to ~950 K.[222] These films were used to mimic the industrial catalyst, which is a K-promoted iron oxide, where potassium is thought to increase the number of active sites.[223] TPD spectra showed that EB and styrene adsorb evenly weak on the K-doped $Fe_3O_4(111)$ films (Figure 74), approaching behavior of the FeO(111) films. It turned out that the catalytic activity of α-$Fe_2O_3(0001)$ at 870 K is observed only after an induction period, in this case ~45 min. The postreacted surface was essentially clean, as judged by AES, but showed a high concentration of defects. On the K-doped $Fe_3O_4(111)$ films, the activation period was much longer, but the activity was higher and the surface became completely covered with carbonaceous species. This finding suggested another reaction pathway on the K-promoted films, where a carbon−oxygen species is presumably catalytically active. These results triggered studies on pure carbon materials as effective catalysts of styrene synthesis; see, for instance, ref 224.

The important role of hydroxyls in the EB dehydrogenation was addressed by Huang et al.[225] by employing gas-phase atomic hydrogen. It was shown that hydroxyls react to produce both H_2 and water that cause partial reduction of iron oxide at elevated temperatures. This reduction may enhance the catalytic activity by opening the H_2 desorption channel. However, reduction to magnetite decreases the catalytic activity and has to be prevented by a parallel reoxidation mechanism. Although further experimental evidence is still needed, the authors believe that this explains why the steam included in the feed gas plays a key role. The authors expected that hydrogen production and water formation will also compete for the removal of hydrogen from hydroxyls formed during the course of the catalytic dehydrogenation reactions over other metal oxides.

9. CERIUM OXIDE: $CeO_2(111)$

Ceria (CeO_2) crystallizes in the fluorite structure. When projected to the (111) plane, the structure can be viewed as a stack of O−Ce−O trilayers as shown in Figure 75.

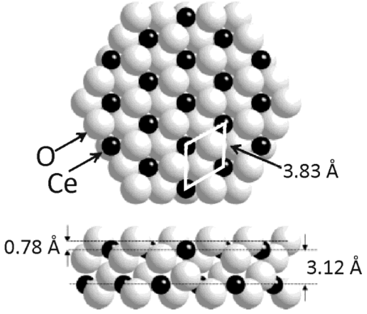

Figure 75. Top and cross views of $CeO_2(111)$.

Stoichiometric ceria is an electrically insulating oxide with a wide band gap (~6.0 eV), but becomes conductive after creating oxygen vacancies, which is accompanied by the reduction of Ce^{4+} ions to Ce^{3+}. It is believed that the electronic states attributed to Ce^{3+} ions at the surface are crucial for catalytic reactions involving ceria.

First reports on the preparation of ceria films can be traced back to the late 1970s. It has been shown that oxidation of metallic Ce foils proceeds through the formation of Ce_2O_3, which is then capped by a thin layer of CeO_2 on the surface.[226] To date, various, both oxide and metal, substrates were used to grow thin ceria film, such as Si (ref 227 and references therein), Ge,[228] $LaAlO_3$,[229] Au,[229] Pd,[229,230] Al_2O_3,[229,231] Ru,[232] Ni,[212,232a] Pt,[233] $SrTiO_3$,[234] yttria-stabilized zirconia (001)[231a,235] and (111),[236] Rh(111),[237] Cu(111),[238] Re(0001),[239] etc. Different deposition techniques were employed, for example, molecular beam epitaxy, laser ablation, physical vapor deposition, magnetron sputtering, etc. In most cases, CeO_2 films in (111) orientation were fabricated. The preparation of other CeO_2 planes as well as of well-ordered Ce_2O_3 phases has been studied to a much lesser extent. As an example, the $CeO_2(001)$ and $CeO_2(110)$ thin films were grown by laser ablation on $SrTiO_3(001)$ and $SrTiO_3(211)$ substrates, respectively.[234] Also, the growth of epitaxial $CeO_2(001)$ films on a Ge(001) substrate,[228] using a hydrogen-assisted pulsed-laser deposition method, as well as on r-cut sapphire[231b] by magnetron sputter deposition has been reported. Reversible transformation of $CeO_2(111)$ to $Ce_2O_3(0001)$ films was observed for films grown on Re(0001).[239] Note also that oxide supports were primarily used for the growth of relatively thick, >50 nm, films, whereas metal single-crystal supports allow one to grow ultrathin ceria overlayers down to one monolayer.

In one of the first comprehensive studies of metal supported ceria films, Nix and co-workers[230] studied the structure of ceria overlayers on Pd(111) using XPS, AES, ISS, and LEED. Low pressure oxidation of the deposited cerium yields a Ce_2O_3 oxide film with a thin capping layer of CeO_2. Although repeated annealing and reoxidation resulted in the formation of more ordered surfaces of CeO_{2-x} stoichiometry, the thermal stability of the oxide film was limited to ~850 K, above which the films decomposed, presumably by diffusion of cerium and oxygen into the Pd substrate. Later, this group used a Cu(111) substrate,[238a] on which well-ordered thick films up to 20 ML in thickness could be prepared by successive cycles of Ce deposition in oxygen ambient at 300 K, followed by annealing to 650−800 K in UHV and reoxidation at 300 K. The authors highlighted that one should minimize extensive alloying that may occur between two metals upon deposition. (Note that the morphology and the defect structure of the ceria films on Cu(111) have only recently been studied by Matolin and co-worker, albeit using a different preparation recipe where Ce is deposited onto the preoxidized, Cu_2O surface.[238b,c])

Hardacre et al.[233a] studied the structure, composition, and stability of ceria films on Pt(111). The oxidation of predeposited Ce films by O_2 and N_2O resulted in the formation of defective (111)-oriented CeO_2 and (0001)-oriented Ce_2O_3 films, respectively. In particular, thick films underwent incomplete oxidation due to passivation by an overlying oxide layer of approximately 1 nm in thickness. At high temperatures (~1000 K), the ceria layers were substantially reduced, ultimately resulting in an ordered Pt/Ce surface alloy seen in LEED as (2 × 2) and (2 × 2)R30° structures. These well-ordered intermetallic surface phases, later identified as Pt_5Ce,[233b,240] were suggested by Schierbaum and Berner[233b,241] as a good starting point for obtaining homogeneous thin layers of ceria by high-temperature oxidation. The resulted films were, to the best of our knowledge, the first ceria films ever studied with STM.[241b] Basically, the STM results showed the formation of two-dimensional islands of $CeO_2(111)$, with the top facets exhibiting a hexagonal lattice of protrusions with a ~4 Å periodicity, which were originally assigned to the outmost O-layer of $CeO_2(111)$. The STM images were, in principle, very similar to those obtained by Nörenberg and Briggs[242] on $CeO_2(111)$ single crystals either at elevated temperatures (570 K) or after high temperature (1000 K) annealing to have the samples electrically conducting.

Netzer and co-workers addressed the initial stages of the film growth on Rh(111).[237] It was shown that ceria follows a Volmer−Weber growth mode, resulting in the formation of well-faceted $CeO_2(111)$ islands of ~15−20 nm in lateral dimensions upon annealing to ~970 K. The ultrathin films contained considerable amounts of Ce^{3+} species, presumably at the ceria/Rh interface. Thicker films (>6 ML) showed aggregates of fully oxidized CeO_2 crystallites, which were difficult to study with a high resolution. Again, the ceria decomposed and Ce−Rh surface alloy phases were observed at high temperatures (>1070 K).

Obviously, in the case of ceria films, the choice of a metal substrate is driven to a lesser extent by the lattice mismatch, because the lattice constants of (111) metal surfaces (ca. 2.5−2.8 Å) are very different from those of $CeO_2(111)$ and $Ce_2O_3(0001)$ surfaces (3.89 and 3.82 Å, respectively). Only for Cu(111), a commensurate structure could be formed due to

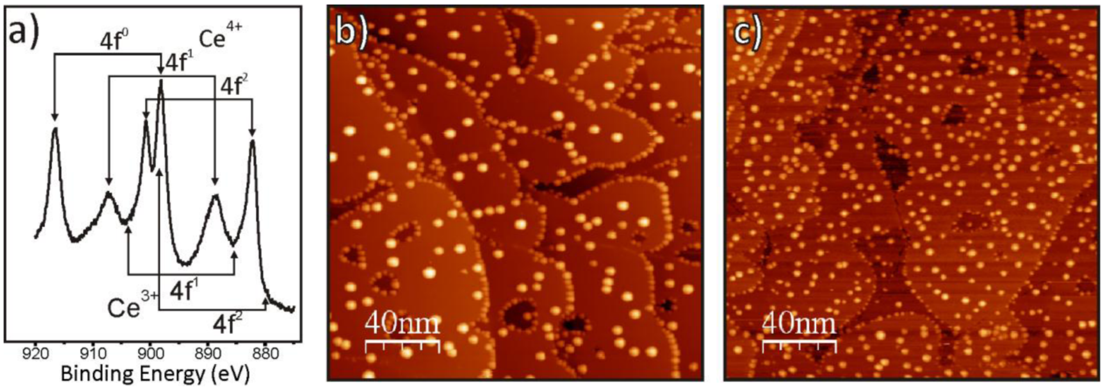

Figure 76. (a) Typical XP spectrum ($h\nu$ = 1020 eV) of the Ce 3d level in the ~3 nm-thick ceria films grown on Ru(0001) showing the abundance of Ce^{4+} species. (b,c) STM images of the $CeO_2(111)$ films with gold deposited on a freshly prepared film (b), and a film annealed in UHV at 1000 K for 5 min (c). Gold particles decorate step edges and defect sites present on the terraces. Reprinted with permission from ref 232c. Copyright 2009 American Chemical Society.

the epitaxial relationship $2a_{CeO2} = 3a_{Cu(111)}$ and $CeO_2[01]$ II Cu[01], thus leading to a (1.5 × 1.5)-Cu(111) LEED pattern.[238c,241c] Apparently, the decisive factor for using a particular substrate for the ceria films is the thermal stability of those systems because of the high temperature annealing that is typically required for preparation of well-ordered oxide films. In this respect, ceria films grown on Ru(0001), extensively studied by Mullins and co-workers,[113,232a,243] seem to show the best performances. The surface is very stable when annealed up to 1000 K, and there is no evidence for ceria alloying with Ru. The original recipe of Mullins et al.[232a] included dosing of Ce in an oxygen ambient 2×10^{-7} mbar on the clean Ru(0001) kept at 700 K, followed by annealing to 900−980 K. Partially reduced $CeO_2(111)$ surfaces were obtained by growing a film at a lower oxygen pressure.

The morphology and atomic structure of relatively thick $CeO_2(111)$/Ru(0001) films covering the entire substrate surface have been studied in our own laboratories.[232b,c] Because the growth of oxide films on metals is often governed by the adhesion energy between an oxide and a substrate, a kinetically limited growth at low temperatures to facilitate the formation of the interfacial ceria layer(s) was suggested. More specifically, the clean Ru(0001) surface was oxidized in 10^{-6} mbar of O_2 at 600 K, and Ce was first deposited in 10^{-6} mbar of O_2 at 100 K (i.e., in contrast to the 700−780 K used previously)[232a,b] in amounts approximately equivalent to form 1−3 monolayers of $CeO_2(111)$ on Ru(0001). The temperature then was slowly increased and kept at 700 K during deposition of further 3−5 monolayers. Finally, the sample was oxidized at ~980 K at the same oxygen pressure. This preparation resulted in films exposing wide atomically flat terraces as shown in Figure 76. From the attenuation of Ru 3d XPS signals, the average film thickness was estimated to be about 3 nm, which corresponds to approximately 6 stacks of O−Ce−O trilayers (see the structure in Figure 75). XPS results also show that the resulted ceria films are fully oxidized because only spectral features of Ce^{4+} are observed (Figure 76a). This conclusion is further supported by STM images of the ceria films, on which small amounts of gold were deposited to decorate the defect sites due to the weak interaction of the Au ad-atoms with the perfect $CeO_2(111)$ surface (see Figure 76b,c).[244] The density of point defects could be determined by counting gold particles on the terraces. On the freshly prepared films, the defect density is very small, indeed, but considerably increases either by vacuum annealing at 1000 K[232c] or by electron bombardment.[245]

Apparently, the nature of the surface defects, which is typically assigned to oxygen vacancies, is the most intriguing issue with respect to ceria surfaces. Considering thin films, one could argue that defect formation and its atomic structure depend on the film thickness. Indeed, STM study of CeO_2/Rh(111) ultrathin films by Castellarin-Cudia et al.[237b] revealed ordered arrays of surface defects, whose formation was attributed to strain at the metal/oxide interface caused by the lattice mismatch. This conclusion was also corroborated by DFT calculations. On the other hand, a very recent STM study of Grinter et al.[246] showed remarkable similarities between the STM images of the ultrathin ceria films on Pt(111) and $CeO_2(111)$ single crystals, thus indicating that an ultrathin film is a good topographic model for the native oxide. It is fair to say that better understanding of ceria surfaces, in particular, of its defect structure, was only possible with the help of scanning probe microscopy techniques (STM and AFM) in combination with high-level DFT calculations.

The first ever reported atomically resolved STM images of $CeO_2(111)$ by Nörenberg and Briggs[242] revealed surface oxygen vacancies, which appeared in STM as triangular defects. Those formed line defects after annealing at high temperatures, presumable by a zipping mechanism. Similar features were observed by Iwasawa and co-workers using noncontact AFM.[247] To explain the atomic STM contrast observed on a partially reduced $CeO_2(111)$ crystal surface at elevated temperatures (~600 K), Esch et al.[248] invoked the presence of subsurface oxygen vacancies, which were implemented in the image simulations by DFT. The authors concluded that clusters of more than two vacancies exclusively expose the reduced, that is, Ce^{3+} ions, primarily by including subsurface vacancies, which play a crucial role in the process of vacancy cluster formation. This study definitely "accelerated" still ongoing debates on a proper description of 4f-metal oxides by first-principle DFT calculations.[249]

It is commonly accepted that two electrons left behind by released oxygen localize on two Ce^{3+} ions. On the basis of DFT results by Ganduglia-Pirovano et al.,[250] these electrons do not necessarily localize on nearest neighbor cerium cations, but rather on the next-nearest ones. This fact, in turn, may have a considerable effect on the relative stability of surface and subsurface oxygen vacancies. Indeed, at high concentration of the oxygen vacancies, the subsurface position turns out to be more stable than the surface position. These findings provide some theoretical support for the experimental results of Reichling's group using dynamic force microscopy (Figure 77).[251] By combining simultaneously acquired signals (the topography and the energy dissipated from cantilever oscillation) of the $CeO_2(111)$ single-crystal surface, it was possible to discriminate surface and subsurface vacancies.

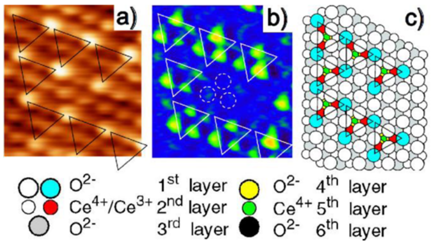

Figure 77. Topography (a) and dissipation (b) images together with the corresponding schematic model (c) of the local ordering of subsurface oxygen vacancies observed by dynamic force microscopy at 80 K on reduced $CeO_2(111)$ single-crystal surfaces. The subsurface oxygen vacancy structures are highlighted by triangles. The dashed circles on (b) indicate a defect free surface area. Adapted with permission from ref 251. Copyright 2007 American Physical Society.

Very recently, spatial correlation between an O vacancy and the associated Ce^{3+} ion pair has been addressed by Jerratsch et al.[245] using low temperature STM of the $CeO_2(111)/Ru(0001)$ films in combination with DFT. The electronic properties of the surface defects were additionally analyzed by tunneling (conductance) spectroscopy. Although the precise position of the two Ce^{3+} ions was not revealed in this study, these cations always sit in different coordination spheres around the defect. The driving force for adopting such open configurations is the ability of the system to relax lattice strain induced by the more spacious Ce^{3+} ion as compared to its Ce^{4+} counterpart. Although the results shed light on the long-standing puzzle on electron localization on defective CeO_2 surfaces, apparently a delicate balance exists between the spatial distribution of oxygen vacancies and associated charge distribution, which may critically depend on the ambient conditions.

In addition to point defects, low coordination sites, for example, at step edges, may also play an important role in the reactivity of ceria, in particular for the nanoparticulate systems. Indeed, the step edges often behave as nucleation centers for supported metal particles (see Figure 76), and a circular shape of terraces, often observed on ceria films,[232b,244] suggests a large variety of these sites. However, the atomic structure and electronic properties of the step edges were studied to a lesser extent. Torbrügge et al.[252] first employed AFM for studying morphology of step structures on a $CeO_2(111)$ crystal that exposed hexagonally shaped islands and etched pits on the wide, atomically smooth terraces. The authors found that the step edges were all oriented along the close-packed oxygen rows in the ⟨110⟩ directions. Therefore, the steps edges expose primarily (001) and (110) nanofacets of one atomic layer in height. The hexagonal shape of the islands indicated almost equal step formation energy for both step terminations.

In a very recent study,[253] it was shown that steps on the $CeO_2(111)$ surface display unusual electronic and electrostatic properties. Depending on the preparation conditions, the formation of ceria ad-islands with hexagonal or triangular shapes was observed, which expose ⟨211⟩ or ⟨110⟩-oriented

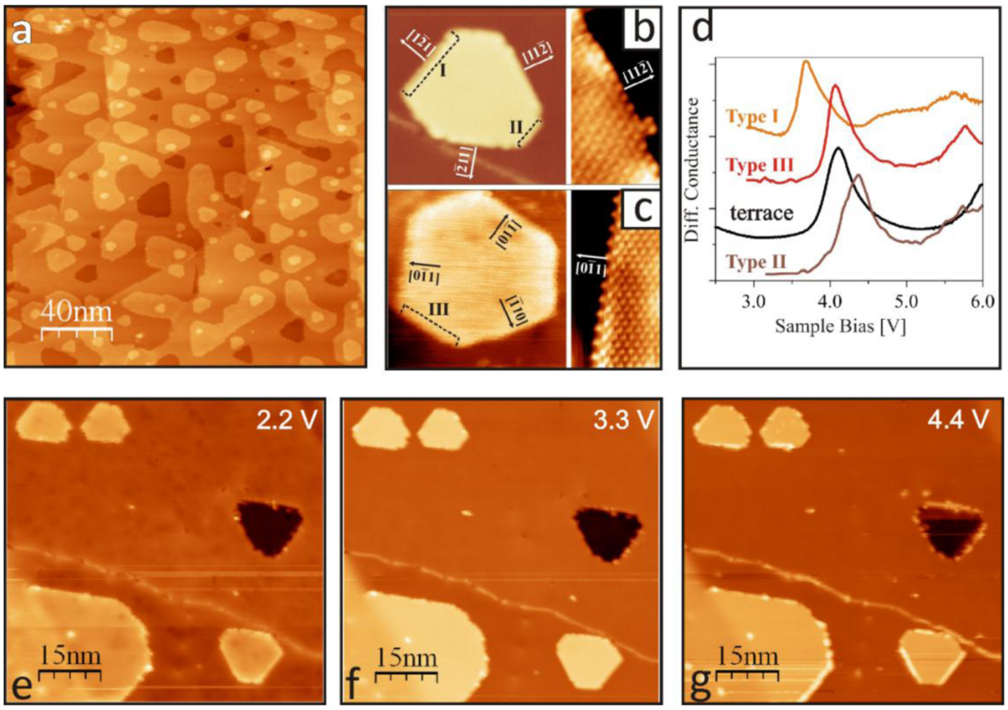

Figure 78. (a) Large-scale STM image of $CeO_2(111)$ thin film exposing monolayer islands and pits. (b,c) Close-up images of a trigonal (b) and hexagonal (c) islands (20 nm × 20 nm) shown with atomic resolution (6 nm × 3 nm (b), 10 nm × 5 nm (c)). The corresponding normal-vectors are indicated. (d) Differential conductance spectra taken over terrace and step edges I, II, and III labeled in (b,c). (e−g) STM images of the same area at three different bias voltages as indicated, which reveal much brighter appearance of type I steps and lines defects at high sample bias. Reprinted with permission from ref.253. Copyright 2011 American Chemical Society.

steps as shown in Figure 78(a-c). Tunneling spectroscopy revealed pronounced differences in the electronic properties of the step edges, as reflected in different onset positions of the ceria conduction band (Figure 78d). The band shifts are related to the development of distinct edge electronic states that split-off from the ceria conduction band, as shown via DFT (GGA +*U*) calculations. The split-off states have significant sp contribution and dominate the tunneling process into the step edges at relatively low sample bias. The edge electronic states develop due to the lower atom-coordination and the more covalent nature of bonds along the step edges. A sizable electrostatic dipole along these steps further promotes the splitting of the corresponding edge states from the main band. As a result, STM contrast of the step edges was strongly dependent on bias such that the steps running in the same directions are imaged unequally (Figure 78e–g). It is plausible that the observed edge morphologies determine not only the electronic properties but also the adsorption behavior at step edges on the $CeO_2(111)$ surface that might be important for catalytic properties of nanosized ceria.

Hardacre et al.[254] studied CO oxidation on ceria films grown on Pt(111) as a function of ceria coverage and morphology. Reactivity was measured in a high-pressure cell used as a batch reactor filled with ~10 Torr of stoichiometric (2:1) CO + O_2 mixture at crystal temperature of 320–430 K. The reaction rate increased between zero and 0.5 ML, after which it dropped almost to zero at 0.8–1.3 ML, but again increased steeply to a value that is much greater than that observed over the clean Pt(111) surface (Figure 79). This very high rate was maintained up to the ~10 ML (only studied in this work). While for the low coverage regime (<1 ML) the reactivity is most likely associated with the metal/oxide interface, the high reactivity of the fully encapsulated Pt(111) (as judged by CO TPD before the reaction) is surprising, indeed, because pure CeO_2 is unreactive for CO oxidation at these low temperatures. This finding was rationalized in terms of a proposal put forward by Frost,[255] according to which electron transfer from a metal phase to an oxide phase reduces the enthalpy for oxygen vacancy formation in the oxide. Although this explanation sounds plausible, the authors argued themselves that there was no absolute evidence of total encapsulation of the Pt crystal with the techniques at their disposal. In particular, the sample morphology after the reaction was undefined in this work. Recent studies[256] of the structure and reactivity of FeO(111) ultrathin films on Pt(111) showed that under O-lean and also stoichiometric conditions (solely used by Hardacre et al.[254]), the originally perfect and dense oxide film dewets, ultimately forming iron oxide nanoparticles dispersed on Pt(111). In principle, such scenario cannot be excluded a priori for the ceria/Pt(111) system. Turning back to the study of Hardacre et al.,[254] disordered ceria films, prepared at low temperatures, were considerably more active than ordered films, prepared by annealing at 900 K. Such phenomena could, in principle, be related to the degree of dewetting; the latter apparently occurs more easily on the originally disordered films.

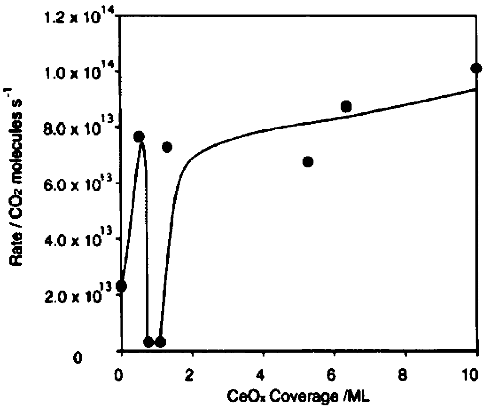

Figure 79. CO oxidation rate over ceria/Pt(111) as a function of ceria coverage at 375 K. Reactivity was measured in a high-pressure cell used as a batch reactor filled with ~10 Torr of stoichiometric (2:1) CO + O_2 mixture. Reprinted with permission from ref 254. Copyright 1994 American Chemical Society.

Another target reaction often used for ceria thin films is methanol dehydrogenation. Siokou and Nix[238a] first studied the adsorption of methanol on ceria films grown on Cu(111). Methanol adsorbs dissociatively at 300 K, with a relatively high sticking probability, to yield surface methoxy species. The IRA spectra of the methoxy species, in particular the C–O stretch frequency, provided information about their coordination to the oxide surface. The authors did not detect any OH species on the oxide by IRAS. The methoxy species were quite stable on the (111) terraces of thick (>5 ML) oxide films and decomposed at ~585 K to yield predominantly H_2 and CO with some simultaneous evolution of formaldehyde and water. The methoxy species, adsorbed at more coordinatively unsaturated cerium ions, were readily oxidized to the formate species, and their decomposition, that occurred at lower temperatures (~560 K), yielded a higher proportion of formaldehyde than was seen for the (111) terrace sites.

Mullins et al.[113] investigated methanol adsorption as a function of temperature and Ce oxidation state on $CeO_2(111)$ films grown on Ru(0001). In addition to TPD, high-resolution XPS and NEXAFS measurements were performed to quantify the amount of methanol adsorbed and to identify the adsorbed species. Methanol reacts at low temperatures with fully oxidized CeO_2 to produce water at 200 K, while formaldehyde and methanol desorb near 560 K. On reduced ceria, more methanol can be adsorbed, and it undergoes more extensive decomposition producing CO and H_2 near 640 K in addition to formaldehyde and water. Basically, CO and H_2 desorption were only seen when the ceria surface was reduced. As the degree of ceria reduction increases, more H_2 and less H_2O are produced. In this regard, the authors concurred with the proposal of Ferriz et al.,[257] who studied CH_3OH adsorption on single-crystal $CeO_2(111)$, CeO_2 grown on yttria-stabilized zirconia, and ceria films on $Al_2O_3(0001)$, that the surfaces previously studied by Siokou and Nix[238a] were not fully oxidized. On the other hand, substantially more methanol chemisorption was observed in the Mullins' TPD experiments than was reported by Ferriz et al.[257] on the oxidized surface. On the basis of this finding, Mullins et al.[113] concluded that, while O vacancies will facilitate methanol adsorption, they are not a necessary condition for methanol adsorption.

In continuation of their works on methanol, Zhou and Mullins[243a] have examined adsorption and reaction of formaldehyde. Formaldehyde does not dissociate on fully oxidized CeO_2 and chemisorbs as dioxymethylene, CH_2O_2. The dioxymethylene decomposes and desorbs as formaldehyde between 200 and 400 K. No other products were found. On reduced ceria, formaldehyde also adsorbs as dioxymethylene. However, a more strongly bound form of dioxymethylene is additionally formed that produces formaldehyde at 440 K.

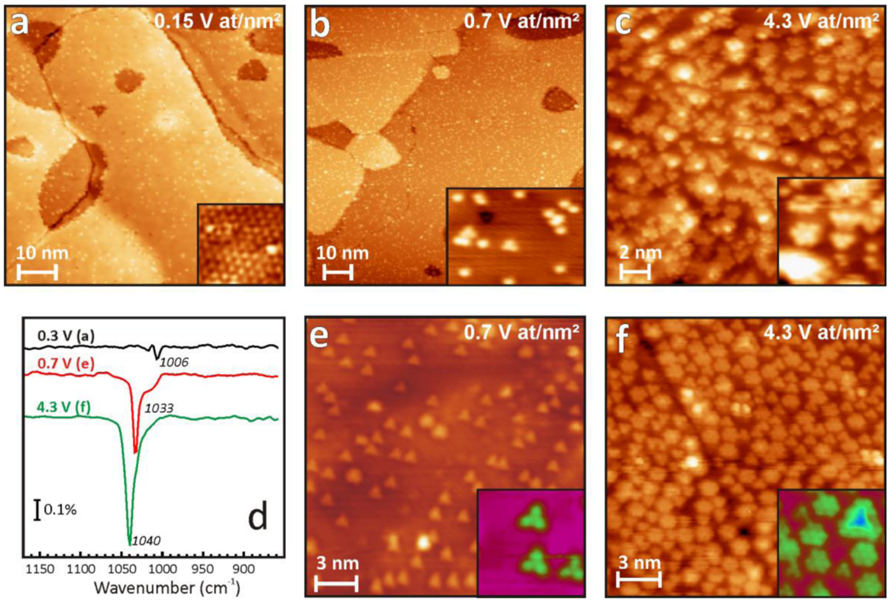

Figure 80. (a−c) STM images of VO_x deposited on $CeO_2(111)$ thin films in oxygen at 300 K with vanadia coverages of 0.15 at./nm^2 (a), 0.70 at./nm^2 (b), and 4.3 at./nm^2 (c). STM images of samples (b) and (c) after annealing to 700 K are shown in (e) and (f), respectively. Insets show high-resolution images of the vanadia species such as monomers, dimers, trimers, and heptamers. IRA spectra of the samples imaged in (a), (e), and (f) are shown in (d). Reprinted with permission from ref 119c. Copyright 2010 Elsevier.

Above 400 K, some of the dioxymethylene reacts to form formate and methoxy on the surface. These species decompose to produce H_2, CO, and CH_2O above 500 K.

10. OXIDE CLUSTERS SUPPORTED ON THIN OXIDE FILMS: $VO_X/CeO_2(111)$

Numerous studies have been reported on the structure and reactivity of planar model systems where the oxide thin films support metal particles like Pd, Rh, Pt, Au, etc. Basically, the reactivity of these systems is determined by the structure of the metal/oxide interface and often involves spillover of reactive species to/from the metal phase. Relatively little is known about the atomic structure and reactivity of oxide supported oxide clusters. Below, we address vanadia clusters as a case study.

Supported vanadium oxide catalysts have received considerable attention due to their high activity for oxidative dehydrogenation (ODH) reactions, for example, the propane-to-propene and methanol-to-formaldehyde reactions.[258] The reactivity has been shown to depend strongly on the oxide support, with reducible oxides (e.g., ceria, titania, and zirconia) exhibiting much higher turnover frequencies than nonreducible oxides (e.g., silica and alumina).[97a,259] Structural characterization of the catalysts, performed primarily using Raman and UV/vis spectroscopy (see ref 97a and references therein), has been used to postulate that vanadia catalysts consist of isolated and polymer structures that wet the supporting oxide (so-called "monolayer catalysts"). However, the atomic structure of vanadia monolayer catalysts, in particular supported on ceria, is the subject of intensive discussions in the literature.

Recently, comprehensive studies of the structure of vanadia clusters on $CeO_2(111)$ thin films as a function of vanadia coverage have been performed. Figure 80 shows STM images of $VO_x/CeO_2(111)$ surface at increasing vanadia coverage, that is, from 0.1 to 4.3 atom/nm^2. Random distribution of vanadia species together with the absence of preferential nucleation sites indicates a strong interaction between vanadia species and the underlying ceria support. In the atomically resolved image (insets of Figure 80a,b), the protruding spots (ca. 3 Å in diameter and 1.2 Å in height) appear to be monomers positioned atop protrusions in the ceria substrate. Increasing vanadia coverage first resulted in a higher density of monomeric species and the simultaneous formation of dimers, trimers, and ill-defined large aggregates with a relatively broad size distribution, which are indicative for kinetically limited growth of the vanadia particles deposited at room temperature. The monomeric species are thermally the least stable. Annealing to 700 K caused monomers to sinter, ultimately producing vanadia trimers and heptamers, particularly at higher coverage. The distance between the protrusions within the trimers and heptamers (∼3.9 Å) is basically the same as measured on the pristine ceria films. The apparent height of these islands, ca. 1.3 Å, is about the same as for monomers. Therefore, the species forming the trimers and larger oligomers occupy the same sites on ceria surface as monomeric species.

The respective IRA spectra revealed only bands at 1000−1040 cm^{-1}, which, combined with the XPS results showing vanadium only in a +5 oxidation state, strongly suggest these species to be vanadyls (V═O) in nature. Tetrahedral VO_4 is anchored to the surface through three O atoms bound to Ce atoms in the film, with one V═O group pointing off the surface. The IRAS band shifts from 1006 cm^{-1} for monomers to 1033 cm^{-1} for trimers and further to 1040 cm^{-1} for heptamers and larger oligomers (see Figure 80d), ultimately approaching the frequencies (∼1045 cm^{-1}) observed for vanadia three-dimensional nanoparticles supported on alumina and silica thin films.[260] This shift can, in principle, be attributed to the onset of dipole coupling between neighboring V═O groups in the oligomers and is fully supported by DFT calculations.[261] Importantly, these results contrast with previous assignments for vanadia/ceria powder catalysts, where the lower Raman frequency (1017 cm^{-1}) was assigned to polymeric species and the higher (1034 cm^{-1}) to isolated species.[262] Therefore, the model systems allowed one to establish a direct structure−spectroscopy correlation for oxide supported vanadia clusters.

These well-defined systems were further studied with respect to oxidative dehydrogenation of methanol with the aim to understand the support effects observed on this reaction on the real catalysts.[119c] Note that methanol oxidation on vanadia supported on both $CeO_2(111)$ single crystal and polycrystalline ceria has previously been studied by the group of Vohs.[119b,d,263] They found that the formaldehyde (FA) desorption temperature resulting from methanol dehydrogenation was dependent on the oxidation state of vanadium. For particles with a predominance of V^{+5} (e.g., in V_2O_5), the desorption of FA was observed at ∼540 K, while for more reduced vanadia particles with a predominance of V^{+3} (e.g., in V_2O_3), the desorption occurred at ∼590 K. The TPD peak of FA from vanadia supported on polycrystalline ceria was found to vary between 525 and 610 K, depending on sample pretreatments.

TPD spectra of methanol on vanadia supported onto ceria thin films are shown in Figure 81 as a function of vanadia coverage.[119c] Prior to the TPD experiments, the "nuclearity" of vanadia deposits was characterized by IRAS based on the above-discussed structure−spectroscopy relationship. At the lowest coverage of vanadia studied in these experiments (1 V at./nm^2), only a relatively sharp peak at 1008 cm^{-1} is observed, thus indicating an abundance of monomeric species. As the coverage increases to 2.7 at./nm^2, an additional feature appears at 1036 cm^{-1} corresponding to trimers; this peak dominates the spectra at the highest coverage studied (i.e., 5.5 V at./nm^2).

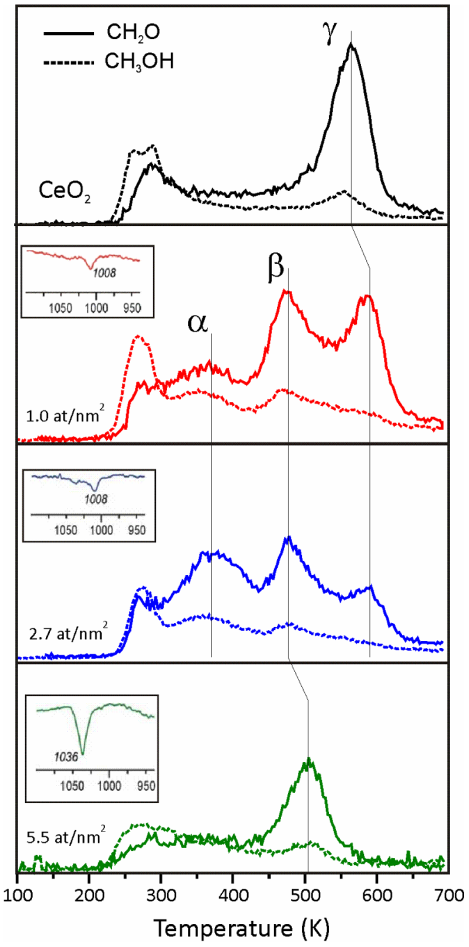

Figure 81. TPD spectra for CH_3OH on VO_x/CeO_2 as a function of vanadia coverage as indicated. Dashed lines indicate the raw signal for CH_3OH (31 amu) desorption, while solid lines indicate CH_2O desorption (i.e., the 29 amu signal corrected for the methanol cracking pattern). Approximately 5 L of CH_3OH was dosed at room temperature. The V═O bands in the respective IRA spectra measured prior to the TPD run are shown as insets. Reprinted with permission from ref 119c. Copyright 2010 Elsevier.

The pristine $CeO_2(111)$ film shows a FA desorption signal at ∼565 K (labeled as γ). In the presence of vanadia, the γ desorption peak shifts to ∼590 K. Note that in these experiments methanol was exposed to the sample at 300 K (i.e., far above the desorption temperature of water (∼200 K) that reduces the ceria surface). Thus, the shifts observed by Mullins et al.[113] for pure ceria films and here for the γ peak on vanadia/ceria most likely have the same origin, that is, reduction of the ceria film. As the coverage of vanadia increases, the integral intensity of the γ peak decreases and finally becomes negligible for the highest VO_x coverage of 5.5 at./nm^2. Two peaks related to the interaction of methanol with the vanadia/ceria surfaces appear at lower temperatures, labeled as α (∼370 K) and β (∼475 K). Only the β peak, shifted to higher temperature (505 K), is observed for the highest coverage of vanadia.

It is clear that the formation of FA in the α state is only observed at low and intermediate vanadia coverages, where monomeric vanadia species have been identified by IRAS. STM study[261] showed that these species exhibit low thermal stability and readily sinter on heating. Indeed, the α peak is not observed during subsequent TPD runs on the same sample. Therefore, the β peak may partially be due to polymeric vanadia species, formed during the temperature ramp. For the highest coverage of vanadia (5.5 at./cm^2) where large polymeric species dominate the surface structure prior to the temperature ramp, the β peak is shifted substantially, and the overall reactivity diminishes. To eliminate the effects of structural changes during TPD acquisition, the samples were preannealed to 700 K in O_2 prior to methanol adsorption at 300 K. The formation of larger vanadia aggregates upon high-temperature annealing, as judged by IRAS, resulted solely in high temperature reactivity at ∼500 K. Interestingly, IRA spectra reveal that the vanadyl species formed after oxidation at 700 K are not consumed upon adsorption of methanol, that is, in contrast to the vanadia/ceria surface formed by oxidation at 300 K. It seems plausible that oxidation at 700 K not only causes sintering of vanadia species but also modifies the Ce surface surrounding vanadyls such that it cannot accommodate methoxy species. Therefore, low temperature reactivity observed for vanadia/ceria relates both to high dispersion of vanadia and to the degree of reduction of the ceria support close to V═O species.

Among several possible schemes for methanol adsorption, the one shown in Figure 82 agrees best with the key experimental findings observed, that is, depletion of the V═O band in IRAS, V reduction in XPS, and available, reduced Ce sites in close proximity to V═O serving as binding sites for

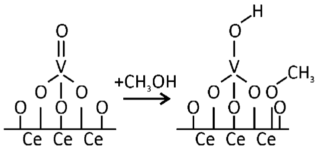

Figure 82. Scheme for methanol adsorption on V═O/$CeO_2(111)$.

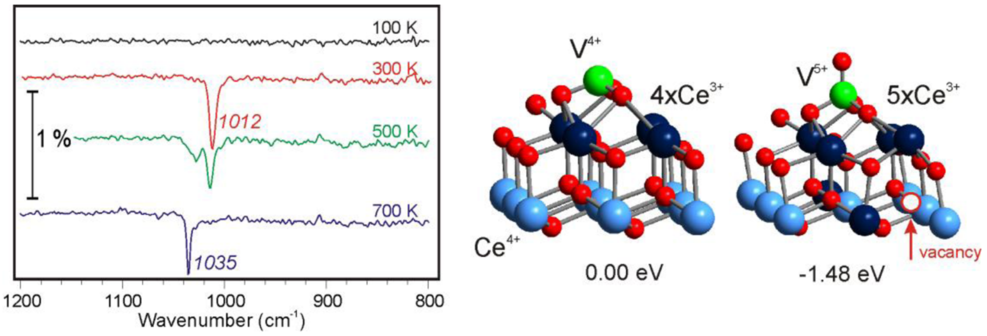

Figure 83. (Left) IRA spectra of $VO_x/CeO_2(111)$ film as deposited at 100 K in UHV and annealed to the indicated temperature. (Right) The structures illustrating the formation of V═O with oxygen from the ceria support upon V atom deposition onto $CeO_2(111)$.

methoxy. It appears that the support effects reported in the literature for real vanadia catalysts[97a] are related to the stabilization of small and isolated vanadia species by reducible oxide supports. Another important factor that controls the reactivity is that ceria stabilizes vanadium in the form of vanadyls. To illustrate this, Figure 83 shows the IRA spectra for the vanadium deposited at 100 K and then stepwise annealed to 300, 500, and 700 K in UHV. The formation of V═O is clearly observed upon annealing to 300 K, which can only be explained by that vanadyl oxygen comes from ceria support. Further annealing causes sintering, which is accompanied by the band shift toward higher frequencies.

The results of DFT calculations nicely prove this scenario.[261] When a V atom is deposited on the perfect $CeO_2(111)$ surface, four electrons are transferred from V 3d states into Ce 4f states, thus creating four Ce^{3+} ions and leaving vanadium in the +4 oxidation state (see Figure 83). There is, however, an isomeric structure of the $V/CeO_2(111)$ system with 1.48 eV less energy, in which oxygen atoms have rearranged such that a vanadyl bond is formed and a subsurface oxygen defect is created in the third oxygen layer of ceria.

Recently, Zhou and Zhou[264] reported XPS and STM studies of titanium vapor-deposited onto $CeO_2(111)/Ru(0001)$ films in UHV. As in the case of vanadia, the titania species strongly interact with the ceria surface forming small atomic-size species randomly dispersed across the surface. On heating to 500 K, these species coalesce into larger aggregates and sometime form chain structures, which are more pronounced at 700 K. The length of the chains ranges from 2 to 15 nm, with most chains basically following three directions with an angle of about 120° between them. Furthermore, the titania chains orient ca. 30° with respect to the Ce atomic rows on the surface. The growth behavior of Ti on the fully oxidized ceria is similar to that on the partially reduced ceria ($CeO_{1.88}$). XPS data indicated that the deposition of Ti on ceria films causes the partial reduction of Ce from +4 to +3 state, with Ti being formally in a fully oxidized, +4 state.

Finally, Matolin and co-workers[265] reported on tungsten interaction with $CeO_2(111)$ layers grown on Cu(111) using primarily XPS and resonant valence band spectroscopy. The results show that W deposits partially reduce ceria at low coverage, whereas the formation of mixed oxide layers is observed at high coverages and at elevated temperatures.

AUTHOR INFORMATION

Corresponding Author

*E-mail: freund@fhi-berlin.mpg.de.

Notes

The authors declare no competing financial interest.

Biographies

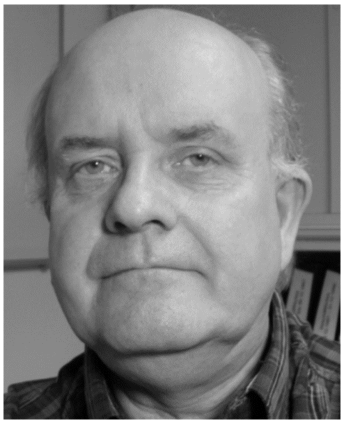

Helmut Kuhlenbeck studied physics at the University of Osnabrück. He received his Ph.D. in 1988 for a study about adsorption on single-crystalline metal. From 1988 to 1996, he worked on topics related to adsorption and reaction of molecules on ordered oxide surfaces at the University of Bochum. In 1995, he finished the habilitation procedure. Since 1996, he is a work group leader at the Chemical Physics department of the Fritz Haber Institute in Berlin. His activities are focused on areas related to model catalysis with emphasis on the spectroscopy of chemical processes on well-ordered oxide surfaces.

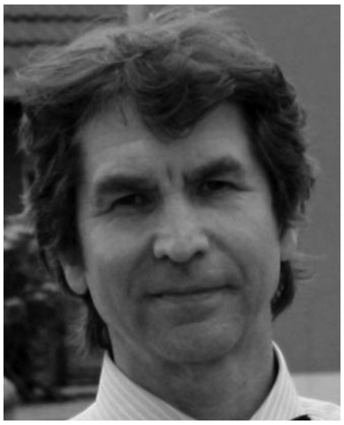

Shamil Shaikhutdinov received his Ph.D. (1986) in Physics at the Moscow Institute of Physics and Technology studying the microwave properties of bio-organic materials and their models. He then joined the Boreskov Institute of Catalysis at Novosibirsk to carry out surface science studies of catalytic systems. From 1994, he worked as a postdoctoral fellow in several research centers in Germany and France. Since 2004, he has been a group leader at the Department of Chemical Physics of the Fritz-Haber Institute in Berlin. His current research is focused on an understanding of structure−reactivity relationships in heterogeneous catalysis.

Hans-Joachim Freund studied physics and chemistry at the University of Cologne where he received his Ph.D. in 1978 and his habilitation in 1983. Between 1979 and 1981, he worked in the Physics Department at the University of Pennsylvania as a postdoctoral fellow. In 1983, he became Associate Professor at Erlangen University and in 1987 Professor at Bochum University, and in 1995, he accepted a position as scientific member and director of the Department of Chemical Physics at the Fritz-Haber-Institut der Max-Planck-Gesellschaft in Berlin. He serves as Honorary Professor of five universities. He received several national and international awards, and he is a member of several academies, scientific societies, and advisory boards of scientific journals.

ACKNOWLEDGMENTS

We acknowledge all past and present collaborators whose names appear in the references, and who have significantly contributed to the work reported here. We thank the German Science Foundation (DFG) for financial support through Sonderforschungsbereich 546 and the Cluster of Excellence UNICAT administrated through TU Berlin. We also thank Fonds der Chemischen Industrie for financial aid. The collaboration within SFB 546 (coordinated by Joachim Sauer at the HU Berlin) has, in particular, contributed significantly to results presented here.

ACRONYMS

ARUPS	angle-resolved ultraviolet photoelectron spectroscopy
BSSE	basis set superposition error
CI	configuration interaction
DFT	density functional theory
DZ	double-ζ
EB	ethylbenzene
EELS	electron energy loss spectroscopy
fcc	face centered cubic
GGA	generalized gradient approximation
GIXS	grazing-incidence X-ray scattering
hcp	hexagonal close-packed
HREELS	high-resolution electron energy loss spectroscopy
IR	infrared
IRAS	infrared reflection absorption spectroscopy
IRS	infrared spectroscopy
IV-LEED	I/V intensity analysis of LEED
LEED	low-energy electron diffraction
LEEM	low-energy electron microscopy
LEIS	low energy ion scattering
MBE	molecular beam epitaxy
NEXAFS	near-edge X-ray absorption fine structure
PED	photoelectron diffraction
PES	photoelectron spectroscopy
PM-IRAS	polarization-modulation infrared reflection absorption spectroscopy
SCF	self-consistent field
SPA-LEED	spot-profile analysis of LEED
STM	scanning tunneling mscroscopy
SXRD	surface X-ray diffraction
THEED	transmission high-energy electron diffraction
TOF	turnover frequency
TPD	temperature programmed desorption
TZP	triple-ζ with polarization
UHV	ultrahigh vacuum
XPS	X-ray photoelectron spectroscopy

REFERENCES

(1) Wichtendahl, R.; Rodriguez-Rodrigo, M.; Härtel, U.; Kuhlenbeck, H.; Freund, H. J. *Phys. Status Solidi A* **1999**, *173*, 93.

(2) (a) Ertl, G.; Küppers, J. *Low Energy Electrons and Surface Chemistry*; Verlag Chemie: Weinheim, 1989. (b) Woodruff, D. P.; Delchar, T. A. *Modern Techniques in Surface Science*; Cambridge Solid State Science Series; Cambridge University Press: Cambridge, 1986. (c) Kevan, S. D., Ed. *Angle Resolved Photoemission: Theory and Current Applications*; Studies in Surface Science and Catalysis 74; Elsevier: Amsterdam, 1992. (d) Eberhardt, W., Ed. *Applications of Synchrotron Radiation*; Springer Series in Surface Sciences 35; Springer: Heidelberg, 1994.

(3) (a) Freund, H. J.; Dillmann, B.; Ehrlich, D.; Haßel, M.; Jaeger, R. M.; Kuhlenbeck, H.; Ventrice, C. A.; Winkelmann, F.; Wohlrab, S.; Xu, C.; Bertrams, T.; Brodde, A.; Neddermeyer, H. *J. Mol. Catal.* **1993**, *82*, 143. (b) Kuhlenbeck, H.; Freund, H.-J. In *Surface Science: Principles and Applications*; Howe, R. F., Lamb, R. N., Wandelt, K., Eds.; Springer Proceedings in Physics 73; Springer: Heidelberg, 1993; p 227. (c) Winkelmann, F.; Wohlrab, S.; Libuda, J.; Bäumer, M.; Cappus, D.; Menges, M.; Al-Shamery, K.; Kuhlenbeck, H.; Freund, H. J. *Surf. Sci.* **1994**, *307*, 1148.

(4) Henrich, V. E.; Cox, P. A. *The Surface Science of Metal Oxides*; Cambridge University Press: Cambridge, 1994.

(5) Bäumer, M.; Cappus, D.; Kuhlenbeck, H.; Freund, H. J.; Wilhelmi, G.; Brodde, A.; Neddermeyer, H. *Surf. Sci.* **1991**, *253*, 116.

(6) Guimond, S.; Sturm, J. M.; Göbke, D.; Romanyshyn, Y.; Naschitzki, M.; Kuhlenbeck, H.; Freund, H. J. *J. Phys. Chem. C* **2008**, *112*, 11835.

(7) (a) Kuhlenbeck, H.; Odörfer, G.; Jaeger, R.; Illing, G.; Menges, M.; Mull, T.; Freund, H. J.; Pöhlchen, M.; Staemmler, V.; Witzel, S.; Scharfschwerdt, C.; Wennemann, K.; Liedtke, T.; Neumann, M. *Phys. Rev. B* **1991**, *43*, 1969. (b) Freund, H. J., Umbach, E., Eds. *Adsorption on Ordered Surfaces of Ionic Solids and Thin Films*; Springer Series in Surface Sciences 33; Springer: Heidelberg, 1993.

(8) Bertrams, T.; Winkelmann, F.; Uttich, T.; Freund, H.-J.; Neddermeyer, H. *Surf. Sci.* **1995**, *333*, 1515.

(9) (a) Farnsworth, H. E.; Tuul, J. *J. Phys. Chem. Solids* **1958**, *9*, 48. (b) Schlier, R. E.; Farnsworth, H. E. *Adv. Catal.* **1957**, *9*, 434. (c) Germer, L. H.; Hartman, C. D. *J. Appl. Phys.* **1960**, *31*, 2085.

(10) Wyckoff, R. W. G. *Crystal Structures*; Wiley-Interscience: New York, 1965.

(11) (a) Ciston, J.; Subramanian, A.; Kienzle, D. M.; Marks, L. D. *Surf. Sci.* **2010**, *604*, 155. (b) Zion, B. D.; Sibener, S. J. *J. Phys. Chem. C* **2008**, *112*, 5961. (c) Zion, B. D.; Sibener, S. J. *J. Chem. Phys.* **2007**, *127*, 154720. (d) Schönnenbeck, M.; Cappus, D.; Klinkmann, J.; Freund, H. J.; Petterson, L. G. M.; Bagus, P. S. *Surf. Sci.* **1996**, *347*,

337. (e) Hannemann, H.; Ventrice, C. A.; Bertrams, T.; Brodde, A.; Neddermeyer, H. *Phys. Status Solidi A* **1994**, *146*, 289.

(12) (a) Kinniburgh, C. G.; Walker, J. A. *Surf. Sci.* **1977**, *63*, 274. (b) Welton-Cook, M. R.; Prutton, M. *J. Phys. C: Solid State Phys.* **1980**, *13*, 3993. (c) Prutton, M.; Walker, J. A.; Welton-Cook, M. R.; Felton, R. C.; Ramsey, J. A. *Surf. Sci.* **1979**, *89*, 95.

(13) Muñoz-Márquez, M. A.; Tanner, R. E.; Woodruff, D. P. *Surf. Sci.* **2004**, *565*, 1.

(14) (a) Steurer, W.; Surnev, S.; Fortunelli, A.; Netzer, F. P. *Surf. Sci.* **2012**, *606*, 803. (b) Großer, S.; Hagendorf, C.; Neddermeyer, H.; Widdra, W. *Surf. Interface Anal.* **2008**, *40*, 1741. (c) Dhaka, A.; Sander, D.; Meyerheim, H. L.; Mohseni, K.; Soyka, E.; Kirschner, J.; Adeagbo, W. A.; Fischer, G.; Ernst, A.; Hergert, W. *Phys. Rev. B* **2011**, *84*, 195441.

(15) (a) Agnoli, S.; Barolo, A.; Granozzi, G.; Ferrari, A. M.; Pisani, C. *J. Phys. Chem. C* **2007**, *111*, 19066. (b) Schoiswohl, J.; Zheng, W.; Surnev, S.; Ramsey, M. G.; Granozzi, G.; Agnoli, S.; Netzer, F. P. *Surf. Sci.* **2006**, *600*, 1099.

(16) (a) van der Heide, P. A. W. *J. Electron Spectrosc. Relat. Phenom.* **2008**, *164*, 8. (b) Schuler, T. M.; Ederer, D. L.; Itza-Ortiz, S.; Woods, G. T.; Callcott, T. A.; Woicik, J. C. *Phys. Rev. B* **2005**, *71*, 115113. (c) Hüfner, S. *Adv. Phys.* **1994**, *43*, 183. (d) Zaanen, J.; Sawatzky, G. A. *Prog. Theor. Phys. Suppl.* **1990**, *101*, 231.

(17) (a) Pinarbasi, M.; Metin, S.; Gill, H.; Parker, M.; Gurney, B.; Carey, M.; Tsang, C. *J. Appl. Phys.* **2000**, *87*, 5714. (b) Tsang, C. H.; Fontana, R. E.; Lin, T.; Heim, D. E.; Gurney, B. A.; Williams, M. L. *IBM J. Res. Dev.* **1998**, *42*, 103.

(18) Girgis, M. J.; Gates, B. C. *Ind. Eng. Chem. Res.* **1991**, *30*, 2021.

(19) Ettler, M.; Timmermann, H.; Malzbender, J.; Weber, A.; Menzler, N. H. *J. Power Sources* **2010**, *195*, 5452.

(20) (a) Mehdaoui, I.; Klüner, T. *J. Phys. Chem. A* **2007**, *111*, 13233. (b) Pacchioni, G.; Di Valentin, C.; Dominguez-Ariza, D.; Illas, F.; Bredow, T.; Klüner, T.; Staemmler, V. *J. Phys.: Condens. Matter* **2004**, *16*, S2497. (c) Di Valentin, C.; Pacchioni, G.; Bredow, T.; Dominguez-Ariza, D.; Illas, F. *J. Chem. Phys.* **2002**, *117*, 2299. (d) Bredow, T. *J. Phys. Chem. B* **2002**, *106*, 7053. (e) Pettersson, L. G. M. *Theor. Chim. Acta* **1994**, *87*, 293. (f) Nygren, M. A.; Pettersson, L. G. M. *J. Chem. Phys.* **1996**, *105*, 9339. (g) Wichtendahl, R.; Rodriguez-Rodrigo, M.; Härtel, U.; Kuhlenbeck, H.; Freund, H. J. *Surf. Sci.* **1999**, *423*, 90.

(21) Shen, S.; Feulner, P.; Umbach, E.; Wurth, W.; Menzel, D. *Z. Naturforsch., A: Phys. Sci.* **1987**, *42*, 1333.

(22) Odörfer, G.; Jaeger, R.; Illing, G.; Kuhlenbeck, H.; Freund, H. J. *Surf. Sci.* **1990**, *233*, 44.

(23) (a) Kuhlenbeck, H.; Odörfer, G.; Jaeger, R.; Xu, C.; Mull, T.; Baumeister, B.; Illing, G.; Menges, M.; Freund, H. J.; Weide, D.; Andresen, P.; Watson, G.; Plummer, E. W. *Vacuum* **1990**, *41*, 34. (b) Mull, T.; Menges, M.; Baumeister, B.; Odörfer, G.; Geisler, H.; Illing, G.; Jaeger, R. M.; Kuhlenbeck, H.; Freund, H. J.; Weide, D.; Schuller, U.; Andresen, P.; Budde, F.; Ferm, P.; Hamza, V.; Ertl, G. *Phys. Scr.* **1990**, *41*, 134.

(24) (a) Horn, K.; DiNardo, J.; Eberhardt, W.; Freund, H. J.; Plummer, E. W. *Surf. Sci.* **1982**, *118*, 465. (b) Norton, P. R.; Tapping, R. L.; Goodale, J. W. *Surf. Sci.* **1978**, *72*, 33. (c) Freund, H. J.; Plummer, E. W. *Phys. Rev. B* **1981**, *23*, 4859. (d) Krause, S.; Mariani, C.; Prince, K. C.; Horn, K. *Surf. Sci.* **1984**, *138*, 305. (e) Heskett, D.; Plummer, E. W.; De Paola, R. A.; Eberhardt, W.; Hoffmann, F. M.; Moser, H. R. *Surf. Sci.* **1985**, *164*, 490. (f) Umbach, E. *Solid State Commun.* **1984**, *51*, 365. (g) Fuggle, J. C.; Umbach, E.; Menzel, D.; Wandelt, K.; Brundle, C. R. *Solid State Commun.* **1978**, *27*, 65.

(25) (a) Freund, H. J.; Bigelow, R. W. *Phys. Scr.* **1987**, *T17*, 50. (b) Freund, H. J.; Slaughter, A. R.; Ballina, S. M.; Banna, M. S.; Bigelow, R. W.; Dick, B.; Lex, J.; Deger, H. M. *J. Chem. Phys.* **1984**, *81*, 2535. (c) Pignataro, S.; Distefano, G. *J. Electron Spectrosc. Relat. Phenom.* **1973**, *2*, 171. (d) Pignataro, S.; DiMarino, R.; Distefano, G. *J. Electron Spectrosc. Relat. Phenom.* **1974**, *4*, 90.

(26) (a) Hermann, K.; Bagus, P. S.; Brundle, C. R.; Menzel, D. *Phys. Rev. B* **1981**, *24*, 7025. (b) Messmer, R. P.; Lamson, S. H. *Chem. Phys. Lett.* **1979**, *65*, 465. (c) Mårtensson, N.; Nilsson, A. *J. Electron Spectrosc. Relat. Phenom.* **1990**, *52*, 1.

(27) Somers, J.; Kordesch, M. E.; Lindner, T.; Conrad, H.; Bradshaw, A. M.; Williams, G. P. *Surf. Sci.* **1987**, *188*, L693.

(28) Janssen, G. J. M.; Nieuwpoort, W. C. *Phys. Rev. B* **1988**, *38*, 3449.

(29) (a) Hoeft, J. T.; Kittel, M.; Polcik, M.; Bao, S.; Toomes, R. L.; Kang, J. H.; Woodruff, D. P.; Pascal, M.; Lamont, C. L. A. *Phys. Rev. Lett.* **2001**, *87*, 086101. (b) Lindsay, R.; Baumgartel, P.; Terborg, R.; Schaff, O.; Bradshaw, A. M.; Woodruff, D. P. *Surf. Sci.* **1999**, *425*, L401. (c) Polcik, M.; Lindsay, R.; Baumgartel, P.; Terborg, R.; Schaff, O.; Kulkarni, S.; Bradshaw, A. M.; Toomes, R. L.; Woodruff, D. P. *Faraday Discuss.* **1999**, *114*, 141.

(30) Redhead, P. A. *Vacuum* **1962**, *12*, 203.

(31) Pacchioni, G.; Bagus, P. S. In *Adsorption on Ordered Surfaces of Ionic Solids and Thin Films*; Freund, H. J., Umbach, E., Eds.; Springer Series in Surface Sciences 33; Springer-Verlag: Berlin, 1993; p 180.

(32) Pöhlchen, M.; Staemmler, V. *J. Chem. Phys.* **1992**, *97*, 2583.

(33) Cappus, D.; Klinkmann, J.; Kuhlenbeck, H.; Freund, H. J. *Surf. Sci.* **1995**, *325*, L421.

(34) Vesecky, S. M.; Xu, X. P.; Goodman, D. W. *J. Vac. Sci. Technol., A* **1994**, *12*, 2114.

(35) Staemmler, V. In *Adsorption on Ordered Surfaces of Ionic Solids and Thin Films*; Freund, H. J., Umbach, E., Eds.; Springer Series in Surface Sciences 33; Springer-Verlag: Berlin, 1993; p 169.

(36) Chen, L. J.; Wu, R. Q.; Kioussis, N.; Zhang, Q. M. *Chem. Phys. Lett.* **1998**, *290*, 255.

(37) Neyman, K. M.; Ruzankin, S. P.; Rösch, N. *Chem. Phys. Lett.* **1995**, *246*, 546.

(38) He, J.-W.; Estrada, C. A.; Corneille, J. S.; Ming-Cheng, W.; Goodman, D. W. *Surf. Sci.* **1992**, *261*, 164.

(39) Furuyama, S.; Fujii, H.; Kawamura, M.; Morimoto, T. *J. Phys. Chem.* **1978**, *82*, 1028.

(40) (a) Habenschaden, E.; Küppers, J. *Surf. Sci.* **1984**, *138*, L147. (b) Pfnür, H.; Feulner, P.; Menzel, D. *J. Chem. Phys.* **1983**, *79*, 4613. (c) Chittenden, C. N.; Pylant, E. D.; Schwaner, A. L.; White, J. M. In *The Handbook of Surface Imaging and Visualization*; Hubbard, A. T., Ed.; CRC Press: Boca Raton, FL, 1995; p 817.

(41) Schlichting, H.; Menzel, D. *Rev. Sci. Instrum.* **1993**, *64*, 2013.

(42) (a) Valero, R.; Gomes, J. R. B.; Truhlar, D. G.; Illas, F. *J. Chem. Phys.* **2010**, *132*, 104701. (b) Dominguez-Ariza, D.; Illas, F.; Bredow, T.; Di Valentin, C.; Pacchioni, G. *Mol. Phys.* **2003**, *101*, 241. (c) Di Valentin, C.; Pacchioni, G.; Chiesa, M.; Giamello, E.; Abbet, S.; Heiz, U. *J. Phys. Chem. B* **2002**, *106*, 1637.

(43) Tasker, P. W. *J. Phys. C: Solid State Phys.* **1979**, *12*, 4977.

(44) Gajdardziska-Josifovska, M.; Plass, R.; Schofield, M. A.; Giese, D. R.; Sharma, R. *J. Electron Microsc.* **2002**, *51*, S13.

(45) Noguera, C. *J. Phys.: Condens. Matter* **2000**, *12*, R367.

(46) Goniakowski, J.; Finocchi, F.; Noguera, C. *Rep. Prog. Phys.* **2008**, *71*, 016501.

(47) Wolf, D. *Phys. Rev. Lett.* **1992**, *68*, 3315.

(48) (a) MacRae, A. U. *Appl. Phys. Lett.* **1963**, *2*, 88. (b) MacRae, A. U. *Science* **1963**, *139*, 379.

(49) (a) Carson, G. A.; Nassir, M. H.; Wulser, K. W.; Langell, M. A. *Surf. Sci. Spectra* **1998**, *5*, 229. (b) Barbier, A.; Renaud, G. *Surf. Sci.* **1997**, *392*, L15. (c) Barbier, A.; Renaud, G.; Stierle, A. *Surf. Sci.* **1998**, *402*, 757. (d) Barbier, A.; Renaud, G.; Mocuta, C.; Stierle, A. *Surf. Sci.* **1999**, *433*, 761. (e) Barbier, A.; Mocuta, C.; Renaud, G. *Phys. Rev. B* **2000**, *62*, 16056. (f) Barbier, A.; Mocuta, C.; Neubeck, W.; Mulazzi, M.; Yakhou, F.; Chesnel, K.; Sollier, A.; Vettier, C.; de Bergevin, F. *Phys. Rev. Lett.* **2004**, *93*, 257208.

(50) (a) Langell, M. A.; Berrie, C. L.; Nassir, M. H.; Wulser, K. W. *Surf. Sci.* **1994**, *320*, 25. (b) Warren, O. L.; Thiel, P. A. *J. Chem. Phys.* **1994**, *100*, 659. (c) Langell, M. A.; Nassir, M. H. *J. Phys. Chem.* **1995**, *99*, 4162.

(51) (a) Demuth, J. E. *Surf. Sci.* **1977**, *69*, 365. (b) Cappus, D.; Xu, C.; Ehrlich, D.; Dillmann, B.; Ventrice, C. A.; Al-Shamery, K.; Kuhlenbeck, H.; Freund, H. J. *Chem. Phys.* **1993**, *177*, 533. (c) Conrad, H.; Ertl, G.; Küppers, J.; Latta, E. E. *Solid State Commun.* **1975**, *17*, 497. (d) Cappus, D.; Haßel, M.; Neuhaus, E.; Heber, M.; Rohr, F.; Freund, H. J. *Surf. Sci.* **1995**, *337*, 268. (e) Hildebrandt, S.; Hagendorf,

C.; Doege, T.; Jeckstiess, C.; Kulla, R.; Neddermeyer, H.; Uttich, T. *J. Vac. Sci. Technol., A* **2000**, *18*, 1010. (f) Bandara, A.; Kubota, J.; Onda, K.; Wada, A.; Domen, K.; Hirose, C. *Surf. Sci.* **1999**, *433*, 83. (g) Domen, K.; Bandara, A.; Kubota, J.; Onda, K.; Wada, A.; Kano, S. S.; Hirose, C. *Surf. Sci.* **1999**, *427−428*, 349. (h) Tyuliev, G. T.; Kostov, K. L. *Phys. Rev. B* **1999**, *60*, 2900. (i) Matsumoto, T.; Kubota, J.; Kondo, J. N.; Hirose, C.; Domen, K. *Langmuir* **1999**, *15*, 2158. (j) Bandara, A.; Kubota, J.; Wada, A.; Domen, K.; Hirose, C. *Appl. Phys. B: Lasers Opt.* **1999**, *68*, 573. (k) Hirose, C.; Bandara, A.; Katano, S.; Kubota, J.; Wada, A.; Domen, K. *Appl. Phys. B: Lasers Opt.* **1999**, *68*, 559. (l) Kitakatsu, N.; Maurice, V.; Hinnen, C.; Marcus, P. *Surf. Sci.* **1998**, *407*, 36. (m) Bandara, A.; Kubota, J.; Wada, A.; Domen, K.; Hirose, C. *Surf. Sci.* **1996**, *364*, L580. (n) Bandara, A.; Kubota, J.; Wada, A.; Domen, K.; Hirose, C. *J. Phys. Chem.* **1996**, *100*, 14962. (o) Kubota, J.; Bandara, A.; Wada, A.; Domen, K.; Hirose, C. *Surf. Sci.* **1996**, *368*, 361. (p) Bandara, A.; Kubota, J.; Wada, A.; Domen, K.; Hirose, C. *J. Phys. Chem. B* **1997**, *101*, 361. (q) Bandara, A.; Dobashi, S.; Kubota, J.; Onda, K.; Wada, A.; Domen, K.; Hirose, C.; Kano, S. S. *Surf. Sci.* **1997**, *387*, 312. (r) Matsumoto, T.; Bandara, A.; Kubota, J.; Hirose, C.; Domen, K. *J. Phys. Chem. B* **1998**, *102*, 2979. (s) Bandara, A.; Kubota, J.; Onda, K.; Wada, A.; Kano, S. S.; Domen, K.; Hirose, C. *J. Phys. Chem. B* **1998**, *102*, 5951. (t) Kitakatsu, N.; Maurice, V.; Marcus, P. *Surf. Sci.* **1998**, *411*, 215. (u) Peng, G. W.; Merte, L. R.; Knudsen, J.; Vang, R. T.; Laegsgaard, E.; Besenbacher, F.; Mavrikakis, M. *J. Phys. Chem. C* **2010**, *114*, 21579. (v) Flege, J. I.; Meyer, A.; Falta, J.; Krasovskii, E. E. *Phys. Rev. B* **2011**, *84*, 115441. (w) Okazawa, T.; Nishizawa, T.; Nishimura, T.; Kido, Y. *Phys. Rev. B* **2007**, *75*, 033413. (x) Yeo, B. S.; Chen, Z. H.; Sim, W. S. *Surf. Sci.* **2004**, *557*, 201. (y) Horgan, A. M.; Dalins, I. *Surf. Sci.* **1973**, *36*, 526. (z) Holloway, P. H.; Hudson, J. B. *Surf. Sci.* **1974**, *43*, 141. (aa) Eastman, D. E.; Cashion, J. K. *Phys. Rev. Lett.* **1971**, *27*, 1520.

(52) (a) Marre, K.; Neddermeyer, H. *Surf. Sci.* **1993**, *287*, 995. (b) Rohr, F.; Wirth, K.; Libuda, J.; Cappus, D.; Bäumer, M.; Freund, H. J. *Surf. Sci.* **1994**, *315*, L977. (c) Ventrice, C. A.; Bertrams, T.; Hannemann, H.; Brodde, A.; Neddermeyer, H. *Phys. Rev. B* **1994**, *49*, 5773. (d) Barbier, A.; Mocuta, C.; Kuhlenbeck, H.; Peters, K. F.; Richter, B.; Renaud, G. *Phys. Rev. Lett.* **2000**, *84*, 2897.

(53) (a) Xu, C.; Goodman, D. W. *J. Chem. Soc., Faraday Trans.* **1995**, *91*, 3709. (b) Xu, C.; Goodman, D. W. *Catal. Today* **1996**, *28*, 297. (c) Wang, S.; Liu, S. M.; Guo, J. D.; Wu, K. H.; Guo, Q. L. *Surf. Sci.* **2012**, *606*, 378.

(54) Mocuta, C.; Barbier, A.; Renaud, G.; Samson, Y.; Noblet, M. *J. Magn. Magn. Mater.* **2000**, *211*, 283.

(55) Lorenz, M.; Schulze, M. *Surf. Sci.* **2000**, *454*, 234.

(56) Erdman, N.; Warschkow, O.; Ellis, D. E.; Marks, L. D. *Surf. Sci.* **2000**, *470*, 1.

(57) (a) Collazo-Davila, C.; Grozea, D.; Marks, L. D.; Feidenhans'l, R.; Nielsen, M.; Seehofer, L.; Lottermoser, L.; Falkenberg, G.; Johnson, R. L.; Gothelid, M.; Karlsson, U. *Surf. Sci.* **1998**, *418*, 395. (b) Marks, L. D. *Phys. Rev. B* **1999**, *60*, 2771.

(58) Ciston, J.; Subramanian, A.; Marks, L. D. *Phys. Rev. B* **2009**, *79*, 085421.

(59) Ebensperger, C.; Meyer, B. *Phys. Status Solidi B* **2011**, *248*, 2229.

(60) Floquet, N.; Dufour, L. C. *Surf. Sci.* **1983**, *126*, 543.

(61) Zhang, W. B.; Tang, B. Y. *J. Chem. Phys.* **2008**, *128*, 124703.

(62) Knudsen, J.; Merte, L. R.; Peng, G. W.; Vang, R. T.; Resta, A.; Laegsgaard, E.; Andersen, J. N.; Mavrikakis, M.; Besenbacher, F. *ACS Nano* **2010**, *4*, 4380.

(63) (a) Zhang, W. B.; Tang, B. Y. *The . Chem. Phys.* **2008**, *128*, 124703. (b) Freund, H. J. *Angew. Chem., Int. Ed.* **1997**, *36*, 452.

(64) Saeki, I.; Sugiyama, Y.; Hayashi, S.; Yamauchi, A.; Doi, T.; Nishiyama, Y.; Kyo, S.; Suzuki, S.; Sato, M.; Fujimoto, S. *Corros. Sci.* **2012**, *55*, 219.

(65) Yermakov, Y.; Zakharov, V. *Adv. Catal.* **1975**, *24*, 173.

(66) Conner, W. C.; Kokes, R. J. *J. Phys. Chem.* **1969**, *73*, 2436.

(67) Kung, H. H. *Transition Metal Oxides: Surface Chemistry and Catalysis*; Studies in Surface Science and Catalysis 45; Elsevier: Ansterdam, 1989.

(68) Kuhlenbeck, H.; Xu, C.; Dillmann, B.; Haßel, M.; Adam, B.; Ehrlich, D.; Wohlrab, S.; Freund, H. J.; Ditzinger, U. A.; Neddermeyer, H.; Neuber, M.; Neumann, M. *Ber. Bunsen-Ges. Phys. Chem.* **1992**, *96*, 15.

(69) Henderson, M. A.; Chambers, S. A. *Surf. Sci.* **2000**, *449*, 135.

(70) Priyantha, W. A. A.; Waddill, G. D. *Surf. Sci.* **2005**, *578*, 149.

(71) Pancotti, A.; de Siervo, A.; Carazzolle, M. F.; Landers, R.; Kleiman, G. G. *Top. Catal.* **2011**, *54*, 90.

(72) Huggins, C. P.; Nix, R. M. *Surf. Sci.* **2005**, *594*, 163.

(73) (a) Lübbe, M.; Moritz, W. *J. Phys.: Condens. Matter* **2009**, *21*, 134010. (b) Bikondoa, O.; Moritz, W.; Torrelles, X.; Kim, H. J.; Thornton, G.; Lindsay, R. *Phys. Rev. B* **2010**, *81*, 205439.

(74) (a) Rohr, R.; Bäumer, M.; Freund, H. J.; Mejias, J. A.; Staemmler, V.; Müller, S.; Hammer, L.; Heinz, K. *Surf. Sci.* **1997**, *389*, 391. (b) Rohr, F.; Bäumer, M.; Freund, H. J.; Mejias, J. A.; Staemmler, V.; Müller, S.; Hammer, L.; Heinz, K. *Surf. Sci.* **1997**, *372*, L291. (c) Gloege, T.; Meyerheim, H. L.; Moritz, W.; Wolf, D. *Surf. Sci.* **1999**, *441*, L917.

(75) Rohrbach, A.; Hafner, J.; Kresse, G. *Phys. Rev. B* **2004**, *70*, 125426.

(76) Bender, M.; Ehrlich, D.; Yakovkin, I. N.; Rohr, F.; Bäumer, M.; Kuhlenbeck, H.; Freund, H. J.; Staemmler, V. *J. Phys.: Condens. Matter* **1995**, *7*, 5289.

(77) Maurice, V.; Cadot, S.; Marcus, P. *Surf. Sci.* **2000**, *458*, 195.

(78) (a) Wang, X. G.; Smith, J. R. *Phys. Rev. B* **2003**, *68*, 201402. (b) Rehbein, C.; Harrison, N. M.; Wander, A. *Phys. Rev. B* **1996**, *54*, 14066. (c) Cline, J. A.; Rigos, A. A.; Arias, T. A. *J. Phys. Chem. B* **2000**, *104*, 6195.

(79) (a) Dillmann, B.; Rohr, F.; Seiferth, O.; Klivenyi, G.; Bender, M.; Homann, K.; Yakovkin, I. N.; Ehrlich, D.; Bäumer, M.; Kuhlenbeck, H.; Freund, H. J. *Faraday Discuss.* **1996**, *105*, 295. (b) Henderson, M. A.; Rosso, K. M. *Surf. Sci.* **2011**, *605*, 555.

(80) (a) Henderson, M. A. *Surf. Sci.* **2010**, *604*, 1800. (b) Henderson, M. A. *Surf. Sci.* **2010**, *604*, 1502.

(81) Maurice, V.; Cadot, S.; Marcus, P. *Surf. Sci.* **2001**, *471*, 43.

(82) Hemmerich, I.; Rohr, F.; Seiferth, O.; Dillmann, B.; Freund, H. J. *Z. Phys. Chem. (Muenchen, Ger.)* **1997**, *202*, 31.

(83) Zecchina, A.; Groppo, E. *Proc. R. Soc. London, Ser. A* **2012**, *468*, 2087.

(84) (a) Staudt, T.; Lykhach, Y.; Tsud, N.; Skala, T.; Prince, K. C.; Matolin, V.; Libuda, J. *J. Phys. Chem. C* **2011**, *115*, 8716. (b) Senanayake, S. D.; Stacchiola, D.; Evans, J.; Estrella, M.; Barrio, L.; Perez, M.; Hrbek, J.; Rodriguez, J. A. *J. Catal.* **2010**, *271*, 392. (c) Preda, G.; Pacchioni, G.; Chiesa, M.; Giamello, E. *J. Phys. Chem. C* **2008**, *112*, 19568.

(85) Seiferth, O.; Wolter, K.; Dillmann, B.; Klivenyi, G.; Freund, H. J.; Scarano, D.; Zecchina, A. *Surf. Sci.* **1999**, *421*, 176.

(86) (a) Borowski, S.; Klüner, T.; Freund, H. J.; Klinkmann, I.; Al-Shamery, K.; Pykavy, M.; Staemmler, V. *Appl. Phys. A: Mater. Sci. Process* **2004**, *78*, 223. (b) Pykavy, M.; Thiel, S.; Klüner, T. *J. Phys. Chem. B* **2002**, *106*, 12556. (c) Thiel, S.; Klüner, T.; Lemoine, D.; Freund, H. J. *Chem. Phys.* **2002**, *282*, 361. (d) Thiel, S.; Pykavy, M.; Klüner, T.; Freund, H. J.; Kosloff, R.; Staemmler, V. *J. Chem. Phys.* **2002**, *116*, 762. (e) Pykavy, M.; Staemmler, V.; Seiferth, O.; Freund, H. J. *Surf. Sci.* **2001**, *479*, 11. (f) Thiel, S.; Pykavy, M.; Klüner, T.; Freund, H. J.; Kosloff, R.; Staemmler, V. *Phys. Rev. Lett.* **2001**, *87*, 077601. (g) Beauport, I.; AlShamery, K.; Freund, H. J. *Surf. Sci.* **1996**, *363*, 252. (h) Beauport, I.; AlShamery, K.; Freund, H. J. *Chem. Phys. Lett.* **1996**, *256*, 641. (i) Alshamery, K.; Beauport, I.; Freund, H. J.; Zacharias, H. *Chem. Phys. Lett.* **1994**, *222*, 107. (j) Xu, C.; Dillmann, B.; Kuhlenbeck, H.; Freund, H. J. *Phys. Rev. Lett.* **1991**, *67*, 3551.

(87) Davenport, J. W. *Phys. Rev. Lett.* **1976**, *36*, 945.

(88) (a) Plummer, E. W.; Eberhardt, W. *Adv. Chem. Phys.* **1982**, *49*, 533. (b) Freund, H. J.; Neumann, M. *Appl. Phys. A: Mater. Sci. Process* **1988**, *47*, 3.

(89) (a) Schmeisser, D.; Greuter, F.; Plummer, E. W.; Freund, H. J. *Phys. Rev. Lett.* **1985**, *54*, 2095. (b) Freund, H. J.; Eberhardt, W.; Heskett, D.; Plummer, E. W. *Phys. Rev. Lett.* **1983**, *50*, 768. (c) Turner, D. W.; Baker, C.; Baker, A. D.; Brundle, C. R. *Molecular Photoelectron*

Spectroscopy; Wiley-Interscience: New York, 1970. (d) Jacobi, K.; Astaldi, C.; Geng, P.; Bertolo, M. *Surf. Sci.* **1989**, *223*, 569. (e) Schneider, C.; Steinrück, H. P.; Heimann, P.; Pache, T.; Glanz, M.; Eberle, K.; Umbach, E.; Menzel, D. *Bessy Annual Rep.* **1987**, 313. (f) Shinn, N. D. *J. Vac. Sci. Technol., A* **1986**, *4*, 1351.

(90) Blyholder, G. *J. Phys. Chem.* **1964**, *68*, 2772.

(91) (a) Shinn, N. D.; Madey, T. E. *J. Chem. Phys.* **1985**, *83*, 5928. (b) Shinn, N. D. *Phys. Rev. B* **1988**, *38*, 12248.

(92) (a) Calderon, H. A.; Niehus, H.; Freitag, B.; Wall, D.; Stavale, F.; Achete, C. A. In *Electron Crystallography for Materials Research and Quantitative Characterization of Nanostructured Materials*; Moeck, P., Hovmoller, S., Nicolopoulos, S., Rouvimov, S., Petkov, V., Gateshki, M., Fraundorf, P., Eds.; Materials Research Society Symposium Proceedings 1184; Materials Research Society: Warrendale, 2009; p 203. (b) Sass, B.; Buschhorn, S.; Felsch, W.; Schmitz, D.; Imperia, P. *J. Magn. Magn. Mater.* **2006**, *303*, 167.

(93) (a) Luo, Q.; Guo, Q. L.; Wang, E. G. *Appl. Phys. Lett.* **2004**, *84*, 2337. (b) Pfuner, F.; Schoiswohl, J.; Sock, M.; Surnev, S.; Ramsey, M. G.; Netzer, F. P. *J. Phys.: Condens. Matter* **2005**, *17*, 4035.

(94) (a) Granqvist, C. G. *Sol. Energy Mater. Sol. Cells* **2007**, *91*, 1529. (b) Wu, C. Z.; Xie, Y. *Energy Environ. Sci.* **2010**, *3*, 1191.

(95) *Vanadia Catalysts for Selective Oxidation of Hydrocarbons and Their Derivatives*; Grzybowska-Swierkosz, B., Trifiro, F., Vedrine, J. C., Eds.; Elsevier: Amsterdam, 1997.

(96) (a) Busca, G.; Lietti, L.; Ramis, G.; Berti, F. *Appl. Catal., B* **1998**, *18*, 1. (b) Cai, Y. P.; Ozkan, U. S. *Appl. Catal.* **1991**, *78*, 241.

(97) (a) Wachs, I. E. *Catal. Today* **2005**, *100*, 79. (b) Burcham, L. J.; Deo, G.; Gao, X. T.; Wachs, I. E. *Top. Catal.* **2000**, *11*, 85. (c) Romanyshyn, Y.; Guimond, S.; Kuhlenbeck, H.; Kaya, S.; Blum, R.; Niehus, H.; Shaikhutdinov, S.; Simic-Milosevic, V.; Nilius, N.; Freund, H. J.; Ganduglia-Pirovano, M.; Fortrie, R.; Döbler, J.; Sauer, J. *Top. Catal.* **2008**, *50*, 106.

(98) (a) Romanyshyn, Y.; Guimond, S.; Göbke, D.; Sturm, J. M.; Kuhlenbeck, H.; Döbler, J.; Ganduglia-Pirovano, M. V.; Sauer, J.; Freund, H. J. *Top. Catal.* **2011**, *54*, 669. (b) Sturm, J. M.; Göbke, D.; Kuhlenbeck, H.; Döbler, J.; Reinhardt, U.; Ganduglia-Pirovano, M. V.; Sauer, J.; Freund, H. J. *Phys. Chem. Chem. Phys.* **2009**, *11*, 3290. (c) Dupuis, A. C.; Abu Haija, M.; Richter, B.; Kuhlenbeck, H.; Freund, H. J. *Surf. Sci.* **2003**, *539*, 99. (d) Abu Haija, M.; Guimond, S.; Romanyshyn, Y.; Uhl, A.; Kuhlenbeck, H.; Todorova, T. K.; Ganduglia-Pirovano, M. V.; Döbler, J.; Sauer, J.; Freund, H. J. *Surf. Sci.* **2006**, *600*, 1497. (e) Abu Haija, M.; Guimond, S.; Uhl, A.; Kuhlenbeck, H.; Freund, H. J. *Surf. Sci.* **2006**, *600*, 1040.

(99) Kresse, G.; Surnev, S.; Schoiswohl, J.; Netzer, F. P. *Surf. Sci.* **2004**, *555*, 118.

(100) Schoiswohl, J.; Sock, M.; Surnev, S.; Ramsey, M. G.; Netzer, F. P.; Kresse, G.; Andersen, J. N. *Surf. Sci.* **2004**, *555*, 101.

(101) (a) Leisenberger, F. P.; Surnev, S.; Vitali, L.; Ramsey, M. G.; Netzer, F. P. *J. Vac. Sci. Technol., A* **1999**, *17*, 1743. (b) Surnev, S.; Vitali, L.; Ramsey, M. G.; Netzer, F. P.; Kresse, G.; Hafner, J. *Phys. Rev. B* **2000**, *61*, 13945. (c) Surnev, S.; Kresse, G.; Ramsey, M. G.; Netzer, F. P. *Phys. Rev. Lett.* **2001**, *87*, 086102.

(102) (a) Niehus, H.; Blum, R. P.; Ahlbehrendt, D. *Phys. Status Solidi A* **2001**, *187*, 151. (b) Niehus, H.; Blum, R. P.; Ahlbehrendt, D. *Surf. Rev. Lett.* **2003**, *10*, 353. (c) Niehus, H.; Calderon, H. A.; Freitag, B.; Stavale, F.; Achete, C. A. *Surf. Sci.* **2008**, *602*, L59.

(103) Window, A. J.; Hentz, A.; Sheppard, D. C.; Parkinson, G. S.; Niehus, H.; Ahlbehrendt, D.; Noakes, T. C. Q.; Bailey, P.; Woodruff, D. P. *Phys. Rev. Lett.* **2011**, *107*, 016105.

(104) Seifert, J.; Meyer, E.; Winter, H.; Kuhlenbeck, H. *Surf. Sci.* **2012**, *606*, L41.

(105) Todorova, T. K.; Ganduglia-Pirovano, M. V.; Sauer, J. *J. Phys. Chem. B* **2005**, *109*, 23523.

(106) Guimond, S.; Abu Haija, M.; Kaya, S.; Lu, J.; Weissenrieder, J.; Shaikhutdinov, S.; Kuhlenbeck, H.; Freund, H. J.; Döbler, J.; Sauer, J. *Top. Catal.* **2006**, *38*, 117.

(107) Sheppard, N. In *Vibrational Spectroscopy of Adsorbates*; Willis, R. F., Ed.; Springer Series in Chemical Physics 15; Springer Verlag: Berlin, 1980; p 165.

(108) (a) Schoiswohl, J.; Tzvetkov, G.; Pfuner, F.; Ramsey, M. G.; Surnev, S.; Netzer, F. P. *Phys. Chem. Chem. Phys.* **2006**, *8*, 1614. (b) Kröger, E. A.; Sayago, D. I.; Allegretti, F.; Knight, M. J.; Polcik, M.; Unterberger, W.; Lerotholi, T. J.; Hogan, K. A.; Lamont, C. L. A.; Cavalleri, M.; Hermann, K.; Woodruff, D. P. *Surf. Sci.* **2008**, *602*, 1267.

(109) Henderson, M. A. *Surf. Sci. Rep.* **2002**, *46*, 5.

(110) Thiel, P. A.; Madey, T. E. *Surf. Sci. Rep.* **1987**, *7*, 211.

(111) Wolfram Research, http://www.wolfram.com.

(112) Mensch, M. W.; Byrd, C. M.; Cox, D. F. *Catal. Today* **2003**, *85*, 279.

(113) Mullins, D. R.; Robbins, M. D.; Zhou, J. *Surf. Sci.* **2006**, *600*, 1547.

(114) Farfan-Arribas, E.; Madix, R. J. *Surf. Sci.* **2003**, *544*, 241.

(115) (a) Hermann, K.; Witko, M.; Druzinic, R.; Chakrabarti, A.; Tepper, B.; Elsner, M.; Gorschlüter, A.; Kuhlenbeck, H.; Freund, H. J. *J. Electron Spectrosc. Relat. Phenom.* **1999**, *98*, 245. (b) Tepper, B.; Richter, B.; Dupuis, A. C.; Kuhlenbeck, H.; Hucho, C.; Schilbe, P.; bin Yarmo, M. A.; Freund, H. J. *Surf. Sci.* **2002**, *496*, 64.

(116) Ganduglia-Pirovano, M. V.; Sauer, J. *Phys. Rev. B* **2004**, *70*, 045422.

(117) Göbke, D.; Romanyshyn, Y.; Guimond, S.; Sturm, J. M.; Kuhlenbeck, H.; Döbler, J.; Reinhardt, U.; Ganduglia-Pirovano, M. V.; Sauer, J.; Freund, H. J. *Angew. Chem., Int. Ed.* **2009**, *48*, 3695.

(118) Wang, Q. G.; Madix, R. J. *Surf. Sci.* **2002**, *496*, 51.

(119) (a) Wang, Q. G.; Madix, R. J. *Surf. Sci.* **2001**, *474*, L213. (b) Wong, G. S.; Concepcion, M. R.; Vohs, J. M. *J. Phys. Chem. B* **2002**, *106*, 6451. (c) Abbott, H. L.; Uhl, A.; Baron, M.; Lei, Y.; Meyer, R. J.; Stacchiola, D. J.; Bondarchuk, O.; Shaikhutdinov, S.; Freund, H. J. *J. Catal.* **2010**, *272*, 82. (d) Feng, T.; Vohs, J. M. *J. Catal.* **2004**, *221*, 619.

(120) Blum, R. P.; Niehus, H.; Hucho, C.; Fortrie, R.; Ganduglia-Pirovano, M. V.; Sauer, J.; Shaikhutdinov, S.; Freund, H. J. *Phys. Rev. Lett.* **2007**, *99*, 226103.

(121) (a) Kim, K. S.; Barteau, M. A. *Surf. Sci.* **1989**, *223*, 13. (b) Idriss, H.; Kim, K. S.; Barteau, M. A. *Surf. Sci.* **1992**, *262*, 113. (c) Dillingham, T. R.; Cornelison, D. M. *Surf. Sci. Spectra* **1999**, *6*, 146. (d) Ammon, C.; Bayer, A.; Held, G.; Richter, B.; Schmidt, T.; Steinruck, H. P. *Surf. Sci.* **2002**, *507*, 845.

(122) Burcham, L. J.; Wachs, I. E. *Catal. Today* **1999**, *49*, 467.

(123) Sauer, J.; Döbler, J. *Dalton Trans.* **2004**, *19*, 3116.

(124) (a) Peden, C. H. F.; Goodman, D. W. *J. Phys. Chem.* **1986**, *90*, 1360. (b) Peden, C. H. F.; Goodman, D. W.; Weisel, M. D.; Hoffmann, F. M. *Surf. Sci.* **1991**, *253*, 44. (c) Stampfl, C.; Scheffler, M. *Phys. Rev. Lett.* **1997**, *78*, 1500.

(125) (a) Over, H.; Kim, Y. D.; Seitsonen, A. P.; Wendt, S.; Lundgren, E.; Schmid, M.; Varga, P.; Morgante, A.; Ertl, G. *Science* **2000**, *287*, 1474. (b) Over, H.; Muhler, M. *Prog. Surf. Sci.* **2003**, *72*, 3. (c) Over, H.; Seitsonen, A. P.; Lundgren, E.; Schmid, M.; Varga, P. *J. Am. Chem. Soc.* **2001**, *123*, 11807. (d) Kim, Y. D.; Over, H.; Krabbes, G.; Ertl, G. *Top. Catal.* **2001**, *14*, 95.

(126) (a) Narkhede, V.; Aßmann, J.; Muhler, M. *Z. Phys. Chem. (Muenchen, Ger.)* **2005**, *219*, 979. (b) Blume, R.; Hävecker, M.; Zafeiratos, S.; Teschner, D.; Kleimenov, E.; Knop-Gericke, A.; Schlögl, R.; Barinov, A.; Dudin, P.; Kiskinova, M. *J. Catal.* **2006**, *239*, 354. (c) Aßmann, J.; Crihan, D.; Knapp, M.; Lundgren, E.; Löffler, E.; Muhler, M.; Narkhede, V.; Over, H.; Schmid, M.; Seitsonen, A. P.; Varga, P. *Angew. Chem., Int. Ed.* **2005**, *44*, 917.

(127) (a) Madey, T. E.; Albert Engelhardt, H.; Menzel, D. *Surf. Sci.* **1975**, *48*, 304. (b) Kostov, K. L.; Gsell, M.; Jakob, P.; Moritz, T.; Widdra, W.; Menzel, D. *Surf. Sci.* **1997**, *394*, L138.

(128) (a) Bottcher, A.; Niehus, H. *J. Chem. Phys.* **1999**, *110*, 3186. (b) Stampfl, C.; Schwegmann, S.; Over, H.; Scheffler, M.; Ertl, G. *Phys. Rev. Lett.* **1996**, *77*, 3371.

(129) (a) Böttcher, A.; Niehus, H. *Phys. Rev. B* **1999**, *60*, 14396. (b) Böttcher, A.; Niehus, H.; Schwegmann, S.; Over, H.; Ertl, G. *J. Phys. Chem. B* **1997**, *101*, 11185.

(130) Reuter, K.; Stampfl, C.; Verónica Ganduglia-Pirovano, M.; Scheffler, M. *Chem. Phys. Lett.* **2002**, *352*, 311.

(131) Flege, J. I.; Hrbek, J.; Sutter, P. *Phys. Rev. B* **2008**, *78*, 165407.

(132) Martynova, Y.; Yang, B.; Yu, X.; Boscoboinik, J. A.; Shaikhutdinov, S.; Freund, H. J. *Catal. Lett.* **2012**, *142*, 657.

(133) Kim, Y. D.; Seitsonen, A. P.; Over, H. *Surf. Sci.* **2000**, *465*, 1.

(134) Over, H. *Chem. Rev.* **2012**, *112*, 3356.

(135) He, Y. B.; Knapp, M.; Lundgren, E.; Over, H. *J. Phys. Chem. B* **2005**, *109*, 21825.

(136) Rössler, M.; Günther, S.; Wintterlin, J. *J. Phys. Chem. C* **2007**, *111*, 2242.

(137) Kim, Y. D.; Schwegmann, S.; Seitsonen, A. P.; Over, H. *J. Phys. Chem. B* **2001**, *105*, 2205.

(138) Reuter, K.; Scheffler, M. *Phys. Rev. B* **2001**, *65*, 035406.

(139) Kim, Y. D.; Seitsonen, A. P.; Wendt, S.; Wang, J.; Fan, C.; Jacobi, K.; Over, H.; Ertl, G. *J. Phys. Chem. B* **2001**, *105*, 3752.

(140) (a) Reuter, K.; Scheffler, M. *Phys. Rev. B* **2003**, *68*, 045407. (b) Wang, J.; Fan, C. Y.; Jacobi, K.; Ertl, G. *J. Phys. Chem. B* **2002**, *106*, 3422. (c) Reuter, K.; Scheffler, M. *Phys. Rev. B* **2006**, *73*, 045433. (d) Farkas, A.; Mellau, G. C.; Over, H. *J. Phys. Chem. C* **2009**, *113*, 14341.

(141) (a) Over, H.; Muhler, M.; Seitsonen, A. P. *Surf. Sci.* **2007**, *601*, 5659. (b) Goodman, D. W.; Peden, C. H. F.; Chen, M. S. *Surf. Sci.* **2007**, *601*, L124.

(142) Matera, S.; Reuter, K. *Phys. Rev. B* **2010**, *82*, 085446.

(143) Over, H.; Balmes, O.; Lundgren, E. *Catal. Today* **2009**, *145*, 236.

(144) Gao, F.; Wang, Y.; Cai, Y.; Goodman, D. W. *Surf. Sci.* **2009**, *603*, 1126.

(145) (a) Wyckoff, R. W. G. *Crystal Structures*, 2nd ed.; Wiley-Interscience: New York, 1982. (b) Cornell, R. M.; Schwertmann, U. *The Iron Oxides*; VCH: Weinheim, 1996.

(146) Muan, A. *Am. J. Sci.* **1958**, *256*, 171.

(147) Leygraf, C.; Ekelund, S. *Surf. Sci.* **1973**, *40*, 609.

(148) Qin, F.; Magtoto, N. P.; Garza, M.; Kelber, J. A. *Thin Solid Films* **2003**, *444*, 179.

(149) Busch, M.; Gruyters, M.; Winter, H. *Surf. Sci.* **2006**, *600*, 2778.

(150) Ketteler, G.; Ranke, W. *J. Phys. Chem. B* **2003**, *107*, 4320.

(151) Waddill, G. D.; Ozturk, O. *Surf. Sci.* **2005**, *575*, 35.

(152) Lopes, E. L.; Abreu, G. J. P.; Paniago, R.; Soares, E. A.; de Carvalho, V. E.; Pfannes, H. D. *Surf. Sci.* **2007**, *601*, 1239.

(153) (a) Deng, X.; Lee, J.; Matranga, C. *Surf. Sci.* **2010**, *604*, 627. (b) Deng, X.; Matranga, C. *J. Phys. Chem. C* **2009**, *113*, 11104. (c) Khan, N. A.; Matranga, C. *Surf. Sci.* **2008**, *602*, 932.

(154) Pflitsch, C.; David, R.; Verheij, L. K.; Franchy, R. *Surf. Sci.* **2001**, *488*, 32.

(155) Weiss, W.; Ranke, W. *Prog. Surf. Sci.* **2002**, *70*, 1.

(156) Vurens, G. H.; Salmeron, M.; Somorjai, G. A. *Surf. Sci.* **1988**, *201*, 129.

(157) (a) Galloway, H. C.; Benítez, J. J.; Salmeron, M. *Surf. Sci.* **1993**, *298*, 127. (b) Galloway, H. C.; Sautet, P.; Salmeron, M. *Phys. Rev. B: Condens. Matter Mater. Phys.* **1996**, *54*, R11145.

(158) (a) Kim, Y. J.; Westphal, C.; Ynzunza, R. X.; Galloway, H. C.; Salmeron, M.; Van Hove, M. A.; Fadley, C. S. *Phys. Rev. B* **1997**, *55*, R13448. (b) Kim, Y. J.; Westphal, C.; Ynzunza, R. X.; Wang, Z.; Galloway, H. C.; Salmeron, M.; Van Hove, M. A.; Fadley, C. S. *Surf. Sci.* **1998**, *416*, 68.

(159) Shaikhutdinov, S. K.; Meyer, R.; Lahav, D.; Bäumer, M.; Klüner, T.; Freund, H. J. *Phys. Rev. Lett.* **2003**, *91*, 761021.

(160) Ritter, M.; Ranke, W.; Weiss, W. *Phys. Rev. B* **1998**, *57*, 7240.

(161) (a) Shaikhutdinov, S.; Ritter, M.; Weiss, W. *Phys. Rev. B: Condens. Matter Mater. Phys.* **2000**, *62*, 7535. (b) Vurens, G. H.; Maurice, V.; Salmeron, M.; Somorjai, G. A. *Surf. Sci.* **1992**, *268*, 170.

(162) Weiss, W.; Ritter, M. *Phys. Rev. B* **1999**, *59*, 5201.

(163) Weiss, W.; Barbieri, A.; Vanhove, M. A.; Somorjai, G. A. *Phys. Rev. Lett.* **1993**, *71*, 1848.

(164) Ritter, M.; Weiss, W. *Surf. Sci.* **1999**, *432*, 81.

(165) Shaikhutdinov, S. K.; Ritter, M.; Wang, X. G.; Over, H.; Weiss, W. *Phys. Rev. B: Condens. Matter Mater. Phys* **1999**, *60*, 11062.

(166) Lennie, A. R.; Condon, N. G.; Leibsle, F. M.; Murray, P. W.; Thornton, G.; Vaughan, D. J. *Phys. Rev. B* **1996**, *53*, 10244.

(167) Condon, N. G.; Leibsle, F. M.; Parker, T.; Lennie, A. R.; Vaughan, D. J.; Thornton, G. *Phys. Rev. B: Condens. Matter Mater. Phys.* **1997**, *55*, 15885.

(168) Condon, N. G.; Leibsle, F. M.; Lennie, A. R.; Murray, P. W.; Vaughan, D. J.; Thornton, G. *Phys. Rev. Lett.* **1995**, *75*, 1961.

(169) (a) Berdunov, N.; Murphy, S.; Mariotto, G.; Shvets, I. V. *Phys. Rev. B* **2004**, *70*, 085404. (b) Shvets, I. V.; Berdunov, N.; Mariotto, G.; Murphy, S. *Europhys. Lett.* **2003**, *63*, 867.

(170) Paul, M.; Sing, M.; Claessen, R.; Schrupp, D.; Brabers, V. A. M. *Phys. Rev. B* **2007**, *76*, 075412.

(171) Shaikhutdinov, S.; Weiss, W. *J. Mol. Catal. A: Chem.* **2000**, *158*, 129.

(172) Shimizu, T. K.; Jung, J.; Kato, H. S.; Kim, Y.; Kawai, M. *Phys. Rev. B* **2010**, *81*, 235429.

(173) Lemire, C.; Meyer, R.; Henrich, V. E.; Shaikhutdinov, S.; Freund, H. J. *Surf. Sci.* **2004**, *572*, 103.

(174) Henrich, V. E.; Shaikhutdinov, S. K. *Surf. Sci.* **2005**, *574*, 306.

(175) Sala, A.; Qin, Z. H.; Shaikhutdinov, S.; Schmidt, T.; Freund, H.-J. *Phys. Rev. B* **2012**, *86*, 155430.

(176) (a) Joseph, Y.; Kuhrs, C.; Ranke, W.; Ritter, M.; Weiss, W. *Chem. Phys. Lett.* **1999**, *314*, 195. (b) Joseph, Y.; Ranke, W.; Weiss, W. *J. Phys. Chem. B* **2000**, *104*, 3224. (c) Ketteler, G.; Weiss, W.; Ranke, W.; Schlögl, R. *Phys. Chem. Chem. Phys.* **2001**, *3*, 1114.

(177) Ringleb, F.; Fujimori, Y.; Wang, H. F.; Ariga, H.; Carrasco, E.; Sterrer, M.; Freund, H. J.; Giordano, L.; Pacchioni, G.; Goniakowski, J. *J. Phys. Chem. C* **2011**, *115*, 19328.

(178) Leist, U.; Ranke, W.; Al-Shamery, K. *Phys. Chem. Chem. Phys.* **2003**, *5*, 2435.

(179) Kendelewicz, T.; Liu, P.; Doyle, C. S.; Brown, G. E., Jr.; Nelson, E. J.; Chambers, S. A. *Surf. Sci.* **2000**, *453*, 32.

(180) Cutting, R. S.; Muryn, C. A.; Vaughan, D. J.; Thornton, G. *Surf. Sci.* **2008**, *602*, 1155.

(181) Cutting, R. S.; Muryn, C. A.; Thornton, G.; Vaughan, D. J. *Geochim. Cosmochim. Acta* **2006**, *70*, 3593.

(182) Lemire, C.; Bertarione, S.; Zecchina, A.; Scarano, D.; Chaka, A.; Shaikhutdinov, S.; Freund, H. J. *Phys. Rev. Lett.* **2005**, *94*, 166101.

(183) Barraclough, C. G.; Lewis, J.; Nyholm, R. S. *J. Chem. Soc.* **1959**, 3552.

(184) Ahdjoudj, J.; Martinsky, C.; Minot, C.; Van Hove, M. A.; Somorjai, G. A. *Surf. Sci.* **1999**, *443*, 133.

(185) Zhu, L.; Yao, K. L.; Liu, Z. L. *Phys. Rev. B* **2006**, *74*, 035409.

(186) Huang, D.-M.; Cao, D.-B.; Li, Y.-W.; Jiao, H. *J. Phys. Chem. B* **2006**, *110*, 13920.

(187) Grillo, M. E.; Finnis, M. W.; Ranke, W. *Phys. Rev. B* **2008**, *77*, 075407.

(188) Yu, X.; Huo, C.-F.; Li, Y.-W.; Wang, J.; Jiao, H. *Surf. Sci.* **2012**, *606*, 872.

(189) (a) Chambers, S. A. *Surf. Sci. Rep.* **2000**, *39*, 105. (b) Chambers, S. A.; Joyce, S. A. *Surf. Sci.* **1999**, *420*, 111. (c) Chambers, S. A.; Thevuthasan, S.; Joyce, S. A. *Surf. Sci.* **2000**, *450*, L273. (d) Gaines, J. M.; Bloemen, P. J. H.; Kohlhepp, J. T.; Bulle-Lieuwma, C. W. T.; Wolf, R. M.; Reinders, A.; Jungblut, R. M.; van der Heijden, P. A. A.; van Eemeren, J. T. W. M.; de Stegge, J. a.; de Jonge, W. J. M. *Surf. Sci.* **1997**, *373*, 85. (e) Gao, Y.; Chambers, S. A. *J. Cryst. Growth* **1997**, *174*, 446. (f) Gao, Y.; Kim, Y. J.; Chambers, S. A.; Bai, G. *J. Vac. Sci. Technol., A* **1997**, *15*, 332. (g) Kim, Y. J.; Gao, Y.; Chambers, S. A. *Surf. Sci.* **1997**, *371*, 358. (h) Kim-Ngan, N. T. H.; Balogh, A. G.; Meyer, J. D.; Brötz, J.; Hummelt, S.; Zając, M.; Ślęzak, T.; Korecki, J. *Surf. Sci.* **2008**, *602*, 2358. (i) Wang, H.-Q.; Altman, E. I.; Henrich, V. E. *Phys. Rev. B* **2008**, *77*, 085313.

(190) (a) Tarrach, G.; Bürgler, D.; Schaub, T.; Wiesendanger, R.; Güntherodt, H. J. *Surf. Sci.* **1993**, *285*, 1. (b) Ceballos, S. F.; Mariotto, G.; Jordan, K.; Murphy, S.; Seoighe, C.; Shvets, I. V. *Surf. Sci.* **2004**, *548*, 106.

(191) Pentcheva, R.; Wendler, F.; Meyerheim, H. L.; Moritz, W.; Jedrecy, N.; Scheffler, M. *Phys. Rev. Lett.* **2005**, *94*, 126101.

(192) Pentcheva, R.; Moritz, W.; Rundgren, J.; Frank, S.; Schrupp, D.; Scheffler, M. *Surf. Sci.* **2008**, *602*, 1299.

(193) Mijiritskii, A. V.; Boerma, D. O. *Surf. Sci.* **2001**, *486*, 73.

(194) Stanka, B.; Hebenstreit, W.; Diebold, U.; Chambers, S. A. *Surf. Sci.* **2000**, *448*, 49.

(195) Ruby, C.; Humbert, B.; Fusy, J. *Surf. Interface Anal.* **2000**, *29*, 377.

(196) Spiridis, N.; Handke, B.; Slezak, T.; Barbasz, J.; Zajac, M.; Haber, J.; Korecki, J. *J. Phys. Chem. B* **2004**, *108*, 14356.

(197) Spiridis, N.; Barbasz, J.; Łodziana, Z.; Korecki, J. *Phys. Rev. B* **2006**, *74*, 155423.

(198) Rustad, J. R.; Wasserman, E.; Felmy, A. R. *Surf. Sci.* **1999**, *432*, L583.

(199) Parkinson, G. S.; Novotný, Z.; Jacobson, P.; Schmid, M.; Diebold, U. *Surf. Sci.* **2011**, *605*, L42.

(200) Maris, G.; Shklyarevskii, O.; Jdira, L.; Hermsen, J. G. H.; Speller, S. *Surf. Sci.* **2006**, *600*, 5084.

(201) Jansen, R.; Brabers, V. A. M.; van Kempen, H. *Surf. Sci.* **1995**, *328*, 237.

(202) (a) Kurtz, R. L.; Henrich, V. E. *Surf. Sci.* **1983**, *129*, 345. (b) Lad, R. J.; Henrich, V. E. *Surf. Sci.* **1988**, *193*, 81.

(203) Condon, N. G.; Murray, P. W.; Leibsle, F. M.; Thornton, G.; Lennie, A. R.; Vaughan, D. J. *Surf. Sci.* **1994**, *310*, L609.

(204) Condon, N. G.; Leibsle, F. M.; Lennie, A. R.; Murray, P. W.; Parker, T. M.; Vaughan, D. J.; Thornton, G. *Surf. Sci.* **1998**, *397*, 278.

(205) Lanier, C. H.; Chiaramonti, A. N.; Marks, L. D.; Poeppelmeier, K. R. *Surf. Sci.* **2009**, *603*, 2574.

(206) Eggleston, C. M.; Hochella, M. F., Jr. *Am. Mineral.* **1992**, *77*, 911.

(207) (a) Fujii, T.; Alders, D.; Voogt, F. C.; Hibma, T.; Thole, B. T.; Sawatzky, G. A. *Surf. Sci.* **1996**, *366*, 579. (b) Fujii, T.; De Groot, F. M. F.; Sawatzky, G. A.; Voogt, F. C.; Hibma, T.; Okada, K. *Phys. Rev. B: Condens. Matter Mater. Phys.* **1999**, *59*, 3195.

(208) Yi, S. I.; Liang, Y.; Thevuthasan, S.; Chambers, S. A. *Surf. Sci.* **1999**, *443*, 212.

(209) Lewandowski, M. Ph.D. Thesis, Technical University Berlin, 2011.

(210) (a) Shaikhutdinov, S. K.; Weiss, W. *Surf. Sci.* **1999**, *432*, L627. (b) Ketteler, G.; Weiss, W.; Ranke, W. *Surf. Rev. Lett.* **2001**, *8*, 661.

(211) Wang, X. G.; Weiss, W.; Shaikhutdinov, S. K.; Ritter, M.; Petersen, M.; Wagner, F.; Schlögl, R.; Scheffler, M. *Phys. Rev. Lett.* **1998**, *81*, 1038.

(212) Wang, R.-p.; Zhou, Y.-l.; Pan, S.-h.; Zhang, H.; Guo, X.-x.; Xiong, X.-m.; Lu, H.-b.; Zhen, Z.-h.; Yang, G.-z. *J. Appl. Phys.* **1998**, *84*, 1994.

(213) Chambers, S. A.; Yi, S. I. *Surf. Sci.* **1999**, *439*, L785.

(214) Lewis-Ballester, A.; Batabyal, D.; Egawa, T.; Lu, C.; Lin, Y.; Marti, M. A.; Capece, L.; Estrin, D. A.; Yeh, S.-R. *Proc. Natl. Acad. Sci. U.S.A.* **2009**, *106*, 17371.

(215) Bergermayer, W.; Schweiger, H.; Wimmer, E. *Phys. Rev. B* **2004**, *69*, 195409.

(216) Zecchina, A.; Scarano, D.; Reller, A. *J. Chem. Soc., Faraday Trans. 1* **1988**, *84*, 2327.

(217) Jarvis, E. A.; Chaka, A. M. *Surf. Sci.* **2007**, *601*, 1909.

(218) (a) Barbier, A.; Stierle, A.; Finocchi, F.; Jupille, J. *J. Phys.: Condens. Matter* **2008**, *20*, 184014. (b) Barbier, A.; Stierle, A.; Kasper, N.; Guittet, M. J.; Jupille, J. *Phys. Rev. B* **2007**, *75*, 233406.

(219) (a) Weiss, W.; Schlögl, R. *Top. Catal.* **2000**, *13*, 75. (b) Kuhrs, C.; Arita, Y.; Weiss, W.; Ranke, W.; Schlögl, R. *Top. Catal.* **2000**, *14*, 111.

(220) Zscherpel, D.; Ranke, W.; Weiss, W.; Schlogl, R. *J. Chem. Phys.* **1998**, *108*, 9506.

(221) Weiss, W.; Zscherpel, D.; Schlögl, R. *Catal. Lett.* **1998**, *52*, 215.

(222) (a) Shaikhutdinov, S. K.; Weiss, W.; Schlögl, R. *Appl. Surf. Sci.* **2000**, *161*, 497. (b) Shaikhutdinov, S.; Joseph, Y.; Kuhrs, C.; Ranke, W.; Weiss, W. *Faraday Discuss.* **1999**, *114*, 363.

(223) Coulter, K.; Goodman, D. W.; Moore, R. G. *Catal. Lett.* **1995**, *31*, 1.

(224) Mestl, G.; Maksimova, N. I.; Keller, N.; Roddatis, V. V.; Schlögl, R. *Angew. Chem., Int. Ed.* **2001**, *40*, 2066.

(225) Huang, W. X.; Ranke, W.; Schlogl, R. *J. Phys. Chem. B* **2005**, *109*, 9202.

(226) (a) Praline, G.; Koel, B. E.; Hance, R. L.; Lee, H. I.; White, J. M. *J. Electron Spectrosc. Relat. Phenom.* **1980**, *21*, 17. (b) Helms, C. R.; Spicer, W. E. *Appl. Phys. Lett.* **1972**, *21*, 237.

(227) (a) Inoue, T.; Yamamoto, Y.; Koyama, S.; Suzuki, S.; Ueda, Y. *Appl. Phys. Lett.* **1990**, *56*, 1332. (b) Ami, T.; Ishida, Y.; Nagasawa, N.; Machida, A.; Suzuki, M. *Appl. Phys. Lett.* **2001**, *78*, 1361. (c) Furusawa, M.; Tashiro, J.; Sasaki, A.; Nakajima, K.; Takakura, M.; Chikyow, T.; Ahmet, P.; Yoshimoto, M. *Appl. Phys. Lett.* **2001**, *78*, 1838.

(228) Norton, D. P.; Budai, J. D.; Chisholm, M. F. *Appl. Phys. Lett.* **2000**, *76*, 1677.

(229) Tian, C.; Du, Y.; Chan, S. W. *J. Vac. Sci. Technol., A* **1997**, *15*, 85.

(230) Alexandrou, M.; Nix, R. M. *Surf. Sci.* **1994**, *321*, 47.

(231) (a) Costa-Nunes, O.; Ferrizz, R. M.; Gorte, R. J.; Vohs, J. M. *Surf. Sci.* **2005**, *592*, 8. (b) Zaitsev, A. G.; Ockenfuss, G.; Guggi, D.; Wordenweber, R.; Kruger, U. *J. Appl. Phys.* **1997**, *81*, 3069.

(232) (a) Mullins, D. R.; Radulovic, P. V.; Overbury, S. H. *Surf. Sci.* **1999**, *429*, 186. (b) Lu, J. L.; Gao, H. J.; Shaikhutdinov, S.; Freund, H. J. *Surf. Sci.* **2006**, *600*, 5004. (c) Baron, M.; Bondarchuk, O.; Stacchiola, D.; Shaikhutdinov, S.; Freund, H. J. *J. Phys. Chem. C* **2009**, *113*, 6042.

(233) (a) Hardacre, C.; Roe, G. M.; Lambert, R. M. *Surf. Sci.* **1995**, *326*, 1. (b) Schierbaum, K.-D. *Surf. Sci.* **1998**, *399*, 29.

(234) Mullins, D. R.; Overbury, S. H.; Huntley, D. R. *Surf. Sci.* **1998**, *409*, 307.

(235) Dmowski, W.; Egami, T.; Gorte, R.; Vohs, J. *Physica B (Amsterdam, Neth.)* **1996**, *221*, 420.

(236) (a) Henderson, M. A.; Perkins, C. L.; Engelhard, M. H.; Thevuthasan, S.; Peden, C. H. F. *Surf. Sci.* **2003**, *526*, 1. (b) Dmowski, W.; Mamontov, E.; Egami, T.; Putna, S.; Gorte, R. *Physica B (Amsterdam, Neth.)* **1998**, *248*, 95.

(237) (a) Eck, S.; Castellarin-Cudia, C.; Surnev, S.; Ramsey, M. G.; Netzer, F. P. *Surf. Sci.* **2002**, *520*, 173. (b) Castellarin-Cudia, C.; Surnev, S.; Schneider, G.; Podlucky, R.; Ramsey, M. G.; Netzer, F. P. *Surf. Sci.* **2004**, *554*, L120.

(238) (a) Siokou, A.; Nix, R. M. *J. Phys. Chem. B* **1999**, *103*, 6984. (b) Dvořák, F.; Stetsovych, O.; Steger, M.; Cherradi, E.; Matolínová, I.; Tsud, N.; Škoda, M.; Skála, T.; Mysliveček, J.; Matolín, V. *J. Phys. Chem. C* **2011**, *115*, 7496. (c) Šutara, F.; Cabala, M.; Sedláček, L.; Skála, T.; Škoda, M.; Matolín, V.; Prince, K. C.; Cháb, V. *Thin Solid Films* **2008**, *516*, 6120.

(239) Xiao, W.; Guo, Q.; Wang, E. G. *Chem. Phys. Lett.* **2003**, *368*, 527.

(240) Baddeley, C. J.; Stephenson, A. W.; Hardacre, C.; Tikhov, M.; Lambert, R. M. *Phys. Rev. B* **1997**, *56*, 12589.

(241) (a) Berner, U.; Schierbaum, K.-D. *Phys. Rev. B* **2002**, *65*, 235404. (b) Berner, U.; Schierbaum, K. *Thin Solid Films* **2001**, *400*, 46. (c) Matolín, V.; Libra, J.; Matolínová, I.; Nehasil, V.; Sedláček, L.; Šutara, F. *Appl. Surf. Sci.* **2007**, *254*, 153.

(242) (a) Nörenberg, H.; Briggs, G. A. D. *Surf. Sci.* **1999**, *424*, L352. (b) Nörenberg, H.; Briggs, G. A. D. *Phys. Rev. Lett.* **1997**, *79*, 4222.

(243) (a) Zhou, J.; Mullins, D. R. *Surf. Sci.* **2006**, *600*, 1540. (b) Mullins, D. R.; McDonald, T. S. *Surf. Sci.* **2007**, *601*, 4931. (c) Mullins, D. R.; McDonald, T. S. *Surf. Sci.* **2008**, *602*, 1280.

(244) Lu, J. L.; Gao, H. J.; Shaikhutdinov, S.; Freund, H. J. *Catal. Lett.* **2007**, *114*, 8.

(245) Jerratsch, J.-F.; Shao, X.; Nilius, N.; Freund, H.-J.; Popa, C.; Ganduglia-Pirovano, M. V.; Burow, A. M.; Sauer, J. *Phys. Rev. Lett.* **2011**, *106*, 246801.

(246) Grinter, D. C.; Ithnin, R.; Pang, C. L.; Thornton, G. *J. Phys. Chem. C* **2010**, *114*, 17036.

(247) Namai, Y.; Fukui, K.-I.; Iwasawa, Y. *Catal. Today* **2003**, *85*, 79.

(248) Esch, F.; Fabris, S.; Zhou, L.; Montini, T.; Africh, C.; Fornasiero, P.; Comelli, G.; Rosei, R. *Science* **2005**, *309*, 752.

(249) (a) Kresse, G.; Blaha, P.; Da Silva, J. L. F.; Ganduglia-Pirovano, M. V. *Phys. Rev. B* **2005**, *72*, 237101. (b) Fabris, S.; de Gironcoli, S.; Baroni, S.; Vicario, G.; Balducci, G. *Phys. Rev. B* **2005**, *71*, 041102. (c) Fabris, S.; de Gironcoli, S.; Baroni, S.; Vicario, G.; Balducci, G. *Phys. Rev. B* **2005**, *72*, 237102. (d) Skorodumova, N. V.; Baudin, M.;

Hermansson, K. *Phys. Rev. B* **2004**, *69*, 075401. (e) Nolan, M.; Parker, S. C.; Watson, G. W. *Surf. Sci.* **2005**, *595*, 223.

(250) Ganduglia-Pirovano, M. V.; Da Silva, J. L. F.; Sauer, J. *Phys. Rev. Lett.* **2009**, *102*, 026101.

(251) Torbrügge, S.; Reichling, M.; Ishiyama, A.; Morita, S.; Custance, Ó. *Phys. Rev. Lett.* **2007**, *99*, 056101.

(252) Torbrugge, S.; Cranney, M.; Reichling, M. *Appl. Phys. Lett.* **2008**, *93*, 073112.

(253) Nilius, N.; Kozlov, S. M.; Jerratsch, J.-F.; Baron, M.; Shao, X.; Viñes, F.; Shaikhutdinov, S.; Neyman, K. M.; Freund, H.-J. *ACS Nano* **2011**, *6*, 1126.

(254) Hardacre, C.; Ormerod, R. M.; Lambert, R. M. *J. Phys. Chem.* **1994**, *98*, 10901.

(255) Frost, J. C. *Nature* **1988**, *334*, 577.

(256) (a) Lei, Y.; Lewandowski, M.; Sun, Y.-N.; Fujimori, Y.; Martynova, Y.; Groot, I. M. N.; Meyer, R. J.; Giordano, L.; Pacchioni, G.; Goniakowski, J.; Noguera, C.; Shaikhutdinov, S.; Freund, H.-J. *ChemCatChem* **2011**, *3*, 671. (b) Sun, Y. N.; Qin, Z. H.; Lewandowski, M.; Carrasco, E.; Sterrer, M.; Shaikhutdinov, S.; Freund, H. J. *J. Catal.* **2009**, *266*, 359. (c) Sun, Y.-N.; Giordano, L.; Goniakowski, J.; Lewandowski, M.; Qin, Z.-H.; Noguera, C.; Shaikhutdinov, S.; Pacchioni, G.; Freund, H.-J. *Angew. Chem., Int. Ed.* **2010**, *49*, 4418. (d) Sun, Y.-N.; Qin, Z.-H.; Lewandowski, M.; Kaya, S.; Shaikhutdinov, S.; Freund, H.-J. *Catal. Lett.* **2008**, *126*, 31.

(257) Ferrizz, R. M.; Wong, G. S.; Egami, T.; Vohs, J. M. *Langmuir* **2001**, *17*, 2464.

(258) Deo, G.; Wachs, I. E.; Haber, J. *Crit. Rev. Surf. Chem.* **1994**, *4*, 141.

(259) (a) Khodakov, A.; Olthof, B.; Bell, A. T.; Iglesia, E. *J. Catal.* **1999**, *181*, 205. (b) Olthof, B.; Khodakov, A.; Bell, A. T.; Iglesia, E. *J. Phys. Chem. B* **2000**, *104*, 1516.

(260) (a) Magg, N.; Immaraporn, B.; Giorgi, J. B.; Schroeder, T.; Bäumer, M.; Döbler, J.; Wu, Z. L.; Kondratenko, E.; Cherian, M.; Baerns, M.; Stair, P. C.; Sauer, J.; Freund, H. J. *J. Catal.* **2004**, *226*, 88. (b) Kaya, S.; Sun, Y. N.; Weissenrieder, J.; Stacchiola, D.; Shaikhutdinov, S.; Freund, H. J. *J. Phys. Chem. C* **2007**, *111*, 5337.

(261) Baron, M.; Abbott, H.; Bondarchuk, O.; Stacchiola, D.; Uhl, A.; Shaikhutdinov, S.; Freund, H.-J.; Popa, C.; Ganduglia-Pirovano, M. V.; Sauer, J. *Angew. Chem., Int. Ed.* **2009**, *48*, 8006.

(262) Banares, M. A.; Mestl, G. *Adv. Catal.* **2009**, *52*, 43.

(263) (a) Vohs, J. M.; Feng, T.; Wong, G. S. *Catal. Today* **2003**, *85*, 303. (b) Wong, G. S.; Kragten, D. D.; Vohs, J. M. *J. Phys. Chem. B* **2001**, *105*, 1366.

(264) Zhou, Y.; Zhou, J. *Surf. Sci.* **2012**, *606*, 749.

(265) Skala, T.; Tsud, N.; Prince, K. C.; Matolin, V. *J. Phys.: Condens. Matter* **2011**, *23*, 215001.